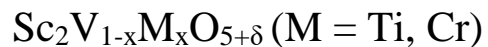


# Controlling Defect Fluorites via Oxidative Charge Ordering in



By

Brooke Nicole Richtik

A thesis submitted to the  
Faculty of Graduate Studies of the University of Manitoba  
in partial fulfilment of the requirements of the degree of

Master of Science

Department of Chemistry  
University of Manitoba  
Winnipeg, Manitoba, Canada

Copyright © 2021 by Brooke N. Richtik

## Abstract

The scandium vanadate system contains a diverse family of structures including the bixbyite (s.g.  $Ia\bar{3}$ ), defect fluorite (s.g.  $Fm\bar{3}m$ ), zircon (s.g.  $I41/amd$ ), and tetragonal- $\text{Sc}_2\text{VO}_5$  (s.g.  $I\bar{4}$ ) structures. Here the structures of the scandium vanadates are determined by charge and size of cations, and oxygen stoichiometry. Consequently, redox chemistry can be used to control the oxidation state of vanadium and navigate between these structures. This thesis focuses on vanadium's neighbouring elements, titanium and chromium, and investigates if similar chemistry can be conducted as for the scandium vanadates. A series of  $\text{Sc}_2\text{V}_{1-x}\text{M}_x\text{O}_{5+\delta}$  ( $M = \text{Ti}$  and  $\text{Cr}$ ) phases were prepared and a detailed structural analysis was conducted including x-ray and neutron diffraction, XANES and DC magnetic susceptibility measurements.

Of particular interest is the tetragonal- $\text{Sc}_2\text{VO}_5$  structure. The vanadium sublattice within the tetragonal structure consists of two distinct crystallographic sites with octahedral and tetrahedral coordination. We show that the octahedral and tetrahedral sites can be individually controlled as demonstrated with the synthesis of tetragonal- $\text{Sc}_2\text{Ti}_{0.8}\text{V}_{0.2}\text{O}_{5+\delta}$  where  $\text{Ti}^{4+}$  and  $\text{V}^{5+}$  occupy octahedral and tetrahedral sites, respectively. Notably the vanadium sublattice consists of tetrahedral motifs that are geometrically frustrated. Substitution of paramagnetic chromium into the tetrahedral site provides a route to tune magnetic interactions within the tetragonal  $I\bar{4}$  structure.

## Acknowledgements

This past two-years has come with many expected and unexpected challenges. This time has taught me to truly value moments we spend with others, and it has taught me the importance of community. I am utterly grateful for the friends and family a part of my community. Even though we have spent the past year and a half a part, their support has enabled me to reach where I am today.

First and foremost, I am entirely thankful to my supervisors Drs. Mario Bieringer and Chris Wiebe for their support. Thank you for pushing me out of my comfort zone, allowing me to ask questions, make mistakes, and always being there to offer support and advice when needed. Chris and Mario's passion for science spreads to those around them. Their work ethic, integrity, and respect and kindness to others are a few reasons why they are role models in my life. The past two years has been filled with learning, both inside and outside the lab. I am sincerely thankful to them for sharing their passion for science with me.

I am very lucky to be apart of two wonderful lab groups filled with talented scientists and good friends. I would like to thank members of the Wiebe and Bieringer research groups: Megan Rutherford, Dr. Cole Mauws, Dr. Joey Lussier, Sebastian Wright and Dmitry Vrublevskiy.

I am grateful to have been apart of Bison athletics during my degree. To my coach, Claude Berube, thank you for providing consistency in a time of a lot of uncertainty and continually encouraging us to put one foot in front of the other. To my teammates, thank you for pushing me to be my best and providing many laughs along the way.

Finally, to my family, thank you for providing me with endless love and support. I could not do this without you.

## Contents

Abstract .....	ii
Acknowledgements .....	iii
Contents .....	iv
List of Figures .....	vi
List of Tables .....	x
Chapter 1: Introduction .....	1
1.1 Structure: .....	1
1.2 Scandium Vanadate Family of Structures: .....	4
1.3 Objective & Motivation: .....	5
Chapter 2: Experimental .....	8
2.1 Techniques: .....	8
2.1.1 Diffraction .....	8
2.1.2 Powder X-ray Diffraction. ....	10
2.1.3 Neutron Diffraction .....	11
2.1.4 Rietveld Refinement. ....	13
2.1.5 Direct Current Magnetic Susceptibility. ....	16
2.1.6 X-ray Absorption Spectroscopy .....	17
2.2 Methods .....	19
2.2.1 Synthesis .....	19
2.2.2 Powder X-ray Diffraction .....	24
2.2.3 XANES .....	24
2.2.4 Magnetic Measurements .....	25
2.2.5 Neutron Diffraction .....	25
Chapter 3: Titanium and the Scandium Vanadates .....	26
3.1 Disordered Structures: .....	26
3.1.1 Background. ....	26
3.1.2 Results and Discussion. ....	28
3.2 Ordered Structure: .....	35
3.2.1 Background. ....	35
3.2.2 Results and Discussion. ....	36
3.3 Conclusion: .....	45

Chapter 4: Chromium and the Scandium Vanadates .....	47
4.1 Ternary Phase Diagram: $\text{Sc}^{3+} - \text{Cr}^{3+} - \text{V}^{3+}$ .....	47
4.1.1 Background .....	47
4.1.2 Results and Discussion. ....	48
4.2 $\text{Sc}_2\text{V}_{0.8}\text{Cr}_{0.2}\text{O}_{5+\delta}$ phases. ....	53
4.2.1 Background .....	53
4.2.2 Results and Discussion. ....	55
4.3 Conclusion.....	64
Chapter 5: Conclusion.....	65
References.....	69
Appendix.....	72

## List of Figures

- Figure 1.1 Illustration of the cubic fluorite structure (s.g.  $Fm\bar{3}m$ ). Blue =  $4a$  site and pink =  $8c$  site. (Left) Illustration of the cubic fluorite with emphasis on the  $AO_8$  cubic coordination and its edge sharing interconnectivity (Right) Emphasis on the anionic tetrahedral environment, and illustration of vacancy that can cause oxygen anion-hopping. 1
- Figure 1.2 Illustration of the tetragonal  $Sc_2VO_5$  structure (s.g.  $I\bar{4}$ ). (Left) Total structure, (middle) B-sublattice; and (right) B-sublattice extending beyond the unit cell to highlight the  $V1^{8g}$  clusters connected by the tetrahedral  $V2^{2c}$  site. White =  $Sc1^{4f}$  site, dark grey =  $Sc2^{8g}$  site, light grey =  $Sc3^{8g}$  site, teal =  $V1^{8g}$  site, and dark blue =  $V2^{2c}$  site. ....2
- Figure 1.3 Illustration of bixbyite structure (s.g.  $Ia\bar{3}$ ); and (right) topotactically oxidized product where additional oxygen anions are present in the  $16c$  site. Dark blue =  $24d$  site, light blue =  $8a$  site, pink =  $48e$  site, and purple =  $16c$  .....3
- Figure 1.4 Illustration of zircon structure (s.g.  $I4_1/amd$ ). Grey =  $4b$  site, blue =  $4a$  site, and pink =  $16h$  site. ....3
- Figure 1.5 Illustration of rutile structure (s.g.  $P4_2/mnm$ ). Purple = cation  $2a$  site and pink = anion  $4f$  site. ....3
- Figure 1.6 Illustration of corundum structure (s.g.  $R\bar{3}c$ ). Green =  $12c$  site and pink =  $18e$  site. ....4
- Figure 1.7 Illustration of the impact of oxidation state of vanadium on structure formation in the scandium vanadate family of phases. ....4
- Figure 1.8  $V_4$  clusters (yellow) connected by  $V'O_4$  tetrahedra,  $V'$ =grey,  $O$ =red. Left insert: V-O bonds and frustrated nature of  $V_4$  clusters. Magnetic spins shown by grey arrows depict a potential ground state. This is one possible spin structure due to the tetrahedral motif. ....6
- Figure 2.1 Diffraction of x-rays from a lattice and illustration of the geometric derivation of Bragg's Law. ....8
- Figure 2.2 Simulated x-ray diffractogram of fluorite structure (s.g.  $Fm\bar{3}m$ , #225) highlighting destructive and constructive interferences. Calculated pattern = black line; and black ticks = Bragg peak positions. Simulated structures depicting lattice planes corresponding to the major Bragg peaks are included. ....9
- Figure 2.3 The dependence of atomic number on the x-ray scattering factor as a function of scattering angle.<sup>13</sup>.....10
- Figure 2.4 Comparison of scattering lengths from neutron and x-ray diffraction where the diameter of the circle is proportional to the atomic scattering length. X-ray form factors are reported at  $2\theta = 0^\circ$ , and neutron scattering length  $b$  is obtained from Sears.<sup>11</sup> Note:  $1 \text{ fm} = 1 \times 10^{-15} \text{ m}$ . ....12
- Figure 2.5 Schematic of POWGEN beamline annotated with major components. ....13
- Figure 2.6 Illustration of Gauss (red) and Lorentz (black) peak shape functions. ....14
- Figure 2.7 Transmission geometry set-up for XAFS experiment. ....17

Figure 2.8 (a) Illustration of potential excitations present during XANES spectroscopy experiments. (b) XAFS spectrum of the vanadium edge of  $V_2O_3$  (blue) and  $ScVO_4$  (red).....18

Figure 2.9 (a) Schematic of tube furnace set-up for high temperature synthesis, where gas flow can include either  $H_2$  or  $O_2$  gas. (b) Schematic of tube furnace with quartz tube attached to vacuum pump. ....20

Figure 2.10 Schematic of reconstructive oxidation set-up where the tube furnace starts a room temperature (RT) then is ramped to the target temperature in position 1. Once the tube furnace has reached the target temperature it is moved over the sample to position 2. ....24

Figure 3.1 Illustration of the rhombohedral fluorite  $Sc_4Ti_3O_{12}$  structure (s.g.  $R\bar{3}$ ). Blue =  $Ti^{4+}$ , grey =  $Sc^{3+}$  and pink =  $O^{2-}$  .....27

Figure 3.2 Illustration of the pseudobrookite structure (s.g.  $Cmcm$ ). Dark purple =  $8f$  site, light purple =  $4c$  site, pink = anion. ....27

Figure 3.3 The Rietveld plot of powder x-ray diffraction data for the product of heating 1:1  $Sc_2O_3$  and  $TiO_2$  at  $1200^\circ C$  in air. Refined composition of  $Sc_2O_3 + TiO_2$  at  $1200^\circ C$  was 87.2(2)% pseudobrookite (s.g.  $Cmcm$ ) with rhombohedral phase (s.g.  $R\bar{3}$ ), and bixbyite phase (s.g.  $Ia\bar{3}$ ) impurities. The black closed circles = measured data, red line = fit, blue line = difference, and black, red and blue ticks = Bragg peaks corresponding to pseudobrookite, rhombohedral and bixbyite phases, respectively. ....28

Figure 3.4 The Rietveld plot of x-ray diffraction data obtained from  $Sc_2TiO_5$  fluorite phase (s.g.  $Fm\bar{3}m$ ) where black closed circles = measured data, red line = fit, blue line = difference and black ticks = Bragg peaks corresponding to fluorite phase. ....30

Figure 3.5 Room temperature ex-situ x-ray diffraction data for temperature dependent  $Sc_2TiO_5$  phase evolution.  $Sc_2TiO_5$  was sequentially heated at  $1200^\circ C$  (24 h),  $1500^\circ C$  (24 h),  $1300^\circ C$  (24 h), and  $1100^\circ C$  (48 h). ....31

Figure 3.6 The Rietveld plot of x-ray diffraction data obtained from  $Sc_2TiO_5$  bixbyite phase (s.g.  $Ia\bar{3}$ ) where black closed circles = measured data, red line = fit, blue line = difference and black ticks = Bragg peaks corresponding to bixbyite phase. ....32

Figure 3.7 The Rietveld plot of x-ray diffraction data of  $Sc_2Ti_{0.2}V_{0.8}O_{4.5+\delta}$  ( $x = 0.2$ , s.g.  $Ia\bar{3}$ ) obtained from the reaction between  $Sc_2O_3 + (V_{0.8}Ti_{0.2})_2O_3$  (reaction 2.10) after heating at  $1500^\circ C$  in 5%  $H_2$  for 48 h. Black closed circles = measured data, red line = fit, blue line = difference and black and blue ticks = Bragg peaks corresponding to fluorite and  $Sc_2Si_2O_7$  phases, respectively. The  $Sc_2Si_2O_7$  impurity accounts for 1.2(1)% of the sample. ....33

Figure 3.8 The Rietveld plot of x-ray diffraction data of  $Sc_2Ti_{0.8}V_{0.2}O_{4.5+\delta}$  ( $x = 0.8$ , s.g.  $Ia\bar{3}$ ) obtained from the reaction between  $Sc_2VO_{4.5}$  and  $Sc_2TiO_{4.5+\delta}$  (reaction 2.11) after heating at  $1500^\circ C$  in 5%  $H_2$  for 48 h. Black closed circles = measured data, red line = fit, blue line = difference and black and blue ticks = Bragg peaks corresponding to bixbyite and  $Sc_2Si_2O_7$  phases. ....34

Figure 3.9 The Rietveld plot of x-ray diffraction data collected on tetragonal  $Sc_2Ti_{0.8}V_{0.2}O_{5.1}$  prepared via reconstructive oxidation of the bixbyite  $Sc_2Ti_{0.8}V_{0.2}O_{4.5}$  (reaction 2.17).  $R_{wp}/\chi^2 = 2.90/1.08$ . Black closed circles = measured data, red line = fit, blue line = difference, and black, blue and red ticks = Bragg peaks corresponding to

tetragonal  $I\bar{4}$  81.9(2)%,  $\text{ScVO}_4$  8.7(1)%, and  $\text{Sc}_2\text{Si}_2\text{O}_7$  9.4(1)% phases. The refined composition of this sample was 81.9(2)% tetragonal  $I\bar{4}$ , 8.7(1)%  $\text{ScVO}_4$ , and 9.4(1)%  $\text{Sc}_2\text{Si}_2\text{O}_7$ .....37

Figure 3.10 The Rietveld plots of x-ray diffraction data for tetragonal- $\text{Sc}_2\text{Ti}_x\text{V}_{1-x}\text{O}_{5+\delta}$  phases for  $x = 0.2$  (red), 0.6 (green) and 0.8 (blue). Black closed circles = measured data, coloured line = fit, grey line = difference and black ticks = Bragg peaks corresponding to tetragonal phase (s.g.  $I\bar{4}$ ).....39

Figure 3.11 Comparison of unit cell volume for  $\text{Sc}_2\text{Ti}_x\text{V}_{1-x}\text{O}_{5+\delta}$  ( $x = 0.8, 0.6$  and  $0.2$ ).....41

Figure 3.12 (a) XANES data of the pre-edge/edge region of the titanium K edge (transmission mode) obtained on tetragonal structures  $\text{Sc}_2\text{Ti}_{0.2}\text{V}_{0.8}\text{O}_{5+\delta}$  (dark green circles),  $\text{Sc}_2\text{Ti}_{0.6}\text{V}_{0.4}\text{O}_{5+\delta}$  (black circles),  $\text{Sc}_2\text{Ti}_{0.8}\text{V}_{0.2}\text{O}_{5.1}$  (blue circles), and  $\text{Sc}_2\text{TiO}_5$  (s.g.  $Cmcm$ , red line). (b) XANES data in the pre-edge region of the vanadium K edge (transmission mode) obtained on tetragonal structures  $\text{Sc}_2\text{Ti}_{0.2}\text{V}_{0.8}\text{O}_{5+\delta}$  (purple circles) and  $\text{Sc}_2\text{Ti}_{0.6}\text{V}_{0.4}\text{O}_{5+\delta}$  (black circles), and standards  $\text{ScVO}_4$  (blue circles) and  $\text{V}_2\text{O}_3$  (light green circles). Linear combination of 50:50 and 25:75  $\text{ScVO}_4$  and  $\text{V}_2\text{O}_3$  spectra are modelled by the black and purple lines, respectively. (b) XANES data in the pre-edge/edge region of the vanadium K edge (transmission mode) obtained on tetragonal structure  $\text{Sc}_2\text{Ti}_{0.8}\text{V}_{0.2}\text{O}_{5.1}$  (grey circles) and  $\text{ScVO}_4$  (blue circles).....42

Figure 3.13. Direct current susceptibility measurements for  $\text{Sc}_2\text{V}_{0.8}\text{Ti}_{0.2}\text{O}_{5+\delta}$ . The zero-field cooled data are shown with light blue circles and the black circles represent the inverse susceptibility data and the red line is the fit to the Curie-Weiss law. All data were collected in a 0.1 T field. A diamagnetic contribution of  $-78.6 \times 10^{-6} \text{ emu mol}^{-1}$  was subtracted from the data.....44

Figure 3.14. Illustration of the B-sublattice highlighting vacant anionic sites. (Left) The  $\text{O}^{8g}$  site (green) is located around the  $\text{V}^{2c}$  site. (Right) The  $\text{O}^{2b}$  (yellow) is positioned in the center of the  $\text{V}^{18g}$  tetrahedron. ....45

Figure 4.1 Illustration of the rhombohedral  $\text{Sc}_3\text{CrO}_6$  phase (s.g.  $R\bar{3}$ , #148). Blue =  $\text{Sc}^{3+}$  ( $18f$  site), green =  $\text{Cr}^{3+}$  ( $3a$  and  $3b$  sites), and pink =  $\text{O}^{2-}$  .....47

Figure 4.2 Ternary phase diagram of reported phases in the  $\text{Sc}^{3+} - \text{Cr}^{3+} - \text{V}^{3+}$  oxide system. Where bixbyite, corundum, and  $R\bar{3}$ -type phases are represented by blue squares, red circles, and green triangles, respectively. ....48

Figure 4.3 (Top) Powder X-ray diffractograms for the compositional series  $(\text{Sc}_{1-x}\text{Cr}_x)_2\text{O}_3$ . Blue peaks belong to the bixbyite phase (space group:  $Ia\bar{3}$ ), green peaks belong to  $R\bar{3}$ -type structure and red peaks belong to corundum phases (space group:  $R\bar{3}c$ ). (Bottom) Full Rietveld refinement of the powder X-ray diffraction data for  $(\text{Sc}_{0.8}\text{Cr}_{0.2})_2\text{O}_3$  where black closed circles = measured data, red line = fit, blue line = difference and black ticks = Bragg peaks corresponding to  $R\bar{3}$ -type structure. ....49

Figure 4.4 Ternary phase diagram of reported phases in the  $\text{Sc}^{3+} - \text{Cr}^{3+} - \text{V}^{3+} - \text{O}$  system, including novel  $\text{Sc}_{0.2}\text{Cr}_{1.8}\text{O}_3$  and  $\text{Sc}_{1.6}\text{Cr}_{0.4}\text{O}_3$  phases shown by red open-circle and green open-triangle. Potential corundum region of the phase diagram is shown in red.....50

Figure 4.5 (Top) X-ray diffraction data for  $(\text{Sc}_{0.1}\text{V}_{0.9-x}\text{Cr}_x)_2\text{O}_3$  ( $x = 0.1, 0.4, 0.7, 0.9$ ). (Bottom) Full Rietveld plot for powder X-ray diffraction data for  $(\text{Sc}_{0.1}\text{V}_{0.8}\text{Cr}_{0.1})_2\text{O}_3$  where black closed circles = measured data, red line = fit, blue line = difference and black ticks = Bragg peaks corresponding to corundum phase. ....51

Figure 4.6 Ternary phase diagram of  $\text{Sc}^{3+} - \text{Cr}^{3+} - \text{V}^{3+} - \text{O}$  system. Where bixbyite, corundum and  $R\bar{3}$ -type phases are represented by blue squares, red circles and green triangles, respectively. Open symbols represent compositions contributed by this thesis work. ....52

Figure 4.7 X-ray diffractogram of the products from the reactions of  $0.9 \text{ mol Sc}_2\text{O}_3 + 0.4 \text{ Cr}_2\text{O}_3 + 0.1 \text{ V}_2\text{O}_3$  after heating for 48 h at  $1500^\circ\text{C}$  in a reducing environment (5%  $\text{H}_2$  in  $\text{N}_2$ ). ....53

Figure 4.8 The Rietveld refinement plots of x-ray diffraction data for bixbyite-  $\text{Sc}_2\text{V}_{0.8}\text{Cr}_{0.2}\text{O}_{4.5}$  (s.g.  $Ia\bar{3}$ ) prepared via reaction 2.12. This sample contained a 2%  $\text{Sc}_2\text{Si}_2\text{O}_7$  impurity phase. Black closed circles = measured data, red line = fit, blue line = difference and black ticks = Bragg peaks corresponding to  $Ia\bar{3}$  and blue ticks = Bragg peaks corresponding to  $\text{Sc}_2\text{Si}_2\text{O}_7$  phase. ....55

Figure 4.9 The Rietveld refinement plots of x-ray diffraction data for fluorite-  $\text{Sc}_2\text{V}_{0.8}\text{Cr}_{0.2}\text{O}_{4.5}$  (s.g.  $Fm\bar{3}m$ ) prepared via reaction 2.14. This sample contained a 2.1(6)%  $\text{Sc}_2\text{Si}_2\text{O}_7$  impurity phase. Black closed circles = measured data, red line = fit, blue line = difference and black ticks = Bragg peaks corresponding to  $Fm\bar{3}m$  and blue ticks = Bragg peaks corresponding to  $\text{Sc}_2\text{Si}_2\text{O}_7$  phase.  $\chi^2/R_{\text{wp}} = 2.65/0.98$ . ....56

Figure 4.10 The Rietveld refinement plots of x-ray diffraction data for tetragonal-  $\text{Sc}_2\text{V}_{0.8}\text{Cr}_{0.2}\text{O}_{4.5}$  (s.g.  $I\bar{4}$ ) prepared via direct synthesis method. The Rietveld analysis suggests the sample contains 88.9(1)% tetragonal  $I\bar{4}$  structure and zircon, bixbyite and corundum impurities. Black closed circles = measured data, red line = fit, blue line = difference and ticks = Bragg peaks. ....58

Figure 4.11 The Rietveld refinement of TOF powder neutron diffraction. Black closed circles = measured data, red line = fit, blue line = difference and ticks = Bragg peaks corresponding to respective structure.  $R_{\text{wp}}/\chi^2 = 5.16/6.05$ . 60

Figure 4.12 (Left) XANES data in the pre-edge region of the vanadium K edge obtained on tetragonal  $\text{Sc}_2\text{V}_{0.8}\text{Cr}_{0.2}\text{O}_{5+\delta}$  (red circles), and standards  $\text{ScVO}_4$  (blue circles) and  $\text{V}_2\text{O}_3$  (green circles). Linear combination of 25:75  $\text{ScVO}_4$  and  $\text{V}_2\text{O}_3$  spectra are modelled by the black line. (Right) XANES data of the pre-edge/edge region of the chromium K-edge obtained on tetragonal structures  $\text{Sc}_2\text{V}_{0.8}\text{Cr}_{0.2}\text{O}_{5+\delta}$  (green circles),  $\text{Cr}_2\text{O}_3$  (orange circles) and  $\text{CrO}_2$  (pink circles). Inset highlights the pre-edge peaks and includes linear combination of 75:25  $\text{Cr}_2\text{O}_3$  and  $\text{CrO}_2$  spectra shown by the solid black line. ....61

Figure 4.13 DC magnetometry data. Purple circles represent zero field cooled data. Black circles correspond to the inverse susceptibility of the field cooled data, where the blue line shows linear fit. A diamagnetic contribution of  $-79.2 \times 10^{-6} \text{ emu mol}^{-1}$  was subtracted from the data. ....63

Figure 5.1 Schematic illustration of the process of oxidizing the bixbyite phases to either the tetragonal phase at high temperature (reconstructive oxidation) or the fluorite phase at low temperature (topotactic oxidation). ....66

Figure 5.2 Illustration of structural transition in  $\text{Sc}_2\text{TiO}_5$ , where the anion disordered fluorite structure (s.g.  $Fm\bar{3}m$ ) is found at high temperature and the anion ordered pseudobrookite structure (s.g.  $Cmcm$ ) is found at low temperature. ....67

## List of Tables

Table 3.1 Compositions of 1:1 $\text{Sc}_2\text{O}_3$ and $\text{TiO}_2$ phases after annealing at temperatures between 1100°C and 1500°C.....	28
Table 3.2 Refined structural parameters for pseudobrookite- $\text{Sc}_2\text{TiO}_5$ . The structure was refined in space group $Cmcm$ , $a = 3.84668(2)$ Å, $b = 10.11963(6)$ Å, $c = 10.27596(6)$ Å, and $V = 400.01(4)$ Å <sup>3</sup> . $R_{\text{wp}}/\chi^2 = 2.99/1.09$ . .....	29
Table 3.3 Refined structural parameters for fluorite- $\text{Sc}_2\text{TiO}_5$ . Space group: $Fm\bar{3}m$ , $a = 4.9034(3)$ Å, $V = 177.893$ Å <sup>3</sup> . $R_{\text{wp}}/\chi^2 = 2.47 / 0.86$ . .....	29
Table 3.4 Refined structural parameters for bixbyite- $\text{Sc}_2\text{TiO}_{4.5+\delta}$ . Space group: $Ia\bar{3}$ , $a = 9.78491(8)$ , Å, and $V = 400.01(4)$ Å <sup>3</sup> . $\chi^2/R_{\text{wp}} = 0.94/2.72$ .....	32
Table 3.5 Refined structural parameters for bixbyite- $\text{Sc}_2\text{Ti}_{0.2}\text{V}_{0.8}\text{O}_{4.5+\delta}$ ( $x = 0.2$ , s.g. $Ia\bar{3}$ ). The lattice parameters are refined as $a = 9.6993(4)$ Å, and $V = 912.4(1)$ Å <sup>3</sup> . $R_{\text{wp}}/\chi^2 = 3.10 / 1.14$ . .....	34
Table 3.6 Refined structural parameters for bixbyite- $\text{Sc}_2\text{Ti}_{0.8}\text{V}_{0.2}\text{O}_{4.5+\delta}$ ( $x = 0.8$ , s.g. $Ia\bar{3}$ ). The lattice parameters are refined as $a = 9.698(1)$ Å, and $V = 912.3(2)$ Å <sup>3</sup> . $R_{\text{wp}}/\chi^2 = 5.41 / 1.91$ . .....	35
Table 3.7 Refined structural parameters for tetragonal- $\text{Sc}_2\text{Ti}_{0.8}\text{V}_{0.2}\text{O}_{5.1}$ (s.g. $I\bar{4}$ , $x = 0.8$ ) prepared via direct synthesis. The lattice parameters are refined as $a = 7.80391(4)$ Å, $c = 14.68142(8)$ Å, and $V = 894.11(1)$ Å <sup>3</sup> . $R_{\text{wp}}/\chi^2 = 3.17/1.1$ . .....	38
Table 4.1 Refined structural parameters for $(\text{Sc}_{0.8}\text{Cr}_{0.2})_2\text{O}_3$ . Space group: $R\bar{3}$ (#148), $a = 8.8077(5)$ Å, $c = 10.2119(7)$ Å, and $V = 686.06(1)$ Å <sup>3</sup> . $\chi^2/R_{\text{wp}} = 1.04/2.95$ .....	50
Table 4.2 Refined Structural Parameters for Corundum Phases $(\text{Sc}_{0.1}\text{V}_{0.9-x}\text{Cr}_x)_2\text{O}_3$ for $x = 0.1, 0.4, 0.7, 0.9$ (s.g. $R\bar{3}c$ ).....	52
Table 4.3 Refined structural parameters for bixbyite- $\text{Sc}_2\text{V}_{0.8}\text{Cr}_{0.2}\text{O}_{4.5+\delta}$ . Space group: $Ia\bar{3}$ , $a = 9.68291(6)$ Å, and $V = 907.85(2)$ Å <sup>3</sup> . $\chi^2/R_{\text{wp}} = 0.98/2.79$ . .....	56
Table 4.4 Refined structural parameters for tetragonal- $\text{Sc}_2\text{V}_{0.8}\text{Cr}_{0.2}\text{O}_{5+\delta}$ prepared via direct synthesis. Values were obtained from simultaneous Rietveld Refinement against x-ray and TOF neutron diffraction data. The space group is refined as $I\bar{4}$ (#82), $a = 7.7749(6)$ Å, $c = 14.5867(1)$ Å, and $V = 881.7(2)$ Å <sup>3</sup> . ...	59

## Chapter 1: Introduction

### 1.1 Structure:

***Rational Design of Materials.*** The relationship between a material's structure and properties is highly intertwined. Thus, understanding structure formation is necessary for rational design of functional materials. Solid state materials are ubiquitous in modern technology due to their electronic, magnetic, optic, and catalytic applications. Learning how to control structure will provide a path to tune properties of solid state materials and continue to drive technological innovation forward. Conventional solid state synthesis, commonly termed the “shake-n-bake” method, consists of thoroughly mixing starting materials then heating at high temperatures for long periods of time. This process will find the thermodynamic product of the reaction, yet valuable information of structural formation is absent from this approach.<sup>1</sup> Consequently, the answer to why a specific structure forms is historically left unanswered. This thesis is focused on understanding structure formation and the limits to which structures can be controlled. The following sections outline structures relevant to this work.

***Fluorite.*** The cubic fluorite structure  $\text{AO}_2$  crystallizes in space group  $Fm\bar{3}m$  (#225). The fluorite is a cation ordered and anion disordered structure. Cations form a cubic close packed structure and occupy the  $4a$  site at  $(0, 0, 0)$ . The anions fill tetrahedral holes and occupy the  $8c$  site at  $(\frac{1}{4}, \frac{1}{4}, \frac{1}{4})$ . The fluorite structure is often found for oxide phases where the cation is in the +4-

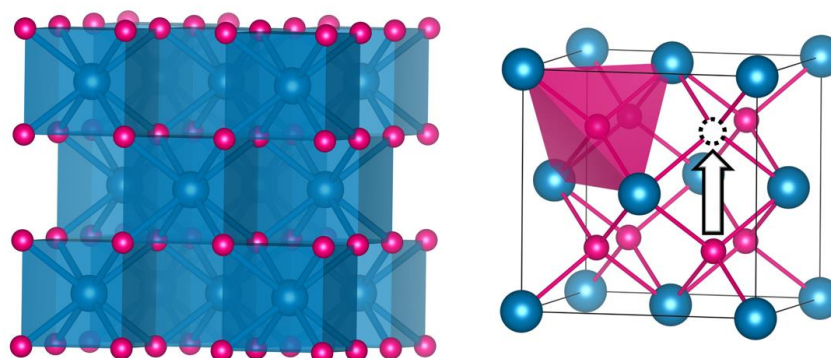


Figure 1.1 Illustration of the cubic fluorite structure (s.g.  $Fm\bar{3}m$ ). Blue =  $4a$  site and pink =  $8c$  site. (Left) Illustration of the cubic fluorite with emphasis on the  $\text{AO}_8$  cubic coordination and its edge sharing interconnectivity (Right) Emphasis on the anionic tetrahedral environment, and illustration of vacancy that can cause oxygen anion-hopping.

oxidation state. The fluorite structure is tolerant to a deficiency of oxygen ions, where oxygen deficient fluorites are termed defect fluorites. The anionic lattice is made up of oxide anions and vacancies. The defect fluorite structure is an ideal structure for the application of solid state electrolytes as the anionic sites are energetically equivalent which can allow for oxygen hopping between vacant sites.

**Tetragonal  $\text{Sc}_2\text{VO}_5$ -type structure.** The tetragonal  $\text{Sc}_2\text{VO}_5$ -type structure is a fluorite-based superstructure that crystallizes in space group  $\bar{I}4$  (#82). The  $\text{Sc}_2\text{VO}_5$  structure was first reported in 1971 and was later revisited by Cong *et al.* in 2010.<sup>2,3</sup> Cong *et al.* identified that this structure consists of scandium and vanadium sublattices. There are three positions on the scandium sublattice:  $\text{Sc}1^{4f}$ ,  $\text{Sc}2^{8g}$ ,  $\text{Sc}3^{8g}$ . The  $4f$  site, at coordinates  $(0, \frac{1}{2}, z)$ , is in a distorted cubic environment, and the  $8g$  sites, at coordinates  $(x, y, z)$ , are 7-fold coordinated. Of particular interest, the vanadium sublattice is comprised of two distinct positions of octahedral and tetrahedral environments. The octahedral position is labelled  $\text{V}1^{8g}$  and occupies the  $8g$  site  $(x, y, z)$ . Whereas the tetrahedral site is labelled  $\text{V}2^{2c}$  and occupies the  $2c$  position at  $(0, \frac{1}{2}, \frac{1}{4})$ . A recent report by Vrublevskiy *et al.* found a mixture of  $\text{V}^{3+/4+}$  is located on the octahedral position and  $\text{V}^{5+}$  is located on the tetrahedral position, and the structure is best written as  $\text{Sc}_2\text{V}_{0.8}^{3+/4+}\text{V}_{0.2}^{5+}\text{O}_{5+\delta}$ .<sup>4</sup> The  $\text{V}1^{8g}$  octahedra form tetrahedral clusters that are interconnected via  $\text{V}^{5+}$  in the  $\text{V}'\text{O}_4$  tetrahedra. Notably, the  $\text{V}^{3+}:\text{V}^{4+}$  ratio on the  $\text{V}1^{8g}$  site can be varied to tune the oxygen stoichiometry. The  $\text{Sc}_2\text{VO}_5$ -type structure will be referred to as the tetragonal  $\bar{I}4$  structure throughout this thesis.

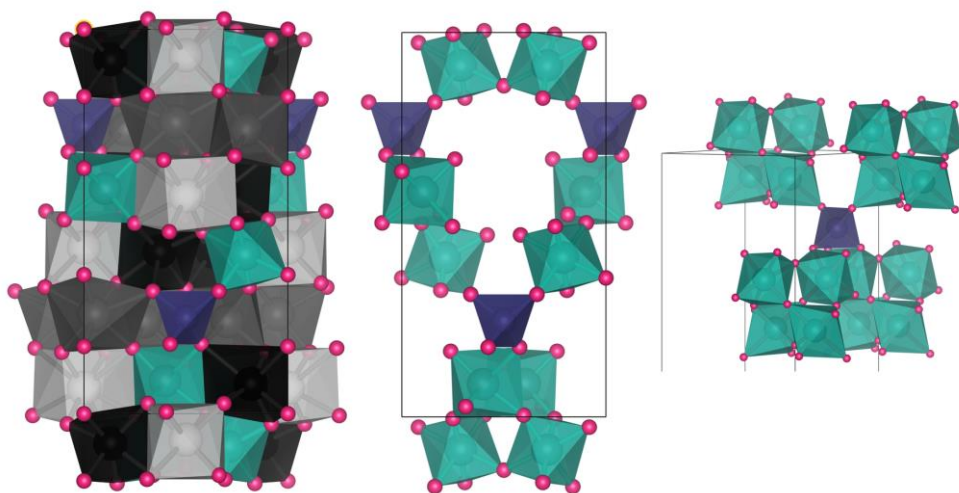


Figure 1.2 Illustration of the tetragonal  $\text{Sc}_2\text{VO}_5$  structure (s.g.  $\bar{I}4$ ). (Left) Total structure, (middle) B-sublattice; and (right) B-sublattice extending beyond the unit cell to highlight the  $\text{V}1^{8g}$  clusters connected by the tetrahedral  $\text{V}2^{2c}$  site. White =  $\text{Sc}1^{4f}$  site, dark grey =  $\text{Sc}2^{8g}$  site, light grey =  $\text{Sc}3^{8g}$  site, teal =  $\text{V}1^{8g}$  site, and dark blue =  $\text{V}2^{2c}$  site.

**Bixbyite.** The cubic bixbyite  $A_2O_3$  structure crystallizes in space group  $Ia\bar{3}$  (#206). Cations are 6-fold coordinated and are located on two distinct crystallographic sites,  $8a$  and  $24d$  sites. This structure closely resembles the fluorite; however, the anionic lattice and anionic vacancies are ordered within the bixbyite. The anions occupy the  $48e$  site. The bixbyite can undergo topotactic oxidation where additional oxygen can be added to the  $16c$  position. Complete oxidation of the bixbyite phase will result in the formation of the fluorite phase.

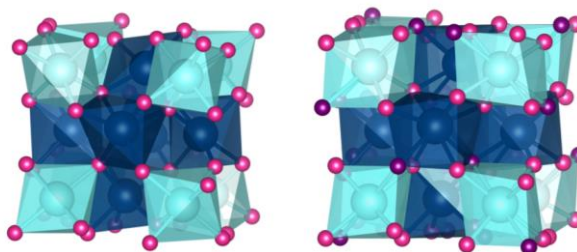


Figure 1.3 Illustration of bixbyite structure (s.g.  $Ia\bar{3}$ ); and (right) topotactically oxidized product where additional oxygen anions are present in the  $16c$  site. Dark blue =  $24d$  site, light blue =  $8a$  site, pink =  $48e$  site, and purple =  $16c$

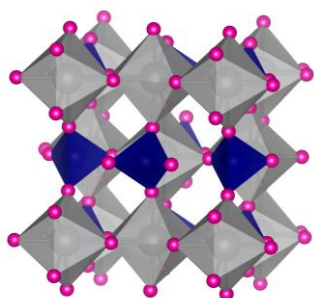


Figure 1.4 Illustration of zircon structure (s.g.  $I4_1/amd$ ). Grey =  $4b$  site, blue =  $4a$  site, and pink =  $16h$  site.

**Rutile.** The tetragonal rutile structure crystallizes in space group  $P4_2/mnm$  (#136). This structure is composed of corner sharing octahedra where cations (often tetravalent) occupy the  $2a$  site at coordinates  $(0, 0, 0)$  and anions occupy the  $4f$  site at coordinates  $(x, x, 0)$ .  $TiO_2$  and  $VO_2$  are common phases which crystallize as a rutile phase.

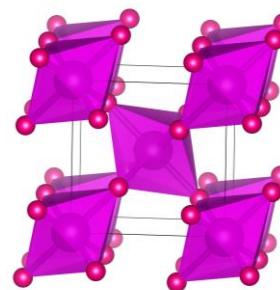


Figure 1.5 Illustration of rutile structure (s.g.  $P4_2/mnm$ ). Purple = cation  $2a$  site and pink = anion  $4f$  site.

**Corundum.** The rhombohedral corundum structure crystallizes in space group  $R\bar{3}c$  (#167). The oxide anions form a hexagonal close packed array and cations are found in two thirds of the octahedral sites. Vacant cation sites are situated in a manner that allows for face-sharing octahedra along the c-axis and edge-sharing octahedra along layers in the ab-plane. Many transition metal oxides crystallize in the corundum structure;  $V_2O_3$ ,  $Ti_2O_3$  and  $Cr_2O_3$  are a few examples relevant to this work.

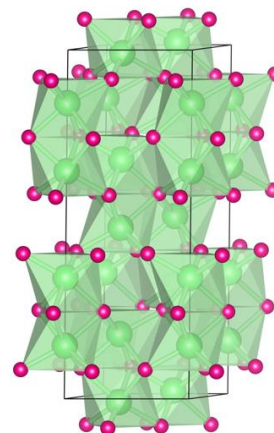


Figure 1.6 Illustration of corundum structure (s.g.  $R\bar{3}c$ ). Green =  $12c$  site and pink =  $18e$  site.

## 1.2 Scandium Vanadate Family of Structures:

Size, charge, and oxygen content play a vital role in the type of structure that is formed. The scandium vanadate family of phases exemplifies this statement. The scandium vanadates are a diverse family of compounds where phase preference is owed to the oxidation state of vanadium. Vanadium is a versatile cation that is stable in the +3, +4, and +5 -oxidation states. In the scandium vanadate system, when  $V^{5+}$  is present a cation-ordered zircon structure is favoured due to the large size and charge difference between  $Sc^{3+}$  and  $V^{5+}$ . In contrast, when vanadium is in the +3 or +4 -

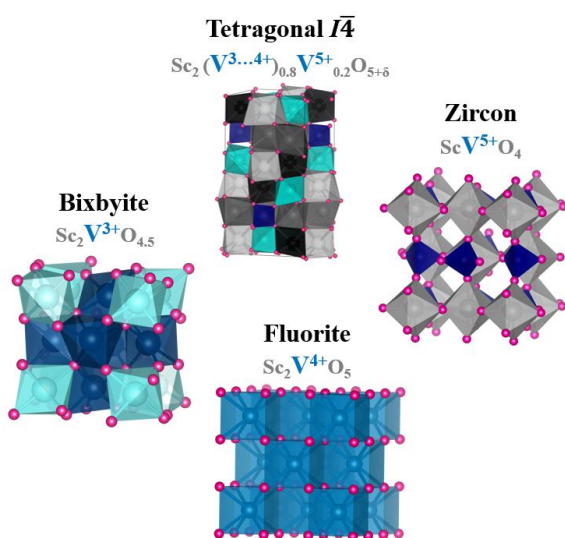


Figure 1.7 Illustration of the impact of oxidation state of vanadium on structure formation in the scandium vanadate family of phases.

oxidation state, due to its similar size and charge to  $Sc^{3+}$  a cation-disordered phase will be favoured. The cation-disordered phase could either be the fluorite ( $V^{4+}$ ) or bixbyite ( $V^{3+}$ ) structure, where the structure depends on the charge of vanadium and consequently the amount of oxygen content within the structure. An interesting structure is found when +3, +4, and +5 -oxidation states are simultaneously present. This scenario is found for the composition  $Sc_2VO_5$  and crystallizes in a tetragonal  $I\bar{4}$  structure. Vrublevskiy *et al.* provided a detailed report of the structural

complexity of this phase.<sup>4</sup> This report also highlighted how the structure can be selected through control of the valency of vanadium where redox chemistry plays a central role in navigating between structures in the scandium vanadate family. Illustration of the relationship between structures and vanadium oxidation states is shown in figure 1.7.

### 1.3 Objective & Motivation:

The ordered-tetragonal  $\text{Sc}_2\text{VO}_5$  structure provides an intriguing framework that requires further investigation. The vanadium sublattice with the ordered tetragonal structure consists of two distinct crystallographic sites,  $\text{V1}^{8g}$  and  $\text{V2}^{2c}$ , and the large difference in size suggests these sites are individually controllable.  $\text{Ti}^{4+}$  is first considered as a potential candidate to occupy the octahedral  $\text{V1}^{8g}$  site.  $\text{Ti}^{4+}$  is an ideal candidate for substitution into the  $\text{V1}^{8g}$  site as it is of an intermediate size between  $\text{V}^{3+}$  and  $\text{V}^{4+}$ , meaning the average size of the  $\text{V1}^{8g}$  site will remain nearly constant ( $\text{Ti}^{4+}$   $r(\text{IV}) = 0.605 \text{ \AA}$ ;  $\text{V}^{3+}$   $r(\text{IV}) = 0.64 \text{ \AA}$ ;  $\text{V}^{4+}$   $r(\text{IV}) = 0.58 \text{ \AA}$ ).<sup>5</sup> In addition,  $\text{Ti}^{4+}$  has a low tendency to be tetrahedrally coordinated with oxygen, thus it is unlikely to occupy the tetrahedral  $\text{V2}^{2c}$  site. The substitution of  $\text{Ti}^{4+}$  into the  $\text{V1}^{8g}$  site of the ordered-tetragonal structure would provide evidence that the octahedral  $\text{V1}^{8g}$  and the tetrahedral  $\text{V2}^{2c}$  sites are individually controllable.

The synthesis of the tetragonal  $I\bar{4}$  structure will also provide insight to synthetic optimization of solid state electrolytes used in solid oxide fuel cells. The defect fluorite structure is a promising archetype for the design of solid state electrolytes. In particular, the defect fluorites  $\text{ScVO}_{3.5}$  and  $\text{ScTiO}_{3.5}$  are potential materials for solid state electrolytes.<sup>6,7</sup> The random arrangement of oxygen vacancies on the anionic lattice allows for oxygen migration due to the equivalent energy of anionic positions. In contrast, the tetragonal  $I\bar{4}$  structure contains an ordered anionic lattice, consequently oxide ions are unable to hop throughout the structure. Formation of the ordered tetragonal phase during the synthesis of a solid state electrolyte would in turn prevent ion conduction. Understanding reaction pathways of ordered structures provides valuable information on how to avoid competing phases during the synthesis or operation of solid state electrolytes.

The vanadium sublattice within the tetragonal  $I\bar{4}$  structure is of particular interest for magnetism due to its network of triangular motifs of paramagnetic cations. The octahedral  $V1^{8g}$  sites form clusters that are linked together with the  $V2^{2c}$  site. Notably, the  $V1^{8g}$  sites form tetrahedral clusters that may exhibit geometric magnetic frustration if the  $V1^{8g}$  site is occupied with paramagnetic species, see figure 1.8. Here geometric frustration refers to a phenomenon caused by competing interactions due to lattice topology and magnetic exchange between spins. Geometric frustration is often found in systems where antiferromagnetic interactions are constrained to a triangular lattice which prevents magnetic moments from ordering.<sup>8</sup> Consequently, the system is forced to make energetic compromises to find a cooperative ground state. This energetic compromise often leads to exotic magnetic ground states, such as the spin glass state where magnetic spins freeze in random orientations, or the spin liquid state where spins remain dynamic, or fluid-like, down to zero Kelvin.<sup>9,10</sup>

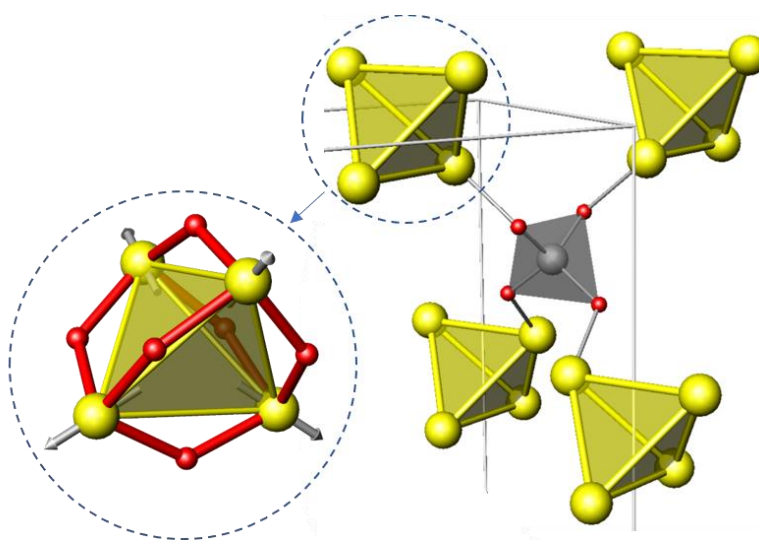


Figure 1.8  $V_4$  clusters (yellow) connected by  $V'O_4$  tetrahedra,  $V'$ =grey,  $O$ =red. Left insert:  $V$ - $O$  bonds and frustrated nature of  $V_4$  clusters. Magnetic spins shown by grey arrows depict a potential ground state. This is one possible spin structure due to the tetrahedral motif.

In the tetragonal- $Sc_2VO_5$  structure, the  $V2^{2c}$  site is occupied by diamagnetic  $V^{5+}$ . Substitution of  $V^{5+}$  with a paramagnetic cation, such as  $Cr^{5+}$ , provides a pathway to tune magnetic interactions within the structure. Spin-1/2 chromium(V) is a potential candidate to occupy the  $V2^{2c}$  site as it has a similar charge and ionic radius to  $V^{5+}$  ( $r(IV) V^{5+}=0.355\text{\AA}$ ,  $r(IV) Cr^{5+}=0.345\text{\AA}$ ).<sup>5</sup> The low spin quantum number ( $S = 1/2$ ) of  $Cr^{5+}$  is advantageous as it has been proposed that the spin liquid ground state is expected to be found in materials with low spin quantum numbers

occupying geometrically frustrated sites.<sup>11</sup> Therefore, targeted substitution of chromium to the tetrahedral V2<sup>2c</sup> site provides a promising route to probe interesting magnetic ground states.

This thesis investigates a series of Sc<sub>2</sub>V<sub>1-x</sub>M<sub>x</sub>O<sub>5+δ</sub> (M = Ti and Cr) phases. This work seeks the targeted synthesis of the tetragonal  $I\bar{4}$  phase with Ti<sup>4+</sup> on the octahedral V1<sup>8g</sup> site: Sc<sub>2</sub>(Ti<sub>0.8</sub>)<sup>8g</sup>(V<sub>0.2</sub>)<sup>2c</sup>O<sub>5.1</sub>, and the ordered-tetragonal phase with Cr<sup>5+</sup> on the tetrahedral V2<sup>2c</sup> site: Sc<sub>2</sub>(V<sub>0.8</sub>)<sup>8g</sup>(Cr<sub>0.2</sub>)<sup>2c</sup>O<sub>5+δ</sub>. Thorough investigation of the Sc<sub>2</sub>V<sub>1-x</sub>M<sub>x</sub>O<sub>5+δ</sub> (M = Ti and Cr) phases is required as Sc-V-Ti and Sc-V-Cr oxide systems have not previously been explored. Understanding of structures available in these systems is necessary to avoid potential competing phases during the synthesis of the tetragonal  $I\bar{4}$  structure. Chapter 3 focuses on substituting titanium into the scandium vanadate family of structures and Chapter 4 considers the substitution of chromium.

## Chapter 2: Experimental

### 2.1 Techniques:

#### 2.1.1 Diffraction.

Diffraction occurs due to the uniform spacing of atoms within a crystalline material. Crystalline materials can be described as three-dimensional diffraction gratings, where virtually defined lattice planes diffract incident waves according to Bragg's law. Bragg's law (eqn. 2.1) correlates the wavelength ( $\lambda$ ) of diffracted monochromatic wave, the distance ( $d_{hkl}$ ) between planes, and the incident angle ( $\theta$ ) of the wave as depicted in figure 2.1. Bragg's law holds when waves scattered from successive planes travel in phase. This results in constructive interference and produces a Bragg peak at angle  $2\theta$  with respect to the incident beam.

$$n\lambda = 2d\sin\theta \quad (\text{eqn. 2.1})$$

$$\frac{1}{d_{hkl}} = \sqrt{\frac{h^2}{a^2} + \frac{k^2}{b^2} + \frac{l^2}{c^2}} \quad (\text{eqn. 2.2})$$

Miller indices describe lattice planes within the crystal structure, and are determined by the integers  $h$ ,  $k$ , and  $l$ . Planes with the same Miller indices must be parallel to each other and equally spaced. The  $hkl$  integer values indicate the reciprocal values at which their planes intercept the crystal lattice. For cubic, tetragonal, and orthorhombic crystal systems, where  $\alpha = \beta = \gamma = 90^\circ$ , equation 2.2 describes the relationship of d-spacing and the lattice dimensions of the unit cell.<sup>12</sup>

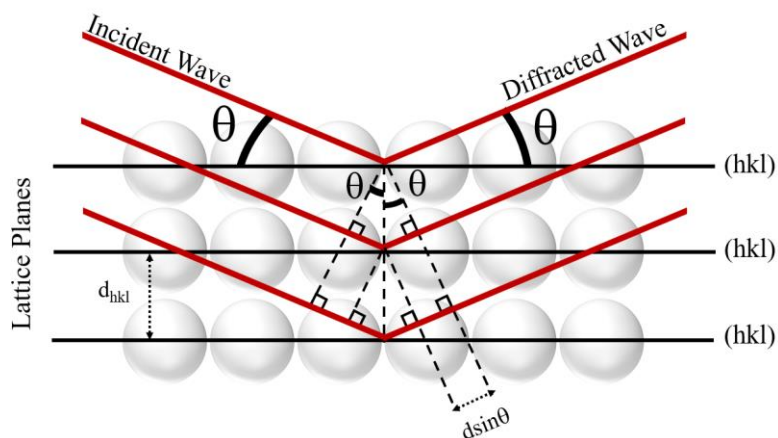


Figure 2.1 Diffraction of x-rays from a lattice and illustration of the geometric derivation of Bragg's Law.

Diffractograms of different structures can differ in terms of peak position (i.e. d-spacing) and relative peak intensity. The size and shape of the unit cell, and the identity and position of the atoms in the cell will result in these differences. The d-spacings provide information related to lattice parameters and space group, whereas relative peak intensities relate to the unit cell content. An example x-ray diffractogram is shown in figure 2.2.

Diffraction experiments can either be conducted on a single crystal or polycrystalline (powder) sample. Powder diffraction assumes that the number of crystallites approaches infinity and orientation of crystallites is completely random. This implies a statistically significant number of each plane of the crystal structure will be in a proper orientation to diffract.<sup>12</sup> Diffraction experiments can use x-rays, neutrons, or electrons as probes. In this thesis work, x-rays and neutrons are used for structural determination of polycrystalline materials.

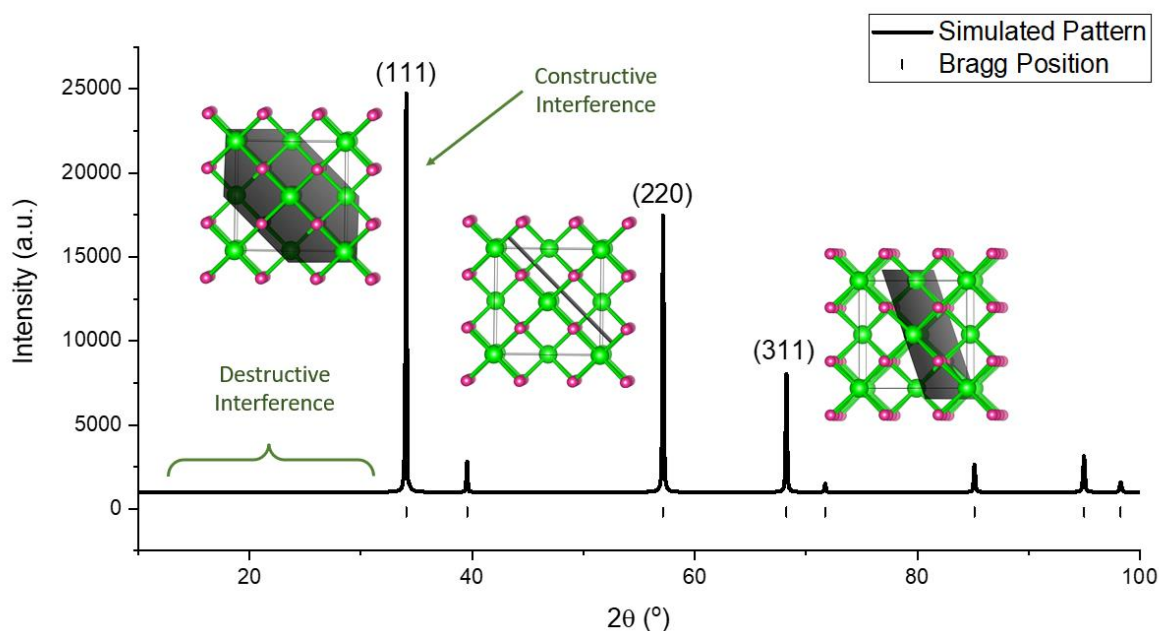


Figure 2.2 Simulated x-ray diffractogram of fluorite structure (s.g.  $Fm\bar{3}m$ , #225) highlighting destructive and constructive interferences. Calculated pattern = black line; and black ticks = Bragg peak positions. Simulated structures depicting lattice planes corresponding to the major Bragg peaks are included.

### 2.1.2 Powder X-ray Diffraction.

Powder x-ray diffraction (PXD) is the primary characterization technique of structures in this thesis. In PXD, the intensity of a diffraction peak,  $I_{hkl}$ , is proportional to the square modulus of its structure factor (eqn. 2.3). The structure factor is defined in equation 2.4, where  $F_{hkl}$  is the structure factor of reflection ( $hkl$ );  $f_n$  is the atomic form factor;  $h$ ,  $k$ , and  $l$  are the Miller indices that describe the diffracting plane; and  $x_n$ ,  $y_n$  and  $z_n$  are the fractional coordinates of an atom,  $n$ . The summation occurs over the entire unit cell meaning every atom/ion in the unit cell is considered.

$$I_{hkl} \propto |F_{hkl}|^2 \quad (\text{eqn. 2.3})$$

$$F_{hkl} = \sum_{n=1}^N f_n(2\theta) \exp[i2\pi(hx_n + ky_n + lz_n)] \quad (\text{eqn. 2.4})$$

The atomic form factor,  $f_n$ , is described as the x-ray scattering power of an atom or ion. The atomic form factor is a function of diffraction angle. For  $2\theta = 0^\circ$ ,  $f_n$  is equal to the number of electrons in the atom or ion. The scattering power decreases as  $2\theta$  increases. As the scattering intensity is directly related to the electron density of an atom, two challenges arise: (1) atoms of similar electron density are nearly indistinguishable from each other; and (2) atoms with low electron density are effectively hidden by the atoms with higher electron density. This means site occupancy of atoms of similar electron density will be challenging to determine. As well as determining crystallographic positions and site occupancy of atoms with low electron density, for example oxygen in the presence of heavy metals will be difficult with PXD. Figure 2.3 plots  $f_n$  as a function of  $2\theta$  for atoms considered in this thesis and highlights the similar scattering power of these elements.

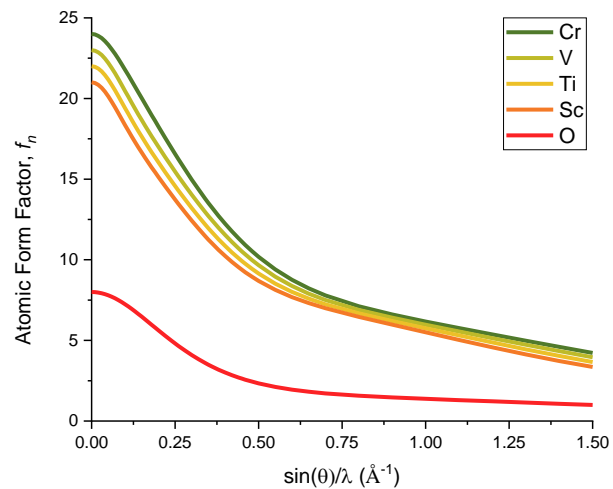


Figure 2.3 The dependence of atomic number on the x-ray scattering factor as a function of scattering angle.<sup>13</sup>

Conventional laboratory x-rays are commonly produced via an x-ray tube. An

x-ray tube produces electromagnetic waves from impacts of high energy electrons with a metal target. The identity of the metal will determine the wavelength of radiation produced, where Cu is most used in laboratory powder diffractometers.

### 2.1.3 Neutron Diffraction.

Neutrons can also be used as diffraction probes. Due to the wave-particle duality, a desired wavelength can be achieved using either electromagnetic radiation (as used in x-ray diffraction) or particles in motion as used in neutron diffraction. The de Broglie equation relates mass,  $m$ , and velocity,  $v$ , of a particle to an associated wavelength,  $\lambda$  (eqn. 2.5). Thus, by selecting a certain speed of neutrons, a particular wavelength can be selected.

$$\lambda = \frac{h}{mv} \quad (\text{eqn. 2.5})$$

Neutron powder diffraction (NPD) is a complementary technique to x-ray diffraction due to the fundamental differences in how neutrons interact with atoms. Comparison of x-ray and neutron scattering intensity of atoms used in this thesis are depicted in figure 2.4. Unlike x-rays that diffract due to the electron density of the atom neutrons scatter from nuclei. The strength of the interaction between the neutron and ion is described by the neutron scattering length,  $b$ . The neutron scattering length,  $b$ , varies among elements and their isotopes, and as a result different elements scatter and absorb neutrons differently. A comprehensive list of neutron scattering lengths was reported in 1992 by Sears.<sup>14</sup> The structure factor with respect to neutron diffraction is expressed in equation 2.6. Notably the neutron scattering length is not a function of  $2\theta$ ; thus, the neutron scattering lengths do not contribute to the decrease of peak intensities at high angle.

$$F_{hkl} = \sum_{n=1}^N b \exp[i2\pi(hx_n + ky_n + lz_n)] \quad (\text{eqn. 2.6})$$

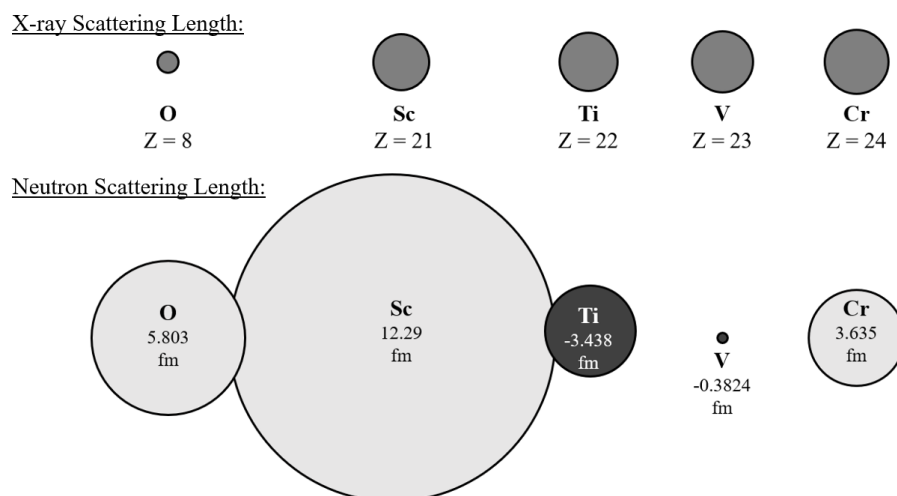


Figure 2.4 Comparison of scattering lengths from neutron and x-ray diffraction where the diameter of the circle is proportional to the atomic scattering length. X-ray form factors are reported at  $2\theta = 0^\circ$ , and neutron scattering length  $b$  is obtained from Sears.<sup>11</sup> Note:  $1 \text{ fm} = 1 \times 10^{-15} \text{ m}$ .

Neutrons can be produced either by fission or spallation. Neutron diffraction experiments in this thesis were conducted at Oak Ridge National Lab (ORNL) and data were collected on POWGEN (BL-11A), where neutrons are produced by spallation. A spallation neutron source (SNS) produces packets of neutrons by bombarding a heavy-metal target with pulses (60 per second) of negatively charged-hydrogen ions travelling at 88% of the speed of light.<sup>15</sup> Neutrons produced through this process are slowed down in a moderator and guided through beamlines to a variety of instruments. One such instrument is the time-of-flight (TOF) diffractometer. The TOF diffractometers use the function of time to select a central wavelength for the experiment. The de Broglie's equation (eqn 2.5) can be expressed with respect to time as shown in equation 2.7 where wavelength is related also to Bragg's Law (eq. 2.1) as shown by:

$$\lambda = \frac{ht}{mL} = 2d\sin\theta \quad (\text{eqn. 2.7})$$

where  $m$  is the mass of a neutron,  $h$  is Planck's constant,  $t$  is the time-of-flight,  $L$  is the total flight path (source to detector),  $\theta$  is the angular detector position, and  $d$  is the interatomic spacing in the crystal structure. Therefore, time-of-flight,  $t$ , can now be expressed as:

$$t = KLd\sin\theta \quad (\text{eqn. 2.8})$$

where  $K = 2m/h = 505.554 \mu\text{s m}^{-1} \text{ \AA}^{-1}$  for neutrons. In TOF neutron diffraction, the detectors are fixed at known angles. As the angular detector position, distance from source to detector, and the starting time of the neutron pulse are known, the time-of-flight can be easily calculated using equation 2.8. Each time a neutron arrives at the detector, the time is registered. Neutron diffractograms often report intensity (y-axis) as a function of time-of-flight or d-spacing (x-axis).

The POWGEN TOF diffractometer is depicted in figure 2.5. The instrument includes a 60 m flight path between the moderator and sample. The instrument includes a chopper system that

consist of a  $T_0$  chopper

and three bandwidth

(BW) choppers.  $T_0$  is

needed to cut out the

very high energy

prompt pulse neutrons

which otherwise would

travel to the instrument

and cause increased

background levels.<sup>16</sup>

Control of choppers

allows for distinct

packets of neutrons to

be selected. The frequency and phase of the 3 BW choppers are used to set the incident wavelength bandwidth and center, respectively.<sup>12</sup>

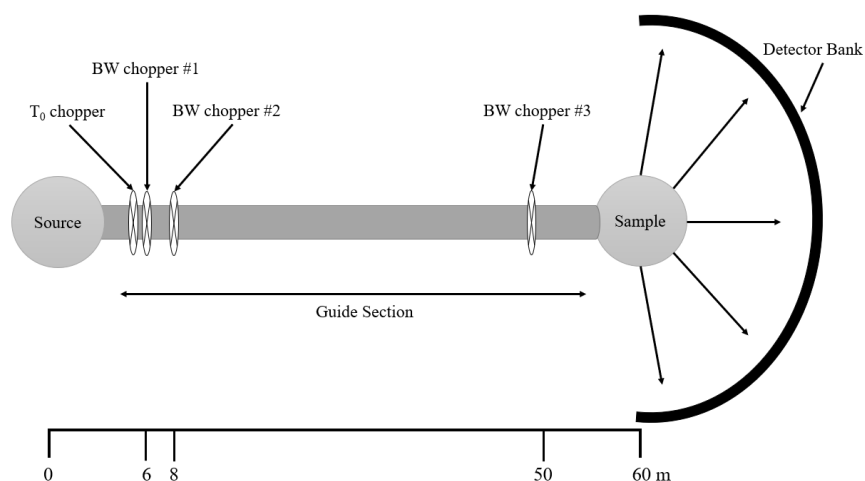


Figure 2.5 Schematic of POWGEN beamline annotated with major components.

#### 2.1.4 Rietveld Refinement.

**Least Squares Minimization.** The aim of the Rietveld refinement method is to obtain a calculated pattern that most closely resembles the experimental pattern. The Rietveld method proceeds by solving a system of equations by using non-linear least squares minimization.<sup>17</sup> The minimized function,  $\Phi$ , in the Rietveld method is given by:<sup>12</sup>

$$\Phi = \sum_{i=1}^n \omega_i (Y_i^{obs} - Y_i^{calc})^2 \quad (\text{eqn. 2.9})$$

where  $Y_i^{obs}$  is the measured intensity at point  $i$  in the diffractogram,  $Y_i^{calc}$  is the calculated intensity, and  $w_i$  is defined as  $[Y_i^{obs}]^{-1}$ , and summation is carried out over all measured data points. The number of points,  $n$ , often varies from  $10^3$ - $10^4$  data points for a typical powder diffraction experiment. The calculated intensity at each point is determined by the structure factor,  $|F_{hkl}|^2$ , and is adjusted by other parameters.  $Y_i^{calc}$  is calculated via the following equation:<sup>17</sup>

$$Y_i^{calc} = s \sum_{hkl} L_{hkl} |F_{hkl}|^2 \Phi P_{hkl} A + y_{bi} \quad (\text{eqn. 2.10})$$

where:

$s$  is the scale factor;

$L_{hkl}$  contains the Lorentz, polarization, and multiplicity factors;

$\Phi$  is the reflection profile function, which describes peak shape;

$P_{hkl}$  is the preferred orientation function;

$A$  is an absorption factor;

$|F_{hkl}|^2$  is the structure factor for the  $hkl$  Bragg reflection; and

$y_{bi}$  is the background intensity of the  $i^{\text{th}}$  step.

Rietveld analysis can be used to model multiphase diffractograms. Multiple phases can contribute to the intensity of each point. Thus, the total  $Y_i^{calc}$  is calculated by the weighted sum of the phases during a multiphase refinement.

**Peak Shape.** The peak shape in an experimental diffractogram is a function of the sample and instrumental factors.<sup>18</sup> The Lorentz, Gauss, and Pseudo-Voigt functions are three commonly used functions used to model peak shape in a diffractogram, though other functions exist as well. Figure 2.6 compares the peak shape of the Gauss and Lorentz functions, notably the Lorentz function consists of long tails on either side of the maximum, and the Gauss function does not exhibit these tails. Often, experimental data require both Gauss and Lorentz functions to be considered to accurately describe experimental peak shape.<sup>12</sup> This can be applied by convoluting both functions; or by using the Pseudo-Voigt function which accounts for both Gauss and Lorentz functions. In this work,

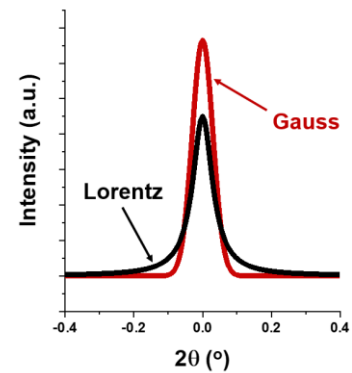


Figure 2.6 Illustration of Gauss (red) and Lorentz (black) peak shape functions.

convolution of Gauss and Lorentz functions were used to model x-ray diffraction data, and Pseudo-Voigt function was used for neutron diffraction data.

The Lorentz, Gauss, and Pseudo-Voigt peak shape functions are centrosymmetric however experimental data often includes peak asymmetry. Peak asymmetry in experimental data is often due to various instrumental factors, such as axial divergence and nonideal specimen geometry, and due to non-zero curvature of Debye rings.<sup>12</sup> Consequently, peak asymmetry must also be considered when refining diffraction data.

There are many programs capable of performing Rietveld analysis; two commonly used software programs are FullProf Suite<sup>19</sup> and TOPAS,<sup>20</sup> and each handle peak asymmetry differently. Fullprof Suite is a commonly used program for Rietveld refinement. One method FullProf uses to model peak asymmetry is by applying a peak asymmetry term which adjusts asymmetry as a function of Bragg angle. This term is used as a heuristic to simulate peaks that best fit the experimental data. Rietveld refinements in this thesis were carried out with TOPAS software. In contrast to FullProf, TOPAS uses the fundamental parameters (FPPF) approach. The FPPF approach to line profile fitting uses physical models to generate the line profile shapes.<sup>21</sup> This approach uses refined parameters which are determined by the diffractometer configuration.<sup>20</sup>

**Figures of Merit.** The quality of a refinement is quantified by figures of merit. Commonly used figures of merit include weighted profile residual ( $R_{wp}$ ), expected profile residual ( $R_{exp}$ ), and goodness of fit ( $\chi^2$ ).  $R_{wp}$ ,  $R_{exp}$ , and  $\chi^2$  are calculated via equations 2.11 – 2.13, where  $Y_i^{calc}$  and  $Y_i^{obs}$  are the calculated and observed intensity of the  $i^{th}$  point, respectively,  $w_i$  is the weight of the  $i^{th}$  point which is equal to  $1/Y_i^{obs}$ ,  $n$  is the total number of points collected in the experimental powder diffractogram, and  $p$  is the number of free least squares parameters. Ideally,  $\chi^2$  should approach unity, however experimental factors such as background and signal to noise ratio may prevent this.<sup>12</sup> Quality of refinements must always be assessed with an understanding of the origin of physical data. A common pitfall during refinements is to over-refine parameters to obtain a satisfactory figure of merit; this comes at the cost of yielding a meaningful calculated structure.

$$R_{wp} = \left[ \frac{\sum_{i=1}^n w_i (Y_i^{obs} - Y_i^{calc})^2}{\sum_{i=1}^n w_i (Y_i^{obs})^2} \right]^{\frac{1}{2}} \times 100\% \quad (\text{eqn. 2.11})$$

$$R_{exp} = \left[ \frac{n - p}{\sum_{i=1}^n w_i (Y_i^{obs})^2} \right]^{\frac{1}{2}} \times 100\% \quad (\text{eqn. 2.12})$$

$$\chi^2 = \frac{\sum_{i=1}^n w_i (Y_i^{obs} - Y_i^{calc})^2}{n - p} \times 100\% = \left[ \frac{R_{wp}}{R_{exp}} \right]^2 \quad (\text{eqn. 2.13})$$

### 2.1.5 Direct Current Magnetic Susceptibility.

The magnetic susceptibility is defined as the change in magnetization with respect to changing applied magnetic field as described by equation 2.14, where  $\chi$  is the magnetic susceptibility,  $M$  is the sample magnetization and  $H$  is the applied magnetic field.<sup>22</sup> While in the paramagnetic regime, the Curie-Weiss law can be applied (eqn. 2.15), where  $\theta$  is the Curie-Weiss temperature,  $C$  is the Curie constant, and  $T$  is the temperature in Kelvin.

$$\chi = \frac{dM}{dH} \quad (\text{eqn. 2.14})$$

$$\chi = \frac{C}{T - \theta_{CW}} \quad (\text{eqn. 2.15})$$

The Curie-Weiss temperature,  $\theta_{CW}$ , represents the strength of the net correlations between magnetic moments. Positive Curie-Weiss temperature indicates a net ferromagnetic interaction, whereas a negative Curie-Weiss temperature indicates a net antiferromagnetic interaction. The Curie constant,  $C$ , is related to the effective magnetic moment,  $\mu_{eff}$  and the spin quantum number (assuming a spin-only system),  $S$ , as shown in equation 2.16 where  $k_B$  is Boltzmann's constant ( $1.381 \times 10^{-23} \text{ m}^2 \text{ kg s}^{-2} \text{ K}^{-1}$ ) and  $N_A$  is Avogadro's number ( $6.022 \times 10^{23} \text{ mol}^{-1}$ ). Thus, the Curie constant can be written with respect to the spin quantum number,  $S$  (equation 2.17). The Curie constant is additive amongst cations in a system; therefore, the  $C_{total}$  is calculated by the weighted sum of  $C$  for each unique spin quantum number in the material. Finding the experimental  $C$  of a material permits calculation of the spin quantum number of cations and consequently cation oxidation states can be derived.

$$\mu_{eff} = \sqrt{\frac{3k_B C}{N_A}} = 2\sqrt{S(S + 1)} \quad (\text{eqn. 2.16})$$

$$C = \frac{[2\sqrt{S(S+1)}]^2 \cdot N_A}{3k_B} \quad (\text{eqn. 2.17})$$

Magnetic susceptibility data in this thesis were collected using a Quantum Design Physical Property Measurement System with the Vibrating Sample Magnetometer (VSM) insert. The VSM measurement is accomplished by oscillating the sample near a detection coil and synchronously detecting the voltage induced. The VSM utilizes a linear motor to vibrate the sample with an oscillation amplitude of 1-3 mm at a frequency of 40 Hz.<sup>23</sup> This system allows for resolution of magnetization changes of less than  $10^{-6}$  emu at a data collection rate of 1 point per second.<sup>23</sup>

### 2.1.6 X-ray Absorption Spectroscopy.

X-ray absorption fine structure (XAFS) is a spectroscopic technique that is element specific and is sensitive to the oxidation state, bonding environment and local geometry around the absorbing atom.<sup>24</sup> During an x-ray absorption experiment, a sample is bombarded with x-rays of a selected energy. Absorption of x-rays by the sample causes the excitation of a core electron. Absorption can be quantified by comparing the intensity of the incident beam to that of the transmitted beam. Figure 2.7 displays the geometry of an XAFS experiment. X-ray absorption spectroscopy investigates how the absorption coefficient,  $\mu$ , changes with energy. A spectrum is obtained by slightly changing the incident energy and measuring the intensity of the transmitted beam. The absorption coefficient can be approximated via equation 2.18 and depends on the sample density,  $\rho$ , the atomic number,  $Z$ , the atomic mass,  $A$ , and the x-ray energy.

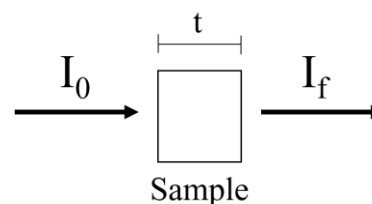


Figure 2.7. Transmission geometry set-up for XAFS experiment.

$$\mu \approx \frac{\rho Z^4}{AE^3} \quad (\text{eqn. 2.18})$$

The absorption coefficient gives the probability that x-rays will be absorbed according to Beer's Law (equation 2.17). Thus, the energy dependence of the absorption coefficient,  $\mu(E)$ , in a transmission geometry can be calculated by equation 2.19, where  $I_t$  and  $I_0$  are the x-ray intensities of the transmitted and incident beams, respectively, and  $t$  is the sample thickness.

$$I_t = I_0 e^{-\mu t} \quad (\text{eqn. 2.19})$$

$$\mu(E) = \ln\left(\frac{I_0}{I_t}\right) \quad (\text{eqn. 2.20})$$

Figure 2.8 provides an example of a XAFS spectrum. XAFS is commonly divided into two regions: (1) the 'near edge' region (XANES), which extends to  $\sim 50$  eV above the absorption edge; and (2) the 'extended' region (EXAFS), that displays oscillations in the absorption coefficient extending from  $\sim 50$  eV above the absorption edge.<sup>25</sup> The absorption edge is defined as the energy at which there is a sharp rise (discontinuity) in the (linear) absorption coefficient of x-rays by an element, which occurs when the energy of photon corresponds to the energy of a shell of the atom.<sup>26</sup>

Peaks present in the near-edge region of the spectrum are often indicative of a non-centrosymmetric environment. Strong pre-edge peaks are a result of orbital overlap between empty  $d$ -electron orbitals with  $p$ -states that photo-electrons must fill. Metal  $3d$  electrons do not normally participate in the absorption process, thus coordination environments without significant hybridization between oxygen  $2p$  and metal  $3d$  levels will not cause a peak to be present. Consequently, the  $pd$  hybridization of ions with unfilled  $d$ -electron bands will be drastically impacted by the coordination environment. This means stronger hybridization and an intense peak

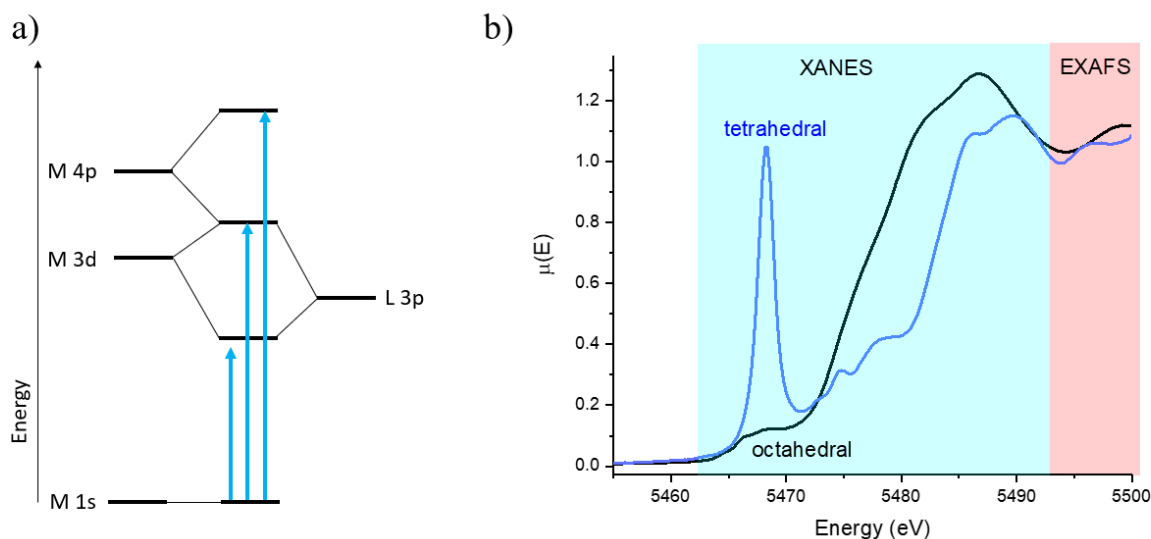


Figure 2.8 (a) Illustration of potential excitations present during XANES spectroscopy experiments. (b) XAFS spectrum of the vanadium edge of  $V_2O_3$  (blue) and  $ScVO_4$  (red).

for non-centrosymmetric tetrahedral coordination, and weaker hybridization and an absence or weak intensity peak for octahedral coordination.

XANES spectra provide fingerprints of the oxidation states and coordination environment. XANES can use linear combinations of spectra obtained from standards, where the coordination environments are well known, to provide a semi-quantitative analysis of the coordination environments.

XAS experiments use x-rays which are produced from a synchrotron source. Synchrotron x-rays are produced by accelerating electrons close to the speed of light and ejecting those into a large storage ring, typically hundreds of meters in diameter.<sup>12</sup> The electrons then travel in a curved path causing a change of momentum; consequently, radiation is produced tangentially to the curve. The advantages of synchrotron radiation include very high intensity, and a broad continuous spectral range (allowing for selection of nearly any wavelength).<sup>27</sup> A continuous spectral range is necessary for XAS as experiments require scanning through a region of specific energies.

## **2.2 Methods**

### **2.2.1 Synthesis**

*High temperature synthesis.* Conventional solid state synthesis was used to prepare the powder samples in this thesis. Stoichiometric amounts of reagents were ground using an agate mortar and pestle in an acetone slurry. Powders were then pressed into pellets, then placed in alumina silicate boats for heating. The Carbolite© tube furnace was used during high temperature reactions in this thesis. The tube furnace can be used to complete reactions in various atmospheres such as oxidizing, reducing and vacuum conditions. Reducing or oxidizing conditions can be employed by flowing either H<sub>2</sub> or O<sub>2</sub> gas through a flow tube. Vacuum atmosphere was achieved either by static vacuum set-up or by sealing samples in evacuated quartz tubes. Schematics of the reaction set-ups are shown in figure 2.9.

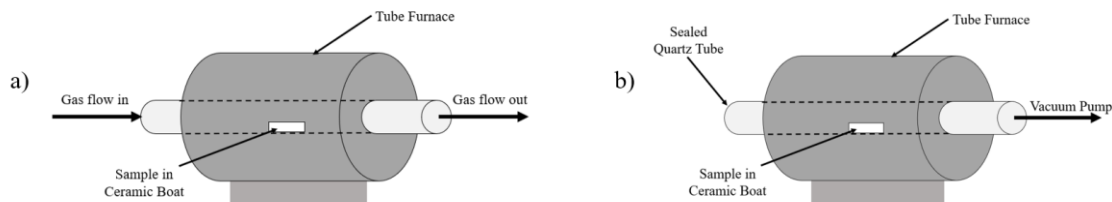


Figure 2.9 (a) Schematic of tube furnace set-up for high temperature synthesis, where gas flow can include either H<sub>2</sub> or O<sub>2</sub> gas. (b) Schematic of tube furnace with quartz tube attached to vacuum pump.

### Zircon structure

**ScVO<sub>4</sub>.** Bulk polycrystalline samples of ScVO<sub>4</sub> (light yellow powder) were prepared. Ammonium vanadate (Cerac, 99.9%) and Sc<sub>2</sub>O<sub>3</sub> were reacted at 1100°C in air for 8 h to prepare ScVO<sub>4</sub> (yellow powder) via reaction 2.1.



**LuCrO<sub>4</sub>.** A 1 g sample of LuCrO<sub>4</sub> (dark green powder) zircon phase was prepared via co-precipitation. The procedure was adapted from Jimenez et al.<sup>28</sup> Lu<sub>2</sub>O<sub>3</sub> (Alfa Aesar, 99.99%) and Cr(NO<sub>3</sub>)<sub>3</sub>·9H<sub>2</sub>O (Alfa Aesar, 98.5%) were dissolved in excess nitric acid. The solution was heated up to 90 °C with continuous stirring. The precipitated intermediate was a yellow powder. The intermediate was then heated according to the following scheme: 160 °C (30 min), 200 °C (30 min) and 580 °C (1 h). Heating was completed under O<sub>2</sub> flow to stabilize Cr<sup>5+</sup> oxidation state.

### Vanadium Oxides

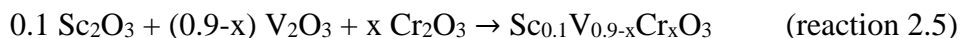
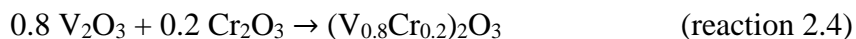
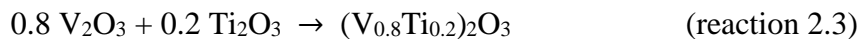
Bulk phase pure V<sub>2</sub>O<sub>3</sub> (black powder) was prepared via reduction of V<sub>2</sub>O<sub>5</sub> at 1100°C under 100% H<sub>2</sub> flow for 12 h. Bulk phase pure VO<sub>2</sub> (black powder) was prepared by reacting V<sub>2</sub>O<sub>3</sub> and V<sub>2</sub>O<sub>5</sub> at 1100°C for 12 hours under static vacuum following reaction 2.2.



### Corundum Phases

The following reactions (2.3-2.5) were completed via conventional solid state synthesis. Sample size for each reaction was approximately 0.5 g. Stoichiometric amounts of powdered reagents were ground using an agate mortar and pestle in an acetone slurry. The starting material

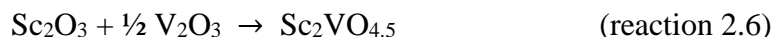
was then heated at 1500°C in a tube furnace under reducing conditions (5% H<sub>2</sub> in N<sub>2</sub>) for 48 h. Sc<sub>2</sub>O<sub>3</sub> (SynQuest Laboratories, 99.95%), Ti<sub>2</sub>O<sub>3</sub> (Alfa Aesar, 99.8%), Cr<sub>2</sub>O<sub>3</sub> (Fisher Scientific) and V<sub>2</sub>O<sub>3</sub> were used as starting materials.



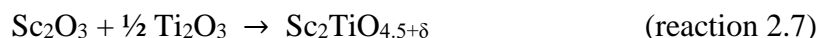
### Bixbyite Phases

**Sc<sub>2</sub>V<sub>1-x</sub>Ti<sub>x</sub>O<sub>4.5+δ</sub>**. The following phases were prepared via high temperature reactions under reducing conditions. Note the term δ is added to the oxygen stoichiometry in Ti containing phases to account for uncertainty of Ti oxidation state. This will be further discussed in chapter 3.

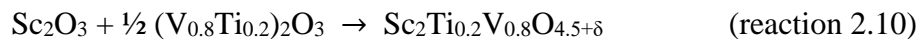
A 1 g sample of Sc<sub>2</sub>VO<sub>4.5</sub> (x = 0) was prepared by reacting Sc<sub>2</sub>O<sub>3</sub> (SynQuest Laboratories, 99.95%) and V<sub>2</sub>O<sub>3</sub> according to reaction 2.6. The reaction was conducted at 1500°C in a tube furnace under reducing conditions (5% H<sub>2</sub> in N<sub>2</sub>). The sample was heated in two 48 h intervals with intermittent grindings.



For Sc<sub>2</sub>TiO<sub>4.5+δ</sub> (x = 1.0), three reactions were performed to obtain the bixbyite phase (s.g. *Ia* $\bar{3}$ ). For reaction 2.8, a 1 g sample was prepared, whereas reactions 2.7 and 2.9 had a sample size of 0.25 g. In each reaction, stoichiometric amounts of powder reagents were ground using an agate mortar and pestle in an acetone slurry then heated at 1500°C in a tube furnace for a total of 96 hours with one intermittent grinding. Sc<sub>2</sub>O<sub>3</sub> (SynQuest Laboratories, 99.95%), Ti<sub>2</sub>O<sub>3</sub> (Alfa Aesar, 99.8%), Ti metal (Alfa Aesar, 99.99%) and TiO<sub>2</sub> (Alfa Aesar, 99.995%) were used as starting materials.



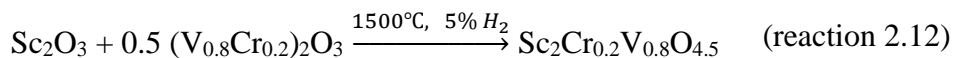
A 0.25 g sample of  $\text{Sc}_2\text{Ti}_{0.2}\text{V}_{0.8}\text{O}_{4.5+\delta}$  ( $x = 0.2$ ) was prepared by reacting  $\text{Sc}_2\text{O}_3$  with corundum- $(\text{V}_{0.8}\text{Ti}_{0.2})_2\text{O}_3$  (prepared via reaction 2.3) at  $1500^\circ\text{C}$  under reducing conditions (5%  $\text{H}_2$  in  $\text{N}_2$ ) for 48 h according to reaction 2.10.



For  $\text{Sc}_2\text{Ti}_{0.8}\text{V}_{0.2}\text{O}_{4.5+\delta}$  ( $x = 0.8$ ), bixbyite- $\text{Sc}_2\text{VO}_{4.5}$  and bixbyite- $\text{Sc}_2\text{TiO}_{4.5}$  were used as starting materials. A 0.25 g sample was prepared. Stoichiometric amounts of starting materials according to reaction 2.11 were ground using an agate mortar and pestle. The starting materials were then pelletized and placed onto a ceramic boat that was then heated for 48 h in reducing atmosphere (5%  $\text{H}_2$  in  $\text{N}_2$ ) at  $1500^\circ\text{C}$ .



**$\text{Sc}_2\text{Cr}_{0.2}\text{V}_{0.8}\text{O}_{4.5}$ .** A 0.2 g sample of  $\text{Sc}_2\text{Cr}_{0.2}\text{V}_{0.8}\text{O}_{4.5}$  was prepared by reacting corundum- $(\text{V}_{0.8}\text{Cr}_{0.2})_2\text{O}_3$  (prepared via reaction 2.4) and  $\text{Sc}_2\text{O}_3$  (SynQuest Laboratories, 99.95%). The reaction was heated at  $1500^\circ\text{C}$  in 5%  $\text{H}_2$  in  $\text{N}_2$  atmosphere for 48 h.

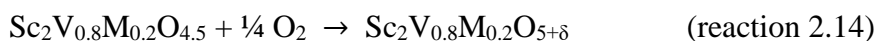


### Fluorite Phases

**$\text{Sc}_2\text{TiO}_5$ .** A 1:1 ratio of  $\text{TiO}_2$  (Alfa Aesar, 99.995%) and  $\text{Sc}_2\text{O}_3$  (SynQuest Laboratories, 99.95%) were thoroughly mixed and heated at  $1500^\circ\text{C}$  in air for 30 h, according to reaction 2.13.



**$\text{Sc}_2\text{M}_{0.2}\text{V}_{0.8}\text{O}_{5+\delta}$  ( $M = \text{Ti and Cr}$ ).** Bixbyite precursors  $\text{Sc}_2\text{Ti}_{0.2}\text{V}_{0.8}\text{O}_{4.5+\delta}$  and  $\text{Sc}_2\text{Cr}_{0.2}\text{V}_{0.8}\text{O}_{4.5}$  were heated at  $400^\circ\text{C}$  in air for 8 h to obtain fluorite structures  $\text{Sc}_2\text{Ti}_{0.2}\text{V}_{0.8}\text{O}_{5+\delta}$  and  $\text{Sc}_2\text{Cr}_{0.2}\text{V}_{0.8}\text{O}_{5+\delta}$ , respectively.



### Tetragonal $I\bar{4}$

**$Sc_2Ti_xV_{1-x}O_{5+\delta}$  ( $x = 0.8$  and  $0.6$ ).** Bulk polycrystalline samples (2 g) of the tetragonal- $Sc_2VO_5$  phase were prepared via conventional solid state methods, according to reaction 2.15. Stoichiometric amounts of starting materials were ground using an agate mortar and pestle; followed by ball milling for 48 h. The mixed precursor underwent multiple heatings in air (800°C 48h, 1000°C 30h, 1200°C 30h), with intermittent grindings.  $Sc_2Ti_{0.6}V_{0.4}O_{5+\delta}$  ( $x = 0.6$ ) required two additional heatings at 1300°C (12h) and 1350°C (12h).



**$Sc_2V_{0.8}M_{0.2}O_{5+\delta}$  ( $M = Ti$  and  $Cr$ ).** A direct synthesis approach was used to prepare tetragonal- $Sc_2V_{0.8}M_{0.2}O_{5+\delta}$  ( $M = Cr$  and  $Ti$ ) phases. Bulk polycrystalline (2 g) samples of each reaction were prepared. Stoichiometric amounts of starting materials, according to reaction 2.16, were ground as an acetone slurry using an agate mortar and pestle. The pelletized sample was loaded onto a ceramic boat and was heated for 12 hours at 1100 °C in either an evacuated quartz tube ( $M = Ti$ ) or under static vacuum ( $M = Cr$ ).



Tetragonal-  $Sc_2V_{0.8}M_{0.2}O_{5+\delta}$  ( $M = Cr$  and  $Ti$ ) phases were also prepared via reconstructive oxidation. Reconstructive oxidation was completed by heating the bixbyite-precursors  $Sc_2Ti_{0.2}V_{0.8}O_{4.5+\delta}$  and  $Sc_2Cr_{0.2}V_{0.8}O_{4.5}$  in a pre-heated furnace at 1100°C in traces of  $O_2$  ( $N_2$  with approximately 5 ppm  $O_2$ ).



A schematic of the reaction set-up is shown in figure 2.10. Heatings were conducted in intervals ranging from 15-30 minutes, with intermittent grindings. The tube furnace was preheated to avoid oxidation. An x-ray diffractogram was collected at room temperature after each heating to track the progress of the oxidation.

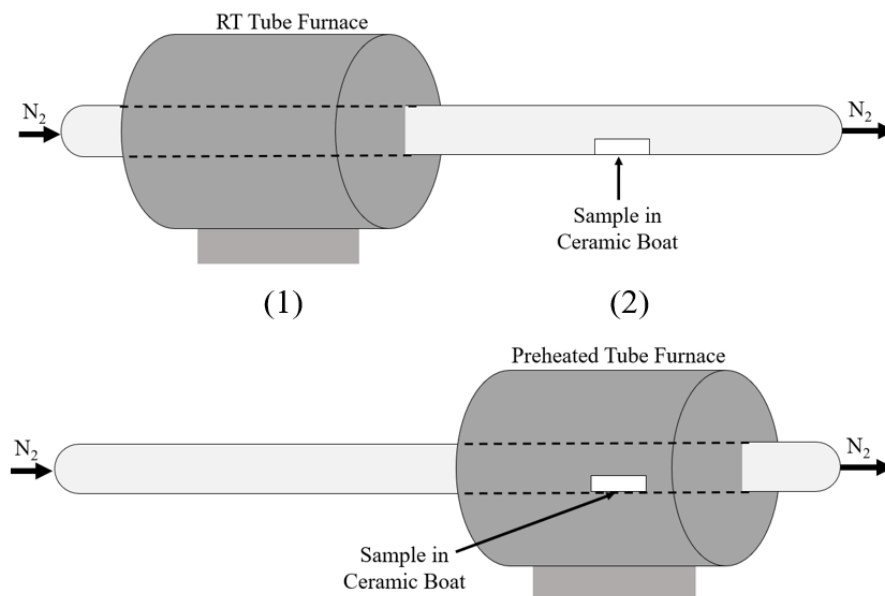


Figure 2.10 Schematic of reconstructive oxidation set-up where the tube furnace starts a room temperature (RT) then is ramped to the target temperature in position 1. Once the tube furnace has reached the target temperature it is moved over the sample to position 2.

## 2.2.2 Powder X-ray Diffraction

Powder x-ray diffraction data were collected on a Huber G670 Guinier Camera using  $Cu\ K\alpha_1$  radiation (Ge-monochromator,  $\lambda(Cu-K\alpha_1) = 1.540560\ \text{\AA}$ ). Samples were mounted as a thin layer on a Mylar polyester film using acetone slurries. Data were collected with a 5 minute exposure time and collected from a  $2\theta$  range of  $15^\circ$  to  $100^\circ$  with a step size of  $0.005^\circ$ . Rietveld refinements were conducted using TOPAS.<sup>20</sup>

## 2.2.3 XANES

The V, Ti and Cr K edge XANES were collected on the 9-BM beamline located at the Advanced Photon Source at Argonne National Laboratory, Illinois. Samples were prepared as powders and pressed to 7 mm diameter pellets with appropriate amount of polyethylene glycol. Samples were then mounted with Kapton tape. Spectra were collected in transmission mode. All XANES spectra were analyzed by using Athena<sup>29</sup> software program. Spectra were calibrated with V ( $E_0 = 5465\ \text{eV}$ ), Ti ( $E_0 = 4966\ \text{eV}$ ) and Cr ( $E_0 = 5989\ \text{eV}$ ) foils.

### 2.2.4 Magnetic Measurements

Direct current (DC) magnetic susceptibility data were collected using Quantum Design Physical Property Measurement System (PPMS) with a vibrating sample magnetometer option. Approximately 20 mg of powdered sample was packed into a gelatin capsule, then loaded into the instrument. The sample was cooled to 2 K in zero applied magnetic field and measured from 2 to 350 K with a 0.1 T applied magnetic field. Zero-field cooled measurements were collected for  $\text{Sc}_2\text{Ti}_{0.2}\text{V}_{0.8}\text{O}_{5+\delta}$  (chapter 3) and  $\text{Sc}_2\text{V}_{0.8}\text{Cr}_{0.2}\text{O}_{5+\delta}$  (chapter 4) prepared via reaction 2.17. The diamagnetic contribution was subtracted from the data, where the diamagnetic contribution was calculated using published values.<sup>30</sup>

### 2.2.5 Neutron Diffraction

A room temperature neutron powder diffraction experiment was carried out for tetragonal- $\text{Sc}_2\text{V}_{0.8}\text{Cr}_{0.2}\text{O}_{5+\delta}$  prepared via direct synthetic method (reaction 2.17). Data were collected using POWGEN diffractometer,<sup>16,31</sup> at the Spallation Neutron Source at Oak Ridge National Laboratory (ORNL) in Oak Ridge, Tennessee. A 0.8293 g powder sample was packed into a 6 mm cylindrical vanadium can. Central wavelength of 1.500 Å was used to collect data in a d-spacing range from 0.485 to 13.00 Å. Data were collected for approximately 1 hour. Silicon was used as a calibration standard for instrument parameters.

## Chapter 3: Titanium and the Scandium Vanadates

---

This chapter focuses on the introduction of titanium into the  $\text{Sc}_2\text{VO}_{5+\delta}$  family of phases. Section 3.1 explores the synthesis and reactivity of disordered  $\text{Sc}_2\text{Ti}_x\text{V}_{1-x}\text{O}_{5+\delta}$  phases for  $x = 1.0, 0.8,$  and  $0.2$ . This section is necessary to understand the synthetic pathways to obtain the cation ordered tetragonal  $\bar{I}4$  structure, and potential competing phases during synthesis. Section 3.2 investigates the tetragonal phase with nominal compositions  $\text{Sc}_2\text{Ti}_x\text{V}_{1-x}\text{O}_{5+\delta}$  for  $x = 0.8, 0.6,$  and  $0.2$ . The overall objective of this work is to substitute  $\text{Ti}^{4+}$  into the octahedral  $\text{V}1^{8g}$  site of the tetragonal  $\bar{I}4$  phase to demonstrate that the octahedral  $\text{V}1^{8g}$  and tetrahedral  $\text{V}2^{2c}$  sites within this structure are individually controllable.

### 3.1 Disordered Structures:

#### 3.1.1 Background.

This section investigates the cation-disordered phases for the  $\text{Sc}_2\text{Ti}_x\text{V}_{1-x}\text{O}_{5+\delta}$  series. The sesquioxides  $\text{V}_2\text{O}_3$  and  $\text{Ti}_2\text{O}_3$  both crystallize in the corundum structure (s.g.  $R\bar{3}c$ ). The ionic radii of  $\text{Ti}^{3+}$  and  $\text{V}^{3+}$  are similar ( $\text{Ti}^{3+}$   $r(\text{VI}) = 0.67 \text{ \AA}$ ;  $\text{V}^{3+}$   $r(\text{VI}) = 0.64 \text{ \AA}$ )<sup>5</sup> and form the solid solution  $(\text{V}_{1-x}\text{Ti}_x)_2\text{O}_3$  that crystallizes in the corundum structure.<sup>32,33</sup> In contrast,  $\text{Sc}_2\text{O}_3$  crystallizes in a bixbyite phase (s.g.  $Ia\bar{3}$ ). The  $\text{Ti}_2\text{O}_3$  phase can be doped with  $\text{Sc}_2\text{O}_3$  ( $(\text{Ti}_{1-x}\text{Sc}_x)_2\text{O}_3$ ,  $x < 0.0413$ ) and maintain the corundum structure.<sup>34</sup> Increasing the concentration of  $\text{Sc}^{3+}$  within this system will favour crystallization in the bixbyite phase as demonstrated by  $\text{ScTiO}_3$  (or  $(\text{Sc}_x\text{Ti}_{1-x})_2\text{O}_3$  where  $x = 0.5$ ).<sup>7,35</sup> The binary phase diagram between  $\text{Ti}_2\text{O}_3$  and  $\text{Sc}_2\text{O}_3$  has not been thoroughly investigated; however a proposed miscibility gap would likely lie between  $\text{Ti}_2\text{O}_3$  and  $\text{Sc}_2\text{O}_3$ , similar to the  $\text{V}_2\text{O}_3$ - $\text{Sc}_2\text{O}_3$  system.<sup>36</sup> For  $\text{Ti}^{4+}$ , four scandium titanate phases have been reported:  $\text{Sc}_2\text{Ti}_2\text{O}_7$  pyrochlore;<sup>37</sup> cubic fluorite<sup>7</sup> and rhombohedral fluorite<sup>38,39</sup> phases of composition  $\text{Sc}_4\text{Ti}_3\text{O}_{12}$ ; and  $\text{Sc}_2\text{TiO}_5$  pseudobrookite.<sup>40,41</sup>

The rhombohedral fluorite  $\text{Sc}_4\text{Ti}_3\text{O}_{12}$  (s.g.  $R\bar{3}$ ) is a superstructure with cation disorder on one of the 2 cation sites as illustrated in figure 3.1. The  $3a$  site  $(0, 0, 0)$  only accommodates Ti, whereas the  $18f$  site  $(x, y, z)$  is occupied with disordered Sc and Ti. The metal  $3a$  site has an

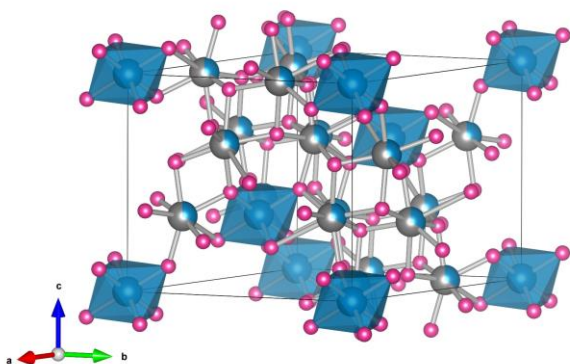


Figure 3.1 Illustration of the rhombohedral fluorite  $\text{Sc}_4\text{Ti}_3\text{O}_{12}$  structure (s.g.  $R\bar{3}$ ). Blue =  $\text{Ti}^{4+}$ , grey =  $\text{Sc}^{3+}$  and pink =  $\text{O}^{2-}$ .

and Ti occupy two metal sites,  $8f$  and  $4c$ , which have distorted octahedral coordination environments. The distorted octahedra are edge-sharing and form trimeric units along the  $c$ -axis, with the  $4c$  site located between two  $8f$  sites. The trioctahedral chains are corner sharing along the  $c$ -axis and edge sharing along the  $b$ -axis. The ordered-anion lattice consists of three distinct crystallographic positions.

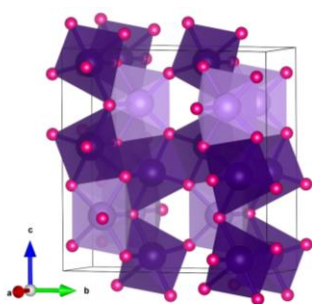


Figure 3.2 Illustration of the pseudobrookite structure (s.g.  $Cmcm$ ). Dark purple =  $8f$  site, light purple =  $4c$  site, pink = anion.

octahedral geometry and the metal  $18f$  site has a 7-fold coordination environment. There are two sites on the anion lattice:  $\text{O}1^{18f}$  and  $\text{O}2^{18f}$ .

The  $\text{Sc}_2\text{TiO}_5$  composition is of particular interest as it is a member of the  $\text{Sc}_2\text{BO}_5$  family. The orthorhombic pseudobrookite structure crystallizes in space group  $Cmcm$  (#63) and is illustrated in figure 3.2. Disordered Sc

In 1971, Ito first reported the single crystal growth of pseudobrookite- $\text{Sc}_2\text{TiO}_5$ .<sup>40</sup> A detailed structural study was later reported, and once again  $\text{Sc}_2\text{TiO}_5$  was obtained through single crystal growth using the flux method.<sup>41</sup> Lyashenko in 2004 also reported the  $\text{Sc}_2\text{TiO}_5$  as pseudobrookite; however, this phase was obtained from coprecipitation of a 1:1 ratio of  $\text{Sc}^{3+}$  and  $\text{Ti}^{4+}$  hydroxides followed by annealing at temperatures between 1100-1300°C.<sup>42</sup> The synthesis of the rhombohedral phase also required a co-precipitation synthesis method to achieve a single phase. In contrast, the previously reported solid state synthesis resulted in impure pseudobrookite with rutile ( $\text{TiO}_2$ ) and fluorite competing phases.<sup>38</sup>

This section investigates the  $\text{Sc}_2\text{TiO}_{5+\delta}$  system using conventional solid state techniques as a synthetic route. The  $\text{Ti}^{4+}$  oxidation state was first considered and the effect of annealing temperature on phase formation was investigated between 1:1  $\text{Sc}_2\text{O}_3$  to  $\text{TiO}_2$  composition. This work also investigated cation-disordered  $\text{Sc}_2\text{Ti}_x\text{V}_{1-x}\text{O}_{4.5+\delta}$  bixbyite phases for  $x = 0.2, 0.8,$  and  $1.0$

which will lead to the conversion of the cation-ordered tetragonal  $I\bar{4}$  phases  $\text{Sc}_2\text{Ti}_x\text{V}_{1-x}\text{O}_{5+\delta}$  ( $x = 0.2, 0.6$  and  $0.8$ ) discussed in section 3.2.

### 3.1.2 Results and Discussion.

**Scandium Titanates.** Five samples of a 1:1 ratio of  $\text{Sc}_2\text{O}_3$  and  $\text{TiO}_2$  powders were mixed and heated in air at temperatures between  $1100^\circ\text{C}$  and  $1500^\circ\text{C}$ , according to reaction 2.13. Table 3.1 reports the phase composition of each sample after annealing, the x-ray diffraction data are included in the appendix (figure A.1). The pseudobrookite phase was the major phase for synthesis temperatures between  $1100^\circ\text{C}$  and  $1300^\circ\text{C}$ . In this temperature range, pseudobrookite- $\text{Sc}_2\text{TiO}_5$  coexists with either rhombohedral or fluorite

Table 3.1 Compositions of 1:1  $\text{Sc}_2\text{O}_3$  and  $\text{TiO}_2$  phases after annealing at temperatures between  $1100^\circ\text{C}$  and  $1500^\circ\text{C}$ .

Synthesis Temperature ( $^\circ\text{C}$ )	Composition* <sup>†</sup>
1100	<b>P</b> + R + B
1200	<b>P</b> + R + B
1250	<b>P</b> + B + F
1300	<b>P</b> + B + F
1500	<b>F</b>

\*Bolded font represents major phase  
<sup>†</sup>P = pseudobrookite, F = fluorite, R = rhombohedral, B = bixbyite

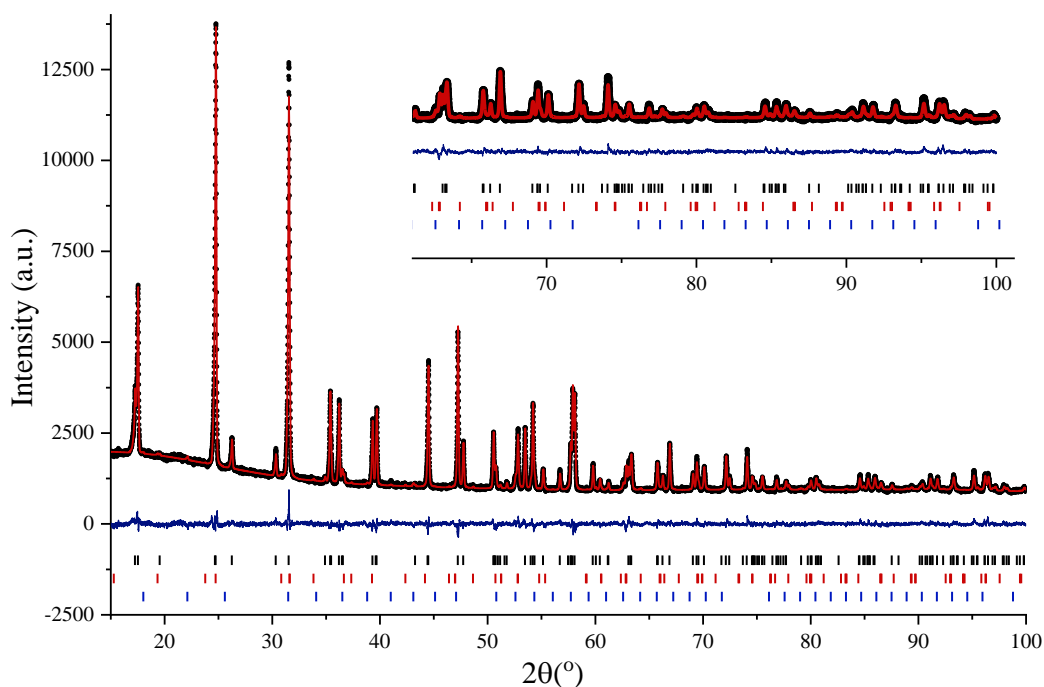


Figure 3.3 The Rietveld plot of powder x-ray diffraction data for the product of heating 1:1  $\text{Sc}_2\text{O}_3$  and  $\text{TiO}_2$  at  $1200^\circ\text{C}$  in air. Refined composition of  $\text{Sc}_2\text{O}_3 + \text{TiO}_2$  at  $1200^\circ\text{C}$  was 87.2(2)% pseudobrookite (s.g.  $Cmcm$ ) with rhombohedral phase (s.g.  $R\bar{3}$ ), and bixbyite phase (s.g.  $Ia\bar{3}$ ) impurities. The black closed circles = measured data, red line = fit, blue line = difference, and black, red and blue ticks = Bragg peaks corresponding to pseudobrookite, rhombohedral and bixbyite phases, respectively.

phases, and the bixbyite phase ( $\text{Sc}_2\text{O}_3$ ). The rhombohedral (cation-disordered, anion-ordered) impurity is favoured at lower temperatures and the fluorite (cation-disordered, anion-disordered) impurity is favoured at higher temperatures. The pseudobrookite phase was most favourable at 1200°C; yet the product at 1200°C contained bixbyite and rhombohedral impurities. This suggests that conventional solid state synthesis may be unable to stabilize the  $\text{Sc}_2\text{TiO}_5$ -pseudobrookite phase, instead flux-growth or co-precipitation synthesis would be more appropriate methods to use, as demonstrated by previous literature. The Rietveld plot of the refined structure for the product at 1200°C is shown in figure 3.3 and crystallographic data for this phase are reported in table 3.2.

Table 3.2 Refined structural parameters for pseudobrookite- $\text{Sc}_2\text{TiO}_5$ . The structure was refined in space group  $Cmcm$ ,  $a = 3.84668(2)$  Å,  $b = 10.11963(6)$  Å,  $c = 10.27596(6)$  Å, and  $V = 400.01(4)$  Å<sup>3</sup>.  $R_{\text{wp}}/\chi^2 = 2.99/1.09$ .

Atom	Site	x	y	z	SOF
Sc/Ti	8f	0	0.1355(1)	0.5616(1)	1.0
Sc/Ti	4c	0	0.1923(1)	¼	1.0
O	8f	0	0.0451(3)	0.1151(3)	1.0
O	4c	0	0.7633(4)	¼	1.0
O	8f	0	0.3068(3)	0.0719(3)	1.0

Note: The sample contains 87.2(2)% pseudobrookite phase with bixbyite and rhombohedral-fluorite impurities.

A single phase fluorite was found when the synthesis temperature increased to 1500°C resulting in the novel fluorite phase:  $\text{Sc}_2\text{TiO}_5$ . The Rietveld plot of the refined structure for fluorite  $\text{Sc}_2\text{TiO}_5$  (s.g.  $Fm\bar{3}m$ ) is shown in figure 3.4 and the refined crystallographic parameters are included in table 3.3.  $\text{Sc}_2\text{TiO}_5$  can be described as a defect fluorite structure as the cation oxidation states constrain the maximum amount of oxygen available within the structure.  $\text{Sc}^{3+}$  and  $\text{Ti}^{4+}$  cations are in their fully oxidized state thus the oxygen stoichiometry is limited to 5 atoms per formula, whereas an oxide vacancy free fluorite structure would have 6 atoms per formula unit. The oxygen site (8c) was refined to be 86.5(5)% occupied which corresponds to 5.19(3) oxygen

Table 3.3 Refined structural parameters for fluorite- $\text{Sc}_2\text{TiO}_5$ . Space group:  $Fm\bar{3}m$ ,  $a = 4.9034(3)$  Å,  $V = 177.893$  Å<sup>3</sup>.  $R_{\text{wp}}/\chi^2 = 2.47 / 0.86$ .

Atom	Site	x	y	z	SOF	B <sub>iso</sub> (Å <sup>2</sup> )
Sc	4a	0	0	0	2/3	2.1(2)
Ti	4a	0	0	0	1/3	2.1(2)
O	8c	¼	¼	¼	0.865(5)	6.5(1)

anions per formula unit. It is noted that this result is not physical as the maximum oxygen stoichiometry is 5 oxygen anions since  $\text{Sc}^{3+}$  and  $\text{Ti}^{4+}$  cannot be oxidized further, neutron diffraction data would be required for precise quantification of oxide stoichiometry. The large thermal parameter is attributed to disorder on the anionic lattice, and agrees with the thermal parameter reported for  $\text{ScTiO}_{3.5}$ .<sup>7</sup>

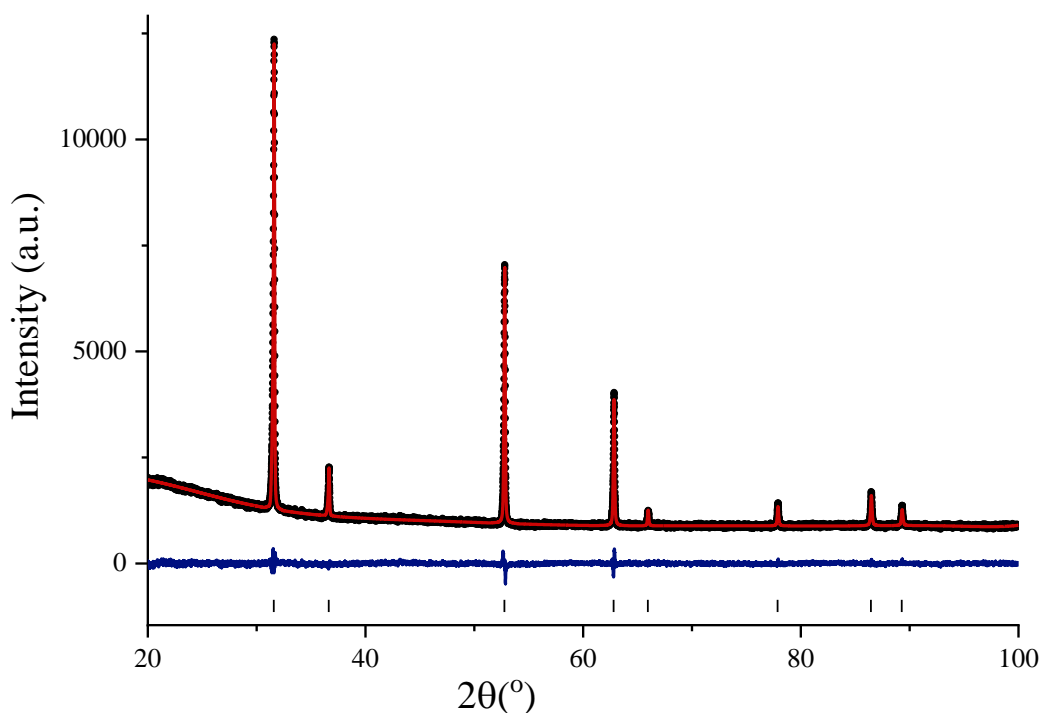


Figure 3.4 The Rietveld plot of x-ray diffraction data obtained from  $\text{Sc}_2\text{TiO}_5$  fluorite phase (s.g.  $Fm\bar{3}m$ ) where black closed circles = measured data, red line = fit, blue line = difference and black ticks = Bragg peaks corresponding to fluorite phase.

The structure of the  $\text{Sc}_2\text{TiO}_5$  composition depends on annealing temperature, and a phase transition between pseudobrookite (s.g.  $Cmcm$ ) and fluorite (s.g.  $Fm\bar{3}m$ ) occurs upon dwelling at low and high temperatures, respectively. To demonstrate this, one sample of a 1:1 ratio of  $\text{Sc}_2\text{O}_3$  to  $\text{TiO}_2$  was mixed and then was heated at each temperature  $1200^\circ\text{C}$  (24 h),  $1500^\circ\text{C}$  (24 h),  $1300^\circ\text{C}$  (24 h), and  $1100^\circ\text{C}$  (48 h). The sample was ground intermittently, and x-ray diffraction data were collected at room temperature between each heating. The diffractograms of each heating are shown in figure 3.5. At  $1200^\circ\text{C}$ , pseudobrookite (86.8(1)%), rhombohedral-fluorite (8.5(1)%), and bixbyite (4.7(1)%) phases are present, then heating to  $1500^\circ\text{C}$  the cubic-fluorite phase was the only phase. Lowering the temperature to  $1300^\circ\text{C}$ , resulted in formation of pseudobrookite (48.1(4)%), fluorite (40.3(3)%), and bixbyite (11.6(3)%) phases. Then after dwelling at  $1100^\circ\text{C}$ ,

pseudobrookite (73.6(1)%), cubic-fluorite (14.6(1)%), and bixbyite (11.8(1)%) phases were present. This demonstrates temperature control can cycle between cubic-fluorite and pseudobrookite phases. The pseudobrookite structure is dominant at low temperatures and co-exists with competing phases. Whereas the fluorite structure is the single phase found at 1500°C.

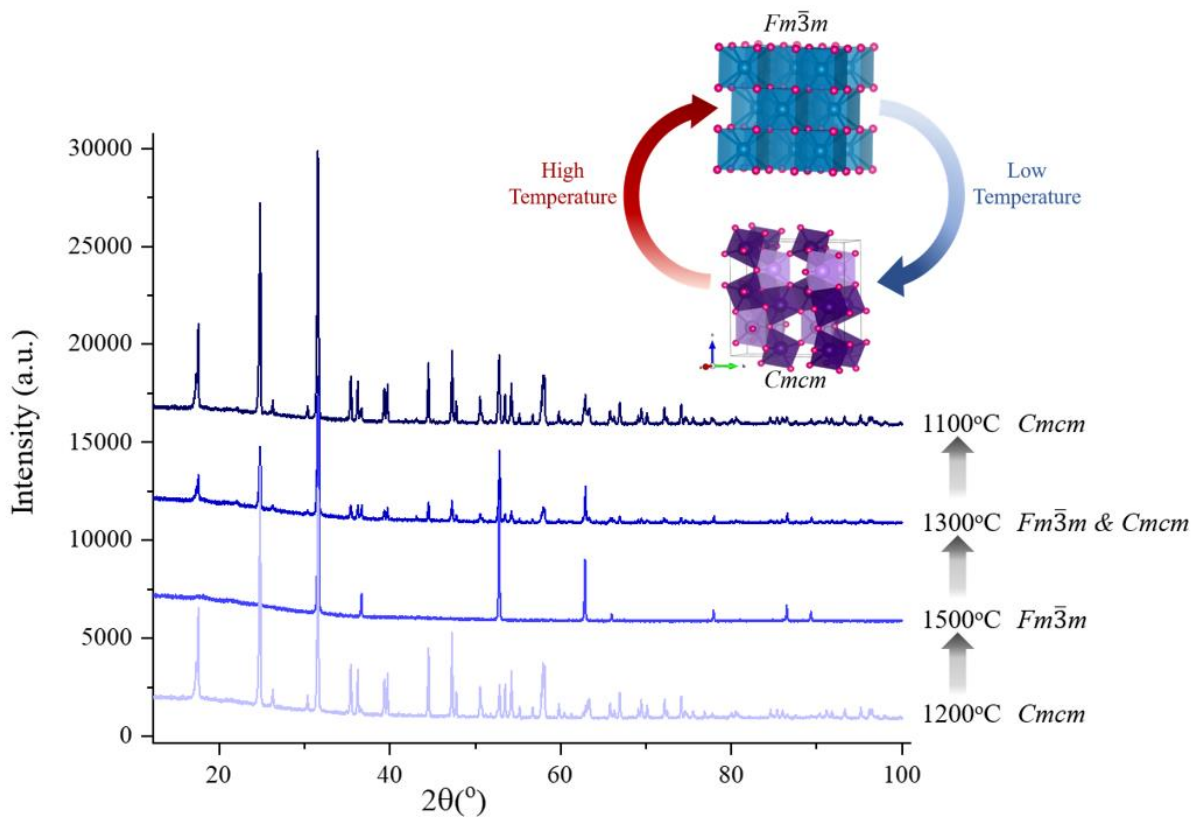


Figure 3.5 Room temperature ex-situ x-ray diffraction data for temperature dependent  $\text{Sc}_2\text{TiO}_5$  phase evolution.  $\text{Sc}_2\text{TiO}_5$  was sequentially heated at 1200°C (24 h), 1500°C (24 h), 1300°C (24 h), and 1100°C (48 h).

The preparation of the  $\text{Sc}_2\text{TiO}_{4.5}$  bixbyite phase was attempted using  $\text{Ti}_2\text{O}_3$  as a starting material (reaction 2.7). The Rietveld plot of the product of reaction 2.7 is shown in figure 3.6, and refined structural parameters are reported in table 3.4. The superstructure peaks of a characteristic bixbyite phase are less prominent than expected. Using the x-ray diffraction data, the structure was refined in space group  $Ia\bar{3}$ ; however, it was found that an additional oxygen position ( $16c$ ) was partially occupied. The addition of oxygen in the  $16c$  site allowed the intensity of the superstructure peaks to be accurately modelled. The oxygen stoichiometry was found to be 4.63(1) suggesting a

mixture of  $\text{Ti}^{4+/3+}$  within the structure and that the reaction conditions were not effective in maintaining the  $\text{Ti}^{3+}$  oxidation state.

Table 3.4 Refined structural parameters for bixbyite- $\text{Sc}_2\text{TiO}_{4.5+\delta}$ . Space group:  $Ia\bar{3}$ ,  $a = 9.78491(8)$ , Å, and  $V = 400.01(4)$  Å<sup>3</sup>.  $\chi^2/R_{\text{wp}} = 0.94/2.72$ .

Atom	Site	x	y	z	SOF
Sc/Ti	8a	0	0	0	1.0
Sc/Ti	24d	0.2545(3)	0	¼	1.0
O	48e	0.1026(6)	0.3573(7)	0.13691(9)	1.0
O	16c	0.1443(7)	0.1443(7)	0.1443(7)	0.47(1)

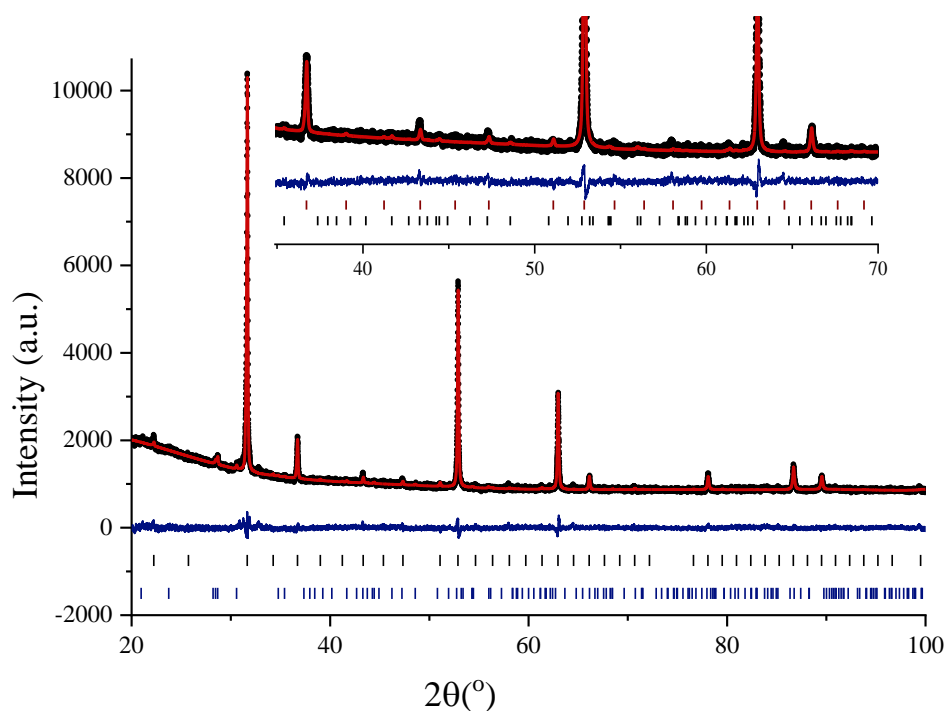


Figure 3.6 The Rietveld plot of x-ray diffraction data obtained from  $\text{Sc}_2\text{TiO}_5$  bixbyite phase (s.g.  $Ia\bar{3}$ ) where black closed circles = measured data, red line = fit, blue line = difference and black ticks = Bragg peaks corresponding to bixbyite phase.

Two additional reactions using: (1)  $\text{Ti}^{4+}/\text{Ti}^0$ ; and (2)  $\text{TiO}_2$  as starting materials (reactions 2.8 and 2.9, respectively) were also investigated. Comparison of x-ray diffraction data, shown in figure A.2, revealed similar intensity of superstructure peaks. This suggests using a mixture of  $\text{Ti}^{4+}/\text{Ti}^0$ , or  $\text{TiO}_2$  as a source of titanium will also yield a mixture of  $\text{Ti}^{4+/3+}$ . Thus, a  $\delta$  term is added to account for the mixed titanium oxidation states and consequently increased oxygen content within the structure. The previously reported  $\text{ScTiO}_3$  bixbyite phase was obtained through synthesis at high temperature in a vacuum setup ( $p < 10^{-4}$  mbar) which stabilized the  $\text{Ti}^{3+}$  oxidation

state.<sup>7</sup> This set-up is a promising route to achieve a bixbyite phase of composition  $\text{Sc}_2\text{TiO}_{4.5}$  with titanium in the +3 oxidation state.

**$\text{Sc}_2\text{Ti}_x\text{V}_{1-x}\text{O}_{4.5+\delta}$  Bixbyite Phases.** The cation-disordered bixbyite phases of composition  $\text{Sc}_2\text{Ti}_x\text{V}_{1-x}\text{O}_{4.5+\delta}$  for  $x = 0.2$  and  $0.8$  were prepared at high temperature under reducing conditions. Bixbyite  $\text{Sc}_2\text{Ti}_{0.2}\text{V}_{0.8}\text{O}_{4.5+\delta}$  ( $x = 0.2$ , s.g.  $Ia\bar{3}$ ) was obtained by reaction of  $(\text{V}_{0.8}\text{Ti}_{0.2})_2\text{O}_3$  and  $\text{Sc}_2\text{O}_3$  (reaction 2.10). Figure 3.7 shows the Rietveld plot of  $\text{Sc}_2\text{V}_{0.8}\text{Ti}_{0.2}\text{O}_{4.5}$  (s.g.  $Ia\bar{3}$ ) and refined structural parameters are reported in table 3.5. The sample contained a 1.2(1)% impurity of  $\text{Sc}_2\text{Si}_2\text{O}_7$  phase attributed to  $\text{Sc}_2\text{O}_3$  reacting with the silicate in the ceramic boat used during synthesis. It is assumed  $\text{Sc}_2\text{Ti}_{0.2}\text{V}_{0.8}\text{O}_{4.5}$  is a cation-disordered bixbyite as there is no difference in charge between  $\text{Sc}^{3+}$ ,  $\text{V}^{3+}$  and  $\text{Ti}^{3+}$ , and cations are of comparable size ( $\text{Sc}^{3+}$   $r(\text{VI}) = 0.745 \text{ \AA}$ ,  $\text{V}^{3+}$   $r(\text{VI}) = 0.64 \text{ \AA}$ ,  $\text{Ti}^{3+} = 0.67 \text{ \AA}$ ).<sup>5</sup>

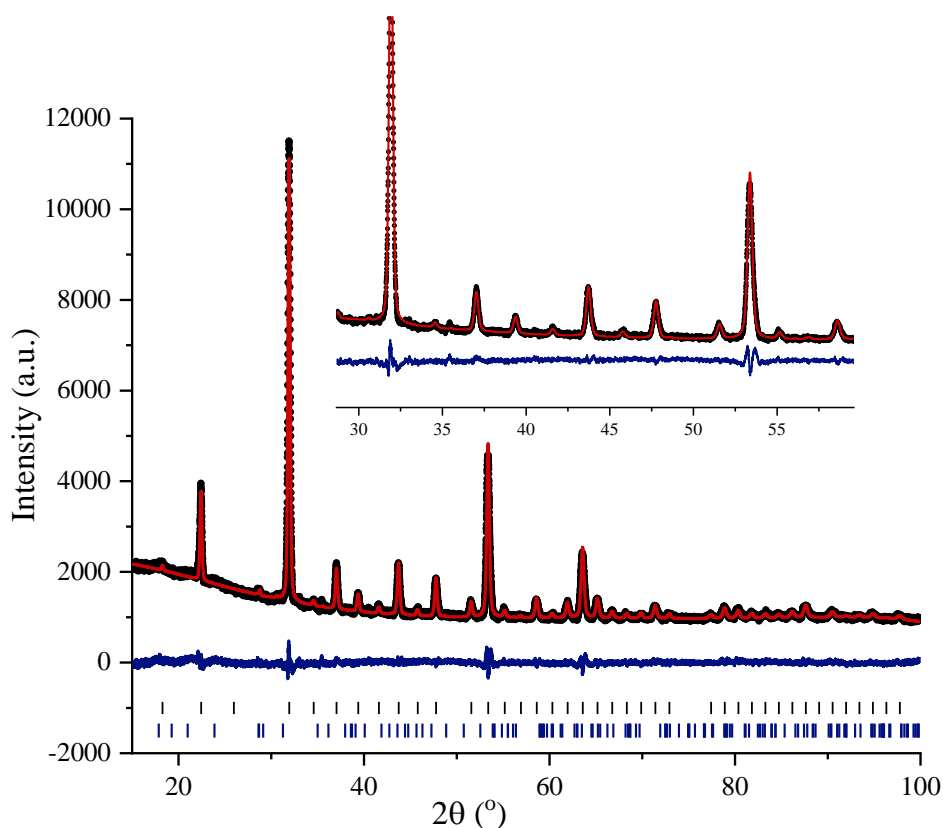


Figure 3.7 The Rietveld plot of x-ray diffraction data of  $\text{Sc}_2\text{Ti}_{0.2}\text{V}_{0.8}\text{O}_{4.5+\delta}$  ( $x = 0.2$ , s.g.  $Ia\bar{3}$ ) obtained from the reaction between  $\text{Sc}_2\text{O}_3 + (\text{V}_{0.8}\text{Ti}_{0.2})_2\text{O}_3$  (reaction 2.10) after heating at  $1500^\circ\text{C}$  in 5%  $\text{H}_2$  for 48 h. Black closed circles = measured data, red line = fit, blue line = difference and black and blue ticks = Bragg peaks corresponding to fluorite and  $\text{Sc}_2\text{Si}_2\text{O}_7$  phases, respectively. The  $\text{Sc}_2\text{Si}_2\text{O}_7$  impurity accounts for 1.2(1)% of the sample.

Table 3.5 Refined structural parameters for bixbyite-  $\text{Sc}_2\text{Ti}_{0.2}\text{V}_{0.8}\text{O}_{4.5+\delta}$  ( $x = 0.2$ , s.g.  $Ia\bar{3}$ ). The lattice parameters are refined as  $a = 9.6993(4)$  Å, and  $V = 912.4(1)$  Å<sup>3</sup>.  $R_{\text{wp}}/\chi^2 = 3.10 / 1.14$ .

Atom	Site	x	y	z	SOF	B <sub>iso</sub> (Å <sup>2</sup> )
Sc/Ti/V	8a	0	0	0	1.0	0.15(5)
Sc/Ti/V	24d	0.2855(1)	0	¼	1.0	0.68(3)
O	48e	0.0958(2)	0.3589(2)	0.1296(2)	1.0	0.73(4)

Bixbyite  $\text{Sc}_2\text{Ti}_{0.8}\text{V}_{0.2}\text{O}_{4.5+\delta}$  ( $x = 0.8$ , s.g.  $Ia\bar{3}$ ) was prepared via reaction between bixbyite- $\text{Sc}_2\text{VO}_{4.5}$  and  $\text{Sc}_2\text{TiO}_{4.5+\delta}$  (reaction 2.11). The Rietveld plot is shown in figure 3.8 and refined crystallographic parameters are reported in table 3.6. Like  $\text{Sc}_2\text{TiO}_{4.5+\delta}$  ( $x = 1$ ), it is assumed bixbyite  $\text{Sc}_2\text{Ti}_{0.8}\text{V}_{0.2}\text{O}_{4.5+\delta}$  ( $x = 0.8$ ) has a mixture of  $\text{Ti}^{3+}/\text{Ti}^{4+}$  cations. The product contains 5% of  $\text{Sc}_2\text{Si}_2\text{O}_7$  impurity. In addition, an unidentified competing phase was present in all attempts of preparing this phase; peaks corresponding to the unidentified phase are shown in the figure inset. This competing phase does not match Ti-rich phases such as pseudobrookite, cubic-fluorite, or rhombohedral-fluorite structures.

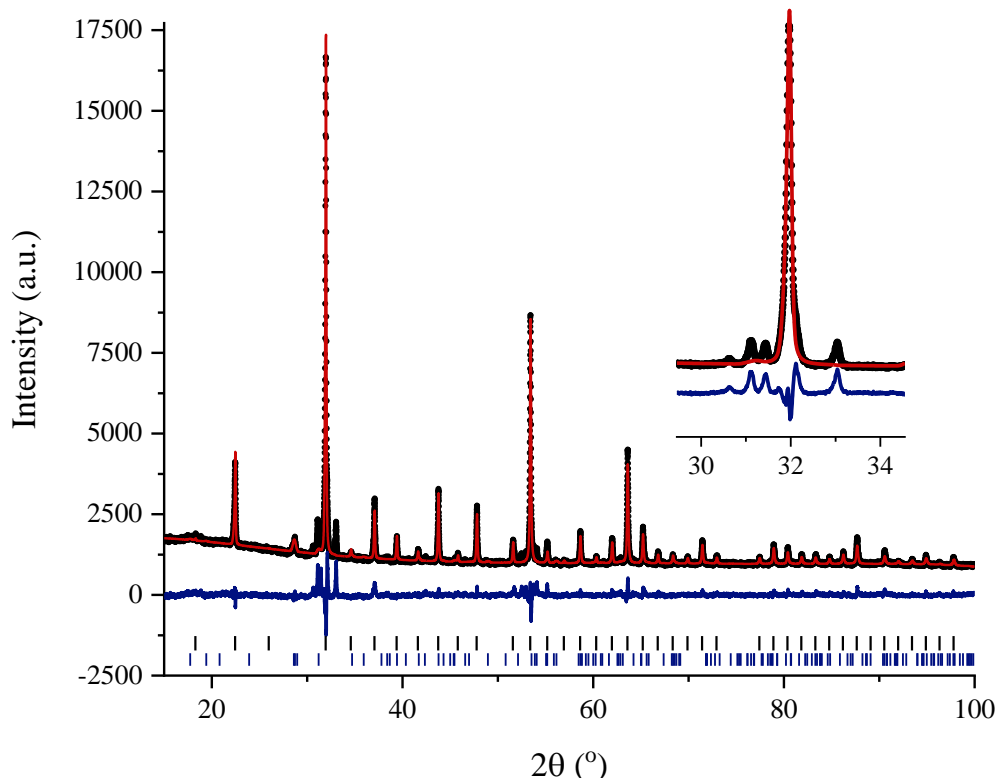


Figure 3.8 The Rietveld plot of x-ray diffraction data of  $\text{Sc}_2\text{Ti}_{0.8}\text{V}_{0.2}\text{O}_{4.5+\delta}$  ( $x = 0.8$ , s.g.  $Ia\bar{3}$ ) obtained from the reaction between  $\text{Sc}_2\text{VO}_{4.5}$  and  $\text{Sc}_2\text{TiO}_{4.5+\delta}$  (reaction 2.11) after heating at 1500°C in 5%  $\text{H}_2$  for 48 h. Black closed circles = measured data, red line = fit, blue line = difference and black and blue ticks = Bragg peaks corresponding to bixbyite and  $\text{Sc}_2\text{Si}_2\text{O}_7$  phases.

Table 3.6 Refined structural parameters for bixbyite-  $\text{Sc}_2\text{Ti}_{0.8}\text{V}_{0.2}\text{O}_{4.5+\delta}$  ( $x = 0.8$ , s.g.  $Ia\bar{3}$ ). The lattice parameters are refined as  $a = 9.698(1)$  Å, and  $V = 912.3(2)$  Å<sup>3</sup>.  $R_{\text{wp}}/\chi^2 = 5.41 / 1.91$ .

Atom	Site	x	y	z	SOF	$B_{\text{iso}}$ (Å <sup>2</sup> )
Sc/Ti/V	8a	0	0	0	1.0	0.01(7)
Sc/Ti/V	24d	0.2863(1)	0	1/4	1.0	0.01(3)
O	48e	0.0947(3)	0.3556(3)	0.1334(4)	1.0	0.93(6)

**Reactivity of Bixbyite Phases.** As previously mentioned, the bixbyite- $\text{Sc}_2\text{VO}_{4.5}$  will undergo topotactic oxidation at 400°C and the fluorite structure (s.g.  $Fm\bar{3}m$ ) will form. In contrast, if oxidation occurs at high temperature, reconstructive oxidation will occur and the tetragonal  $I\bar{4}$  structure will form.<sup>4</sup> This work investigates if similar reactivity is present in bixbyite- $\text{Sc}_2\text{Ti}_x\text{V}_{1-x}\text{O}_{4.5+\delta}$  phases. Topotactic oxidation was performed on bixbyite phases  $\text{Sc}_2\text{TiO}_{4.5+\delta}$  and  $\text{Sc}_2\text{Ti}_{0.2}\text{V}_{0.8}\text{O}_{4.5+\delta}$  ( $x = 1.0$  and  $0.2$ ) by heating in air at 400°C for 15 h. Both compositions formed the fluorite phase under these conditions. It is expected that for  $\text{Sc}_2\text{TiO}_{4.5+\delta}$ ,  $\text{Ti}^{3+}$  is oxidized to  $\text{Ti}^{4+}$ ; and for  $\text{Sc}_2\text{Ti}_{0.2}\text{V}_{0.8}\text{O}_{4.5+\delta}$   $\text{Ti}^{3+}$  and  $\text{V}^{3+}$  are oxidized to  $\text{Ti}^{4+}$  and  $\text{V}^{4+}$ . Reconstructive oxidation was performed on bixbyite phases  $\text{Sc}_2\text{TiO}_{4.5+\delta}$  and  $\text{Sc}_2\text{Ti}_{0.8}\text{V}_{0.2}\text{O}_{4.5+\delta}$  ( $x = 1.0$  and  $0.8$ ) following the slow oxidative technique outlined in 2.2.1. Oxidation of  $\text{Sc}_2\text{TiO}_{4.5+\delta}$  composition at 1100°C resulted in topotactic oxidation and the fluorite phase was obtained after heating for a total of 3 h. Notably, this process did not yield the tetragonal  $I\bar{4}$  nor the pseudobrookite phases. In contrast, reconstructive oxidation of the bixbyite  $\text{Sc}_2\text{Ti}_{0.8}\text{V}_{0.2}\text{O}_{4.5+\delta}$  ( $x = 0.8$ ) formed the tetragonal  $I\bar{4}$  phase. Analysis of this process will be discussed in detail in the following section.

## 3.2 Ordered Structure:

### 3.2.1 Background.

The tetragonal  $I\bar{4}$  structure is a unique framework where two distinct crystallographic sites form the B-sublattice. The octahedral  $\text{V}1^{8g}$  site accounts for 80% of the B-sublattice and is occupied by  $\text{V}^{3+}/\text{V}^{4+}$ , whereas the tetrahedral  $\text{V}2^{2c}$  site accounts for 20% and is occupied by  $\text{V}^{5+}$ . The large size difference between  $\text{V}1^{8g}$  and  $\text{V}2^{2c}$  sites suggests these sites can be individually controlled. The objective of this work is to substitute  $\text{Ti}^{4+}$  into the octahedral  $\text{V}1^{8g}$  site as proof of concept that the sites on the B-sublattice can be independently controlled.

Titanium(IV) is a promising candidate for substitution into the octahedral  $V1^{8g}$  site as its ionic radius is in between  $V^{4+}$  and  $V^{3+}$ ; therefore the size of the  $V1^{8g}$  site will remain constant ( $Ti^{4+}$   $r(IV) = 0.605 \text{ \AA}$ ;  $V^{3+}$   $r(IV) = 0.64 \text{ \AA}$ ;  $V^{4+}$   $r(IV) = 0.58 \text{ \AA}$ ).<sup>5</sup> Substituting a tetravalent cation into the  $V1^{8g}$  is also of particular interest as it will consequently alter the oxygen stoichiometry. Recall the parent  $Sc_2VO_5$  structure is best described as  $Sc_2V^{3+/4+}_{0.8}V^{5+}_{0.2}O_{5+\delta}$ , where oxygen stoichiometry is varied through the control of the  $V^{3+}:V^{4+}$  ratio. There are 8 anionic sites within the tetragonal  $I\bar{4}$  structure which account for 5.0 oxygen anions available per formula unit. If the  $V1^{8g}$  site was only occupied with a tetravalent cation then the oxygen content would correspond to 5.1 atoms per formula unit. Thus, the substitution of  $Ti^{4+}$  into the  $V1^{8g}$  site provides an opportunity to investigate the limits of oxygen content within the  $I\bar{4}$  structure.

### 3.2.2 Results and Discussion.

**Reconstructive Oxidation.** Reconstructive oxidation of the bixbyite  $Sc_2Ti_{0.8}V_{0.2}O_{4.5+\delta}$  phase was performed at  $1100^\circ\text{C}$  in traces of  $O_2$  according to reaction 2.17. Oxidation occurred over 6 intervals varying from 30 to 60 min, yielding a total heating time of 4.5 h. After oxidation of 4.5 h, the final black product contained 76.7(2)% of the tetragonal  $I\bar{4}$  phase and the composition is assumed to be  $Sc_2Ti_{0.8}V_{0.2}O_{5+\delta}$ . The Rietveld plot of the final product is shown in figure 3.9 and the structure is described by space group  $I\bar{4}$ . The final product contained  $Sc_2Si_2O_7$  and  $ScVO_4$  impurity phases, as well as an additional impurity phase which was not quantified due to significant peak overlap with the tetragonal  $I\bar{4}$  phase. This additional phase is suspected to be the Sc/Ti rhombohedral-fluorite structure as this phase can model additional intensity of Bragg peaks not accounted for in the Rietveld refinement. The cubic fluorite can also model this additional intensity though unlikely to be present as the cubic phase is found at synthesis temperatures  $>1250^\circ\text{C}$  (section 3.1.2). The  $Sc_2Si_2O_7$  impurity phase was present in the bixbyite precursor, thus remained in the final product. The presence of  $ScVO_4$  and Ti-rich phase impurities may be a consequence of balancing stoichiometry since some scandium is present in the silicate phase.

The refined unit cell parameters of the tetragonal- $Sc_2Ti_{0.8}V_{0.2}O_{5.1}$  phase obtained through reconstructive oxidation method were  $a = 7.77578(8)$  and  $c = 14.5895(2)$ . Note reconstructive oxidation yielded a smaller unit cell for tetragonal- $Sc_2Ti_{0.8}V_{0.2}O_{5.1}$  than the direct synthesis method (discussed in the following section). This suggests that the product obtained from reconstructive oxidation has a lower oxygen stoichiometry than the direct synthesis product. This is supported by

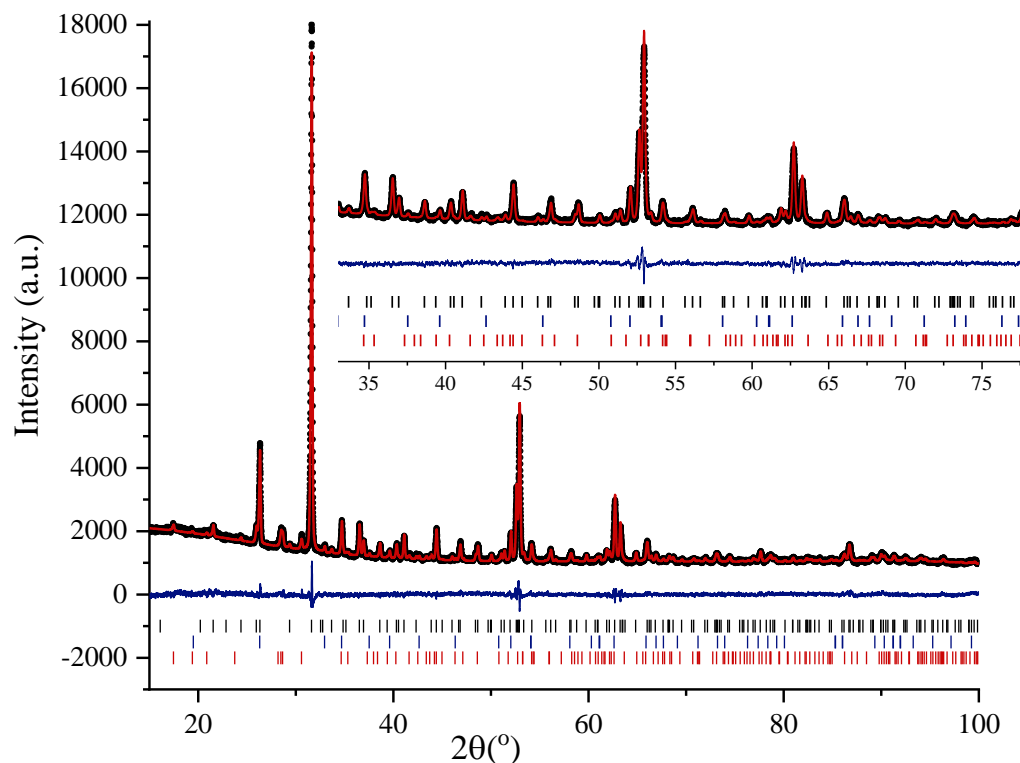


Figure 3.9 The Rietveld plot of x-ray diffraction data collected on tetragonal  $\text{Sc}_2\text{Ti}_{0.8}\text{V}_{0.2}\text{O}_{5.1}$  prepared via reconstructive oxidation of the bixbyite  $\text{Sc}_2\text{Ti}_{0.8}\text{V}_{0.2}\text{O}_{4.5}$  (reaction 2.17).  $R_{\text{wp}}/\chi^2 = 2.90/1.08$ . Black closed circles = measured data, red line = fit, blue line = difference, and black, blue and red ticks = Bragg peaks corresponding to tetragonal  $\bar{I}\bar{4}$  81.9(2)%,  $\text{ScVO}_4$  8.7(1)%, and  $\text{Sc}_2\text{Si}_2\text{O}_7$  9.4(1)% phases. The refined composition of this sample was 81.9(2)% tetragonal  $\bar{I}\bar{4}$ , 8.7(1)%  $\text{ScVO}_4$ , and 9.4(1)%  $\text{Sc}_2\text{Si}_2\text{O}_7$ .

the black colour of the product which indicates presence of reduced species, such as  $\text{Ti}^{3+}$  and  $\text{V}^{3+}$ . Though there is uncertainty with the precise structure and oxidation states present in this phase, the Rietveld analysis clearly demonstrates that the tetragonal  $\bar{I}\bar{4}$  structure is the major phase resulting from the reconstructive oxidation of bixbyite- $\text{Sc}_2\text{Ti}_{0.8}\text{V}_{0.2}\text{O}_{4.5+\delta}$

The small ionic radius of  $\text{V}^{5+}$  compared to  $\text{Sc}^{3+}$  and  $\text{Ti}^{4+}$  is predicted to drive cation ordering ( $\text{Sc}^{3+}$   $r(\text{VIII}) = 0.87 \text{ \AA}$   $\text{Ti}^{4+}(\text{VI}) = 0.605 \text{ \AA}$ ; and  $\text{V}^{5+}$   $r(\text{IV}) = 0.355 \text{ \AA}$ ).<sup>5</sup> Oxidation must be conducted at high temperature to allow cation mobility; otherwise, oxygen would be topotactically inserted into the bixbyite phase and the cation-disordered fluorite phase would form. A higher synthesis temperature of  $1100^\circ\text{C}$  was required to invoke cation migration to form the ordered-tetragonal  $\bar{I}\bar{4}$  structure of composition  $\text{Sc}_2\text{Ti}_{0.8}\text{V}_{0.2}\text{O}_{5.1}$  compared to undoped- $\text{Sc}_2\text{VO}_5$  where reconstructive oxidation occurs at  $800^\circ\text{C}$ .<sup>4</sup>

Though reconstructive oxidation of a bixbyite precursor is one method to obtain the tetragonal  $I\bar{4}$  structure, it is not a facile route. Preparation of the bixbyite phase is susceptible to forming  $\text{Sc}_2\text{Si}_2\text{O}_7$  impurity phase, and reconstructive oxidation is a tedious process that requires tracking reaction progress to prevent heating for too long. Therefore, a direct method to obtain the ordered-tetragonal  $I\bar{4}$  structure was investigated.

**Direct Synthesis.** The tetragonal- $\text{Sc}_2\text{Ti}_{0.8}\text{V}_{0.2}\text{O}_{5.1}$  (s.g.  $I\bar{4}$ ,  $x = 0.8$ ) structure was prepared by ball milling stoichiometric amounts of  $\text{Sc}_2\text{O}_3$ ,  $\text{TiO}_2$ , and  $\text{ScVO}_4$  at room temperature for 48 h then reacting in air (reaction 2.15) with a final heating step at  $1200^\circ\text{C}$ . The synthesis of  $\text{Sc}_2\text{Ti}_{0.8}\text{V}_{0.2}\text{O}_{5+\delta}$  proceeds through a detailed heating scheme with intermittent grindings, as outlined in section 2.2.1. The Rietveld plot of the refined structure is shown in figure 3.10 and refined structural parameters are reported in table 3.7. The resulting beige  $\text{Sc}_2\text{Ti}_{0.8}\text{V}_{0.2}\text{O}_{5.1}$  sample was phase pure according to powder x-ray diffraction. Homogenous distribution of  $\text{V}^{5+}$  in the starting material was of utmost importance to avoid formation of a Sc/Ti rich fluorite impurity phase. Otherwise, the starting material would contain regions of only  $\text{Sc}_2\text{O}_3$  and  $\text{TiO}_2$ , resulting in the formation of fluorite- $\text{Sc}_2\text{TiO}_5$  impurity upon heating.

Within tetragonal- $\text{Sc}_2\text{Ti}_{0.8}\text{V}_{0.2}\text{O}_{5.1}$  (s.g.  $I\bar{4}$ ,  $x = 0.8$ ),  $\text{V}^{5+}$  and  $\text{Ti}^{4+}$  are expected to occupy the tetrahedral  $\text{V}2^{2c}$  site and the octahedral  $\text{V}1^{8g}$  site, respectively. To understand the natural tendency of V and Ti to occupy the  $\text{V}1^{8g}$  and  $\text{V}2^{2c}$  sites of the B-sublattice within the tetragonal  $I\bar{4}$

Table 3.7 Refined structural parameters for tetragonal- $\text{Sc}_2\text{Ti}_{0.8}\text{V}_{0.2}\text{O}_{5.1}$  (s.g.  $I\bar{4}$ ,  $x = 0.8$ ) prepared via direct synthesis. The lattice parameters are refined as  $a = 7.80391(4)$  Å,  $c = 14.68142(8)$  Å, and  $V = 894.11(1)$  Å<sup>3</sup>.  $R_{\text{wp}}/\chi^2 = 3.17/1.1$ .

Atom	Site	x	y	z
Sc1	4f	0	1/2	0.4337(2)
Sc2	8g	0.9495(2)	0.2033(3)	0.2560(2)
Sc3	8g	0.6283(2)	0.3176(3)	0.4228(1)
V1	8g	0.2109(4)	0.1014(4)	0.4122(2)
V2	2c	0	1/2	3/4
O1	8g	0.1116(8)	0.2323(9)	0.4998(5)
O2	8g	0.8363(8)	0.3874(9)	0.3432(5)
O3	8g	0.8070(9)	0.4201(8)	0.5327(5)
O4	4e	0	0	0.6401(8)
O5	4e	0	0	0.1727(7)
O6	2a	1/2	1/2	1/2
O7	8g	0.7451(7)	0.1751(7)	0.6737(5)
O8	8g	0.0753(8)	0.3377(8)	0.6845(5)

Note: Thermal parameters for cation and anion sites were fixed to  $1.0$  Å<sup>2</sup> and  $0.5$  Å<sup>2</sup>, respectively. V1 and V2 sites are refined with only V cation on this site due to the similar electron density of Ti and V.

structure, compositions  $\text{Sc}_2\text{Ti}_x\text{V}_{1-x}\text{O}_{5+\delta}$  for  $x = 0.6$  and  $0.2$  were investigated. For  $\text{Sc}_2\text{Ti}_{0.6}\text{V}_{0.4}\text{O}_{5+\delta}$  and  $\text{Sc}_2\text{Ti}_{0.2}\text{V}_{0.8}\text{O}_{5+\delta}$  ( $x = 0.6$  and  $0.2$ ) phase pure polycrystalline samples were obtained, where the  $\delta$ -term is used to account for the uncertainty in oxygen stoichiometry for these phases as vanadium can exist in the +3, +4, and +5 -oxidation states. Refined crystallographic parameters for  $\text{Sc}_2\text{Ti}_x\text{V}_{1-x}\text{O}_{5+\delta}$  ( $x = 0.6$  and  $0.2$ ) are reported in the appendix.

In the tetragonal- $\text{Sc}_2\text{Ti}_{0.6}\text{V}_{0.4}\text{O}_{5+\delta}$  (s.g.  $\bar{I}4$ ,  $x = 0.6$ ) composition, 40% of the B-sites will be occupied by vanadium. It is expected that 0.2 mol  $\text{V}^{5+}$  will occupy the tetrahedral  $\text{V}2^{2c}$  site and the remaining 0.2 mol vanadium will occupy the octahedral  $\text{V}1^{8g}$  B-site. Vanadium(III/IV) can occupy the octahedral  $\text{V}1^{8g}$  site as demonstrated for undoped tetragonal  $\text{Sc}_2\text{VO}_5$ .<sup>4</sup> However in this reaction,  $\text{V}^{5+}$  is the only source of vanadium thus this reaction investigates if  $\text{V}^{5+}$  can partially occupy the octahedral  $\text{V}1^{8g}$  site.

Phase pure tetragonal- $\text{Sc}_2\text{Ti}_{0.6}\text{V}_{0.4}\text{O}_{5+\delta}$  (s.g.  $\bar{I}4$ ,  $x = 0.6$ ) was obtained via reaction 2.15. Like the  $x = 0.8$  composition, ball milling of starting materials was required to prevent formation of fluorite- $\text{Sc}_2\text{TiO}_5$  impurity. The Rietveld plot for the x-ray diffraction data are shown in figure

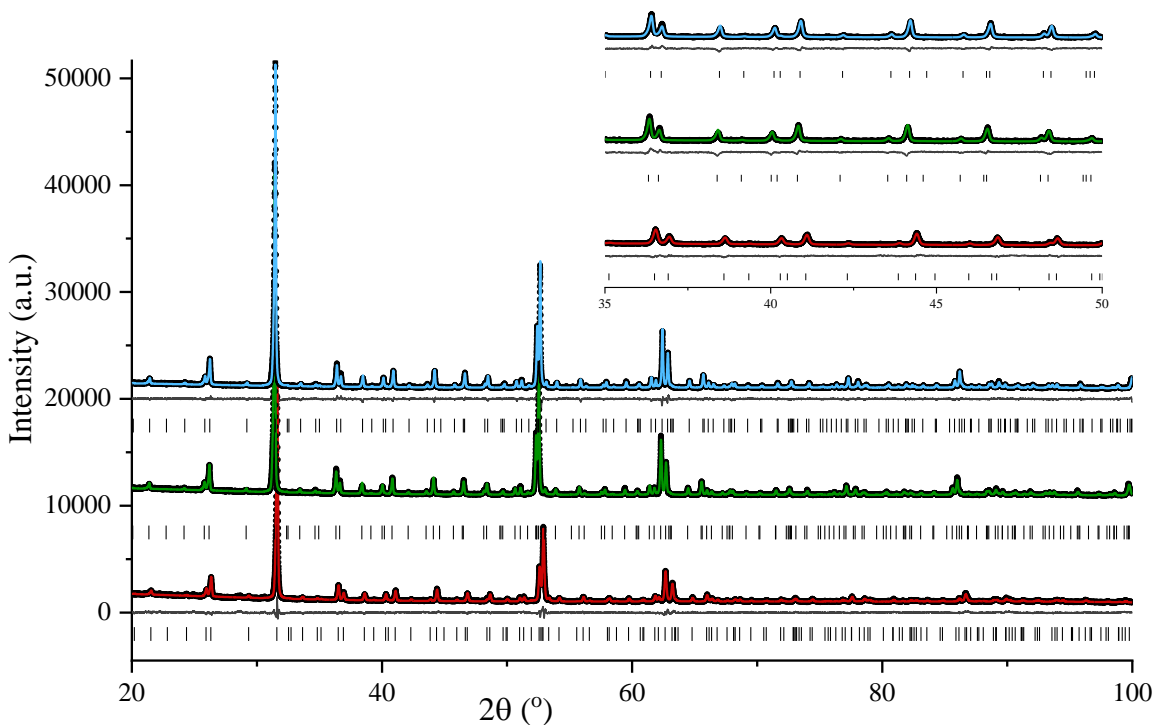


Figure 3.10 The Rietveld plots of x-ray diffraction data for tetragonal- $\text{Sc}_2\text{Ti}_x\text{V}_{1-x}\text{O}_{5+\delta}$  phases for  $x = 0.2$  (red),  $0.6$  (green) and  $0.8$  (blue). Black closed circles = measured data, coloured line = fit, grey line = difference and black ticks = Bragg peaks corresponding to tetragonal phase (s.g.  $\bar{I}4$ ).

3.10. The synthesis of  $\text{Sc}_2\text{Ti}_{0.6}\text{V}_{0.4}\text{O}_{5+\delta}$  involved multiple heatings and grindings like the  $x = 0.8$  analogue; however, an additional heating at  $1350^\circ\text{C}$  was required to obtain a phase pure sample for  $x = 0.6$  composition. After heating at  $1200^\circ\text{C}$ , the product contained 1.3%  $\text{ScVO}_4$  and 2.5%  $\text{Sc}_2\text{O}_3$  residual starting material. A higher synthesis temperature was necessary for residual  $\text{ScVO}_4$  to react. This suggests that  $\text{V}^{5+}$  partially reduced to  $\text{V}^{3+/4+}$  as lower oxidation states are often favoured at higher temperatures.  $\text{V}^{3+/4+}$  has a larger ionic radius compared to  $\text{V}^{5+}$ ; therefore, it is favourable to occupy the octahedral  $\text{V1}^{8g}$  site.

The composition  $\text{Sc}_2\text{Ti}_{0.2}\text{V}_{0.8}\text{O}_{5+\delta}$  ( $x = 0.2$ ) was considered to determine if  $\text{Ti}^{4+}$  could completely occupy the tetrahedral  $\text{V2}^{2c}$  site. Unlike composition for  $x = 0.8$  and  $0.6$ , the synthesis route for  $\text{Sc}_2\text{Ti}_{0.2}\text{V}_{0.8}\text{O}_{5+\delta}$  ( $x = 0.2$ ) was tailored to explicitly target  $\text{Ti}^{4+}$  to occupy the tetrahedral  $\text{V2}^{2c}$  site. To direct  $\text{Ti}^{4+}$  to the  $\text{V2}^{2c}$  site it is necessary to target oxidation states of vanadium that would favour being in the octahedral  $\text{V1}^{8g}$  site, namely  $\text{V}^{4+}$  or  $\text{V}^{3+}$ . If vanadium has a high propensity to fill the octahedral sites, then this would force  $\text{Ti}^{4+}$  to occupy the tetrahedral site. Vanadium(IV) oxide is used as a starting material as  $\text{V}^{4+}$  allows for a suitable amount of oxygen content to be within the structure, whereas  $\text{V}^{3+}$  would cause a lower oxygen content within the system and the bixbyite phase would be favoured. To maintain the  $\text{V}^{4+}$  oxidation state, synthesis was conducted in an evacuated quartz tube. The absence of air during the reaction may result in the reduction of cations, thus the product may have a mixture of  $\text{V}^{3+}$  and  $\text{V}^{4+}$ . However vanadium(IV) also has a natural tendency to disproportionate at high temperatures into  $\text{V}^{5+}$  and  $\text{V}^{3+}$ . Therefore, if tetragonal  $\bar{I}4$  phase forms one of two scenarios is possible:

- 1)  $\text{Ti}^{4+}$  can occupy the  $2c$  site, and  $\text{V}^{3+}$  may be present due to the slightly reducing environment of vacuum conditions; or
- 2)  $\text{V}^{4+}$  disproportionates into  $\text{V}^{3+}$  and  $\text{V}^{5+}$ , where  $\text{V}^{5+}$  will occupy the  $2c$  site and drive formation of the  $\bar{I}4$  structure.

The Rietveld plot for the x-ray diffraction data (figure 3.10) shows the product of reaction 2.16 crystallizes as a single phase in the tetragonal  $\bar{I}4$  structure. However, analysis of x-ray diffraction data is unable to reveal if  $\text{Ti}^{4+}$  occupies the octahedral  $\text{V1}^{8g}$  site or the tetrahedral  $\text{V2}^{2c}$  site. Further investigation is required to determine which of the two above scenarios occurred. Figure 3.11 compares the unit cell volumes of  $\text{Sc}_2\text{Ti}_x\text{V}_{1-x}\text{O}_{5+\delta}$  for  $x = 0.8, 0.6$  and  $0.2$  (s.g.  $\bar{I}4$ ) prepared via direct synthesis. The unit cell volume of solid state oxides is related to both the ionic

radii of cations and oxygen stoichiometry. The addition of titanium to the tetragonal- $\text{Sc}_2\text{VO}_5$  structure (s.g.  $I\bar{4}$ ) does not result in a linear relationship with unit cell volume suggesting that the oxidation state of vanadium and consequently oxygen stoichiometry varies amongst the three compositions. Though all three compositions  $\text{Sc}_2\text{Ti}_x\text{V}_{1-x}\text{O}_{5+\delta}$  ( $x = 0.8, 0.6$  and  $0.2$ ) crystallize in the tetragonal  $I\bar{4}$  structure, further investigation is required to determine valency and oxygen content in each composition.

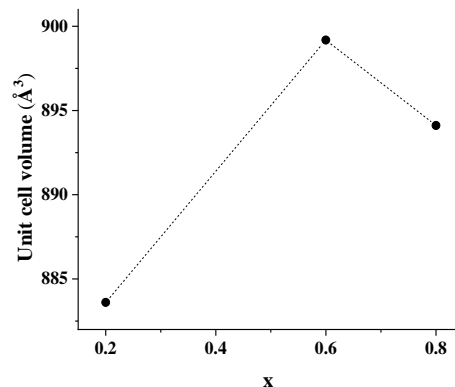


Figure 3.11 Comparison of unit cell volume for  $\text{Sc}_2\text{Ti}_x\text{V}_{1-x}\text{O}_{5+\delta}$  ( $x = 0.8, 0.6$  and  $0.2$ ).

**Coordination environment.** To understand the coordination environment of Ti and V within the tetragonal  $I\bar{4}$  structures, XANES data were collected on  $\text{Sc}_2\text{Ti}_x\text{V}_{1-x}\text{O}_{5+\delta}$  for  $x = 0.2, 0.6$ , and  $0.8$  obtained via direct synthesis. This will directly correspond to site occupancy as the  $\text{V}1^{8g}$  and  $\text{V}2^{2c}$  sites are octahedrally and tetrahedrally coordinated, respectively. The titanium edge data are shown in figure 3.12a.  $\text{Sc}_2\text{V}_{1-x}\text{Ti}_x\text{O}_{5+\delta}$  for  $x = 0.2, 0.6$ , and  $0.8$  have an identical pre-edge feature present between 4966 eV and 4971 eV. This peak agrees well with the pseudobrookite (s.g.  $Cmcm$ )  $\text{Sc}_2\text{TiO}_5$  standard, where titanium is octahedrally coordinated within the pseudobrookite structure. The pseudobrookite standard displays another feature at 4975 eV which is not found in the tetragonal structures, this feature may be attributed to the  $\text{TiO}_2$  impurity phase present in  $\text{Sc}_2\text{TiO}_5$ . XANES data support  $\text{Ti}^{4+}$  is octahedrally coordinated in all three tetragonal compositions ( $\text{Sc}_2\text{V}_{1-x}\text{Ti}_x\text{O}_{5+\delta}$  for  $x = 0.2, 0.6$ , and  $0.8$ ). As  $\text{Ti}^{4+}$  is of octahedral coordination this indicates that  $\text{Ti}^{4+}$  will occupy the octahedral  $\text{V}1^{8g}$  site in the tetragonal structure, regardless of concentration or synthesis conditions.

The vanadium edges for  $x = 0.2, 0.6$ , and  $0.8$  are shown in figure 3.12b and c. Zircon  $\text{ScVO}_4$  (s.g.  $I4_1/amd$ ,  $\text{V}^{5+}$ , tetrahedral coordination) and corundum  $\text{V}_2\text{O}_3$  (s.g.  $R\bar{3}c$ ,  $\text{V}^{3+}$ , octahedral coordination) were used as standards to provide semi-quantitative analysis of  $\text{V}^{3+}$  and  $\text{V}^{5+}$  within the tetragonal compositions. A linear combination of 25%  $\text{ScVO}_4$  and 75%  $\text{V}_2\text{O}_3$  spectra best modelled the spectrum obtained from  $\text{Sc}_2\text{Ti}_{0.2}\text{V}_{0.8}\text{O}_{5+\delta}$  ( $x = 0.2$ ). Whereas for  $\text{Sc}_2\text{Ti}_{0.6}\text{V}_{0.4}\text{O}_{5+\delta}$  ( $x = 0.6$ ), the spectrum was most accurately modelled by a linear combination of 50%  $\text{ScVO}_4$  and 50%  $\text{V}_2\text{O}_3$  spectra. Figure 3.12c compares spectra of  $\text{Sc}_2\text{V}_{0.2}\text{Ti}_{0.8}\text{O}_{5+\delta}$  ( $x = 0.8$ ) to the standard- $\text{ScVO}_4$ ,

and shows that both spectra have similar intensity of the pre-edge peak relative to the edge. From the vanadium edge spectra, the following information is obtained:

- For  $\text{Sc}_2\text{Ti}_{0.8}\text{V}_{0.2}\text{O}_{5+\delta}$  ( $x = 0.8$ ), the vanadium XANES data reveal the 0.2 vanadium is tetrahedrally coordinated, suggesting it occupies the  $\text{V}2^{2c}$  site. Thus, the  $x = 0.8$  composition can be described as:  $\text{Sc}_2(\text{Ti}^{4+}_{0.8})^{8g}(\text{V}^{5+}_{0.2})^{2c}\text{O}_{5+\delta}$ .
- For  $\text{Sc}_2\text{Ti}_{0.6}\text{V}_{0.4}\text{O}_{5+\delta}$  ( $x = 0.6$ ), tetrahedrally and octahedrally coordinated vanadium was found as a 50:50 ratio. This supports the partial reduction claim where  $\text{V}^{5+}$  occupies the tetrahedral  $\text{V}2^{2c}$  site, and additional V was reduced and occupies the octahedral  $\text{V}1^{8g}$  site. The  $x = 0.6$  composition can be described as:  $\text{Sc}_2(\text{Ti}^{4+}_{0.6}\text{V}^{3+/4+}_{0.2})^{8g}(\text{V}^{5+}_{0.2})^{2c}\text{O}_{5+\delta}$ .
- For  $\text{Sc}_2\text{Ti}_{0.2}\text{V}_{0.8}\text{O}_{5+\delta}$  ( $x = 0.2$ ), a ratio of 25:75 tetrahedral to octahedral vanadium was found. The XANES data suggests that 2 out of 8 vanadium atoms are tetrahedrally coordinated, and 6 out of 8 vanadium atoms are octahedrally coordinated. This can be rewritten as  $(\text{Sc}_2(\text{V}^{3+/4+}_{0.6}\text{Ti}^{4+}_{0.2})^{8g}(\text{V}^{5+}_{0.2})^{2c}\text{O}_{5+\delta})$  and supports the disproportionation model.

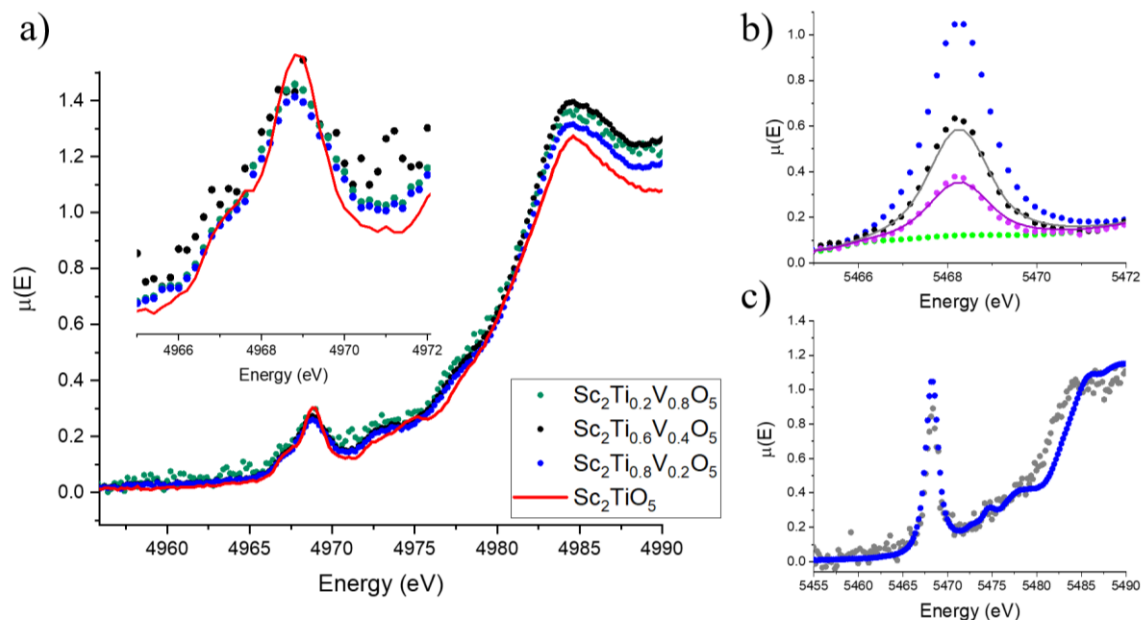


Figure 3.12 (a) XANES data of the pre-edge/edge region of the titanium K edge (transmission mode) obtained on tetragonal structures  $\text{Sc}_2\text{Ti}_{0.2}\text{V}_{0.8}\text{O}_{5+\delta}$  (dark green circles),  $\text{Sc}_2\text{Ti}_{0.6}\text{V}_{0.4}\text{O}_{5+\delta}$  (black circles),  $\text{Sc}_2\text{Ti}_{0.8}\text{V}_{0.2}\text{O}_{5.1}$  (blue circles), and  $\text{Sc}_2\text{TiO}_5$  (s.g. *Cmcm*, red line). (b) XANES data in the pre-edge region of the vanadium K edge (transmission mode) obtained on tetragonal structures  $\text{Sc}_2\text{Ti}_{0.2}\text{V}_{0.8}\text{O}_{5+\delta}$  (purple circles) and  $\text{Sc}_2\text{Ti}_{0.6}\text{V}_{0.4}\text{O}_{5+\delta}$  (black circles), and standards  $\text{ScVO}_4$  (blue circles) and  $\text{V}_2\text{O}_3$  (light green circles). Linear combination of 50:50 and 25:75  $\text{ScVO}_4$  and  $\text{V}_2\text{O}_3$  spectra are modelled by the black and purple lines, respectively. (c) XANES data in the pre-edge/edge region of the vanadium K edge (transmission mode) obtained on tetragonal structure  $\text{Sc}_2\text{Ti}_{0.8}\text{V}_{0.2}\text{O}_{5.1}$  (grey circles) and  $\text{ScVO}_4$  (blue circles).

**Oxygen Stoichiometry.** Synthesis of  $\text{Sc}_2\text{Ti}_{0.8}\text{V}_{0.2}\text{O}_{5+\delta}$  ( $x = 0.8$ ) favours  $\text{Ti}^{4+}$  and  $\text{V}^{5+}$  as  $\text{ScVO}_4$  and  $\text{TiO}_2$  were used as starting materials and the reaction was conducted in air. XANES data shows  $\text{Ti}^{4+}$  and  $\text{V}^{5+}$  are octahedrally and tetrahedrally coordinated, respectively. Thus, the oxygen stoichiometry would correspond to 51 atoms per unit cell ( $Z = 10$ ) and that is  $\delta = 0.1$ . For  $\text{Sc}_2\text{Ti}_{0.6}\text{V}_{0.4}\text{O}_{5+\delta}$  ( $x = 0.6$ ), the composition is more accurately described as  $\text{Sc}_2(\text{Ti}^{4+}_{0.6}\text{V}^{3+/4+}_{0.2})^{8g}(\text{V}^{5+}_{0.2})^{2c}\text{O}_{5+\delta}$  as revealed by XANES data. A mixture of  $\text{V}^{4+}/\text{V}^{3+}$  could be present within the structure, thus the two extreme cases in this composition are considered: (1) the octahedral  $\text{V}1^{8g}$  site is occupied by  $(\text{Ti}_{0.6}\text{V}^{4+}_{0.2})^{8g}$  corresponding to 51 oxygen anions per unit cell ( $\delta = 0.1$ ); and (2) the octahedral  $\text{V}1^{8g}$  site is occupied by  $(\text{Ti}_{0.6}\text{V}^{3+}_{0.2})^{8g}$  corresponding to 50 oxygen atoms per unit cell ( $\delta = 0$ ). The average structure could lie anywhere between these two extreme cases. Thus, the most accurate description of  $x = 0.6$  composition would be:  $\text{Sc}_2(\text{Ti}^{4+}_{0.6}\text{V}^{3+/4+}_{0.2})^{8g}(\text{V}^{5+}_{0.2})^{2c}\text{O}_{5+\delta}$  where  $\delta = 0 - 0.1$ .

For  $x = 0.8$ , a mixture of  $\text{V}^{3+/4+}$  could also be present on the octahedral  $\text{V}1^{8g}$  site. DC magnetic susceptibility measurements were conducted on  $\text{ScV}_{0.8}\text{Ti}_{0.2}\text{O}_{5+\delta}$  ( $x = 0.8$ ) to derive the oxygen stoichiometry in this phase (figure 3.13). The data were fit to the Curie-Weiss law where a  $\mu_{eff}$  of  $1.62(1) \mu_B$  and a  $\theta_{CW}$  of  $14.9(4) \text{ K}$  were extracted. The positive value of the  $\theta_{CW}$  indicates overall ferromagnetic exchange. This is unlike undoped- $\text{Sc}_2\text{VO}_5$  phase (s.g.  $I\bar{4}$ ) which exhibits net antiferromagnetic interactions.<sup>4</sup> The Curie constant,  $C$ , was used to evaluate the ratio of  $\text{V}^{3+}:\text{V}^{4+}$  occupying the octahedral  $\text{V}1^{8g}$  site. The spin-only Curie constants were calculated using equations 2.14 and 2.15. The expected spin-only Curie constants are  $C(\text{V}^{3+}) = 0.99 \text{ emu K mol}^{-1} \text{ Oe}^{-1}$ , and  $C(\text{V}^{4+}) = 0.375 \text{ emu K mol}^{-1} \text{ Oe}^{-1}$ , for the  $S = 1$ , and  $1/2$  ions, respectively. Diamagnetic ( $S = 0$ ) cations will not contribute to the Curie constant as  $C(\text{V}^{5+}, \text{Sc}^{3+} \text{ and } \text{Ti}^{4+}) = 0 \text{ emu K mol}^{-1} \text{ Oe}^{-1}$ . The experimentally obtained Curie constant,  $C$ , was found to be  $0.329(1) \text{ emu K mol}^{-1} \text{ Oe}^{-1}$  and is described as the weighted sum of the individual Curie constants (equation 3.1).

$$C_{total} = [(0.8 - x) \cdot C_{V^{4+}}] + [x \cdot C_{V^{3+}}] \quad (\text{eqn. 3.1})$$

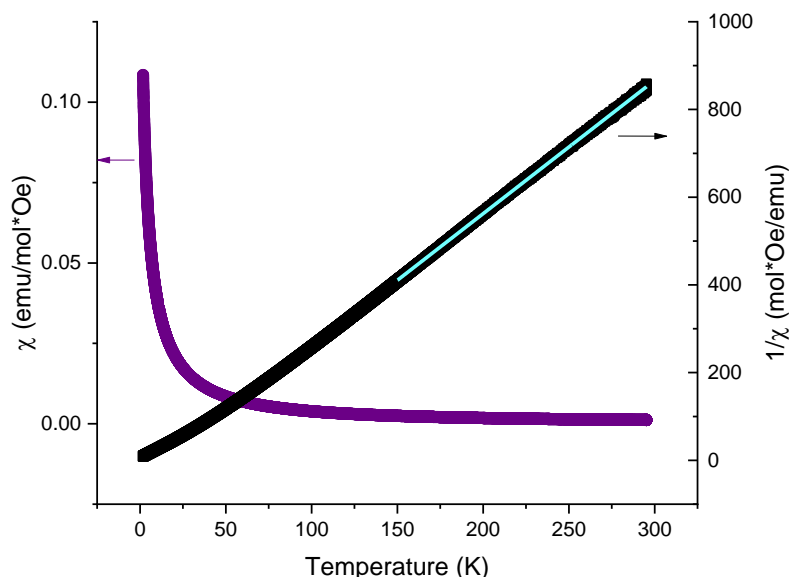


Figure 3.13. Direct current susceptibility measurements for  $\text{Sc}_2\text{V}_{0.8}\text{Ti}_{0.2}\text{O}_{5+\delta}$ . The zero-field cooled data are shown with light blue circles and the black circles represent the inverse susceptibility data and the red line is the fit to the Curie-Weiss law. All data were collected in a 0.1 T field. A diamagnetic contribution of  $-78.6 \times 10^{-6} \text{ emu mol}^{-1}$  was subtracted from the data.

Using equation 3.1, the mixture of  $\text{V}^{3+}:\text{V}^{4+}$  in  $\text{Sc}_2\text{V}_{0.8}\text{Ti}_{0.2}\text{O}_{5+\delta}$  was calculated to be 0.43  $\text{V}^{3+}$  and 0.17  $\text{V}^{4+}$ . This corresponds to a composition of  $(\text{Sc}_2(\text{V}^{3+}_{0.43}\text{V}^{4+}_{0.17}\text{Ti}^{4+}_{0.2})^{8g}(\text{V}^{5+})^{2c}\text{O}_{4.89})$ , where oxygen stoichiometry was calculated to be 48.9 atoms per unit cell ( $Z = 10$ ).

For compositions  $\text{Sc}_2\text{Ti}_x\text{V}_{1-x}\text{O}_{5+\delta}$  ( $x = 0.2, 0.6, \text{ and } 0.8$ ), the oxygen content can be controlled by varying the ratio of  $\text{Ti}^{4+}:\text{V}^{3+}:\text{V}^{4+}$  in the octahedral site. This is accomplished by two different means:

- 1) changing  $x$  (i.e.  $\text{Ti}^{4+}$  concentration); and
- 2) the oxidation state of vanadium (i.e.  $\text{V}^{3+}:\text{V}^{4+}$  ratio).

The experimentally determined oxygen stoichiometry within this series ranges from 4.89 ( $x = 0.2$ ) to 5.1 ( $x = 0.8$ ) anions per formula unit. Recall that the undoped- $\text{Sc}_2\text{VO}_5$  analogue (s.g.  $I\bar{4}$ ) phase was reported to have 4.85 oxygen anions per formula unit.<sup>4</sup> This yields the question: where are the extra oxide ions located?

In the undoped- $\text{Sc}_2\text{VO}_5$  analogue (s.g.  $I\bar{4}$ ), eight oxygen sites are filled which accounts for 50 oxygen anions within the unit cell. Additional oxygen can be inserted into the structure through oxidation of the tetragonal structure to the fluorite phase.<sup>4</sup> In this transition, oxygen is topotactically inserted and will occupy either of the remaining vacant anionic sites ( $\text{O}^{2b}$  or  $\text{O}^{8g}$ ).

Where the  $O^{2b}$  site is located at the center of the octahedral cluster, and the  $O^{8g}$  site is located around the tetrahedral  $2c$  site, as shown in figure 3.14. Neutron diffraction experiments would be required to answer this question as the scattering intensity of oxygen anions within x-ray diffraction experiments is dominated by the large scattering intensity of other cations. Oxygen anions will have enough contrast between cations within the sample with neutron diffraction, allowing for accurate determination of location and relative occupancy.

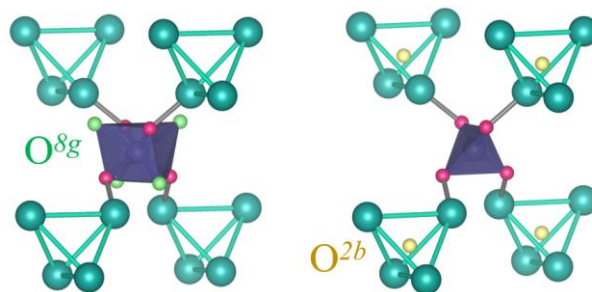


Figure 3.14. Illustration of the B-sublattice highlighting vacant anionic sites. (Left) The  $O^{8g}$  site (green) is located around the  $V2^{2c}$  site. (Right) The  $O^{2b}$  (yellow) is positioned in the center of the  $V1^{8g}$  tetrahedron.

### 3.3 Conclusion:

An understanding of disordered phases within the  $Sc_2Ti_xV_{1-x}O_{5+\delta}$  system is of benefit to avoid unwanted phases and to understand the role of  $V^{5+}$  within the ordered tetragonal structure. Although  $Sc_2Ti_{0.8}V_{0.2}O_{5.1}$  may be viewed as doping  $Ti^{4+}$  into the tetragonal- $Sc_2VO_5$  structure, it is important to stress that this composition more closely resembles the stoichiometry of  $Sc_2TiO_5$ . Thus, this composition can also be viewed as doping 0.2  $V^{5+}$  into the titanium site. Remarkably replacing 20% of titanium with  $V^{5+}$  will cause cation ordering and results in the formation of the tetragonal  $I\bar{4}$  structure.

This work obtained a phase pure sample of tetragonal- $Sc_2Ti_{0.8}V_{0.2}O_{5.1}$  (s.g.  $I\bar{4}$ ), where purity is owed to proper mixing of reagents via ball milling (previous synthesis attempts contained a fluorite impurity). During the synthesis of tetragonal- $Sc_2Ti_{0.8}V_{0.2}O_{5.1}$ , the homogenous distribution of  $ScVO_4$  in the starting material is of utmost importance to avoid formation of the fluorite- $Sc_2TiO_5$  phase. The disordered fluorite is expected to form in regions where  $V^{5+}$  is absent, thus highlighting the role of  $V^{5+}$  in forming the ordered tetragonal phase.

Vanadium(V) drives cation ordering within the tetragonal structure. At no temperature does the  $Sc_2TiO_{4.5+\delta}$  composition yield an ordered structure, whereas substituting 20% of  $Ti^{4+}$  with  $V^{5+}$  is sufficient to induce cation ordering and results in the formation of the tetragonal  $I\bar{4}$  structure. The role of  $V^{5+}$  in the formation of the ordered structure is also exemplified when oxidation of

$\text{Sc}_2\text{TiO}_{4.5}$  is considered. Oxidation of  $\text{Sc}_2\text{TiO}_{4.5}$  under the same conditions does not form the ordered tetragonal phase. Instead, the introduction of oxygen is topotactic and results in formation of a disordered fluorite phase. The ordered tetragonal  $I\bar{4}$  phase does not form in the absence of  $\text{V}^{5+}$  which highlights the ability of  $\text{V}^{5+}$  to invoke cation ordering due to its difference in size and charge. The  $\text{Sc}_2\text{TiO}_5$  is a comparable system to  $\text{Sc}_2\text{VO}_5$  in terms of oxygen stoichiometry; thus, it is reasonable to compare their structural evolution. In the vanadium system,  $\text{Sc}_2\text{VO}_{5+\delta}$ , the bixbyite phase is present at  $\delta = -0.5$ , the tetragonal ordered phase is present at  $\delta = -0.1$ , and the fluorite phase is present at  $\delta = 0.5$ . In the titanium system,  $\text{Sc}_2\text{TiO}_{5+\delta}$ , the bixbyite phase is present at  $\delta = -0.5$ , and the fluorite phase is present at  $\delta = 0$ . Thus, if the ordered tetragonal phase is found in the titanium system, it would be expected to have oxygen content between  $-0.5 < \delta < 0$ . However, the ordered tetragonal phase is not seen during slow oxidation of  $\text{Sc}_2\text{TiO}_{4.5+\delta}$  (bixbyite) to  $\text{Sc}_2\text{TiO}_5$  (fluorite). Thus, the  $\text{Sc}_2\text{TiO}_5$  system is unable to form the ordered tetragonal phase due to the absence of  $\text{V}^{5+}$  or another small and highly charged cation.

The stability of  $\text{V}^{5+}$  within the tetragonal structure is also exemplified in this chapter. Once the ordered tetragonal phase is formed, it will be stable up to temperatures of  $1350^\circ\text{C}$ . This was shown during the synthesis of  $\text{Sc}_2\text{Ti}_{0.6}\text{V}_{0.4}\text{O}_{5+\delta}$  ( $x = 0.6$ ), where a higher temperature only resulted in a partial reduction of vanadium. The lattice enthalpy of the tetragonal phase prevents  $\text{V}^{5+}$  present in the tetragonal phase from reducing. It is likely that the reduced vanadium is a result of the reduction of  $\text{ScVO}_4$ . If vanadium was reduced from the tetragonal structure, then decomposition of the tetragonal phase would be expected at high temperatures.

This work reveals that the  $\text{V}1^{8g}$  and  $\text{V}2^{2c}$  sites of the tetragonal  $I\bar{4}$  structure are individually controllable.  $\text{Ti}^{4+}$  is found to occupy the  $\text{V}1^{8g}$  site and  $\text{V}^{5+}$  occupies the  $\text{V}2^{2c}$  in all compositions. Of particular interest, the Ti containing tetragonal  $I\bar{4}$  phases have a higher oxygen stoichiometry compared to the vanadium only parent- $\text{Sc}_2\text{VO}_5$  phase. This demonstrates that the tetragonal  $I\bar{4}$  phase can accommodate additional oxide anions and the stability of this phase is not dependent on the anion sublattice. Future work in this project will include neutron diffraction experiments to determine where additional oxygen anions are located in  $\text{Sc}_2\text{V}_{1-x}\text{Ti}_x\text{O}_{5+\delta}$  ( $x = 0.2, 0.6, \text{ and } 0.8$ ) tetragonal  $I\bar{4}$  phases.

## Chapter 4: Chromium and the Scandium Vanadates

This chapter focuses on the substitution of chromium into the scandium vanadate phases, with the overall objective to obtain the tetragonal  $I\bar{4}$  structure with Cr located on the tetrahedral  $V2^{2c}$  site. Section 4.1 explores the ternary phase diagram for  $Sc^{3+}$ ,  $V^{3+}$  and  $Cr^{3+}$  oxides. This is a necessary first step to understand potential competing phases during the synthesis of the ordered tetragonal phase. Section 4.2 investigates the  $Sc_2V_{0.8}Cr_{0.2}O_{5+\delta}$  phases and a detailed structural study of the  $Sc_2V_{0.8}Cr_{0.2}O_{5+\delta}$  ordered tetragonal structure is presented.

### 4.1 Ternary Phase Diagram: $Sc^{3+} - Cr^{3+} - V^{3+}$

#### 4.1.1 Background.

The ternary phase diagram between the  $Sc^{3+} - Cr^{3+} - V^{3+}$  oxide phases is investigated in this section. Vanadium (III) oxide and chromium (III) oxide crystallize in the corundum phase (s.g.  $R\bar{3}c$ ). A solid solution can be prepared between  $V_2O_3$  and  $Cr_2O_3$  ( $V_{2-x}Cr_xO_3$ ,  $x = 0 - 2$ ), and this series will crystallize in the rhombohedral corundum structure.<sup>43</sup> In contrast, scandium (III) oxide crystallizes as a cubic bixbyite phase (s.g.  $Ia\bar{3}$ ). Lussier *et al.* reported the  $Sc_2O_3$  (bixbyite) and  $V_2O_3$  (corundum) system.<sup>44</sup> Solid solutions ( $Sc_{2-x}V_xO_3$ ) can be prepared both in the bixbyite region of the phase diagram and in the corundum region separated by a miscibility gap between  $x = 1.08$  and  $1.68$ .

As  $V_2O_3$  and  $Cr_2O_3$  both crystallize as a corundum structure, it would be expected that the scandium chromate series ( $(Sc_\alpha Cr_{1-\alpha})_2O_3$ ) would have a similar phase diagram as scandium vanadate ( $(Sc_{1-\beta}V_\beta)_2O_3$ ). A cation ordered phase is known to exist at  $\alpha = 0.75$  ( $(Sc_{0.75}Cr_{0.25})_2O_3$  or  $Sc_3CrO_6$ ) suggesting there is a fundamental difference between these two systems.

The  $Sc_3CrO_6$  phase crystallizes as a  $Mg_3TeO_6$ -type structure (s.g.  $R\bar{3}$ , #148).<sup>45</sup> The  $Mg_3TeO_6$ -type structure is a rhombohedral phase where the cationic lattice consists of three crystallographic sites and the anionic lattice consists of two sites. In the  $Sc_3CrO_6$  composition, Cr

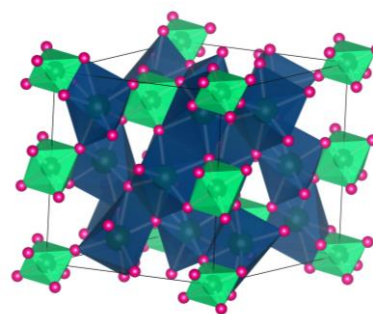


Figure 4.1 Illustration of the rhombohedral  $Sc_3CrO_6$  phase (s.g.  $R\bar{3}$ , #148). Blue =  $Sc^{3+}$  ( $18f$  site), green =  $Cr^{3+}$  ( $3a$  and  $3b$  sites), and pink =  $O^{2-}$

occupies the  $3a$  site, Sc occupies the  $18f$  site, 74:26 Cr to Sc ratio occupies the  $3b$  site, and the two anionic sites are fully occupied. Due to site mixing on the  $3b$  site, the formula unit can more accurately be written as  $\text{Sc}_{3.13}\text{Cr}_{0.87}\text{O}_6$ . The unit cell parameters for this phase are reported as  $V = 686.01 \text{ \AA}^3$ ,  $a = 8.8007 \text{ \AA}$ ,  $c = 10.2273 \text{ \AA}$ .<sup>45</sup> Figure 4.1 illustrates this structure.

The known phase diagram for  $\text{Cr}_2\text{O}_3$ ,  $\text{Sc}_2\text{O}_3$  and  $\text{V}_2\text{O}_3$  is shown in figure 4.2. No additional solid state oxide phases with a composition containing  $\text{Cr}^{3+}$ - $\text{Sc}^{3+}$ - $\text{V}^{3+}$  at ambient pressure have been reported, though it is noted at high-pressure, a  $\text{ScCrO}_3$  perovskite phase (s.g  $Pnma$ , #62) is known.<sup>46</sup> All phases reported in this system are binary and are located on the perimeter of the phase diagram. It is necessary to understand the relationship between scandium, vanadium, and chromium before the introduction of chromium into the tetragonal structure can be considered. This section explores the ternary system to understand the relationship between the  $\text{Sc}^{3+}$ ,  $\text{Cr}^{3+}$  and  $\text{V}^{3+}$  oxides.

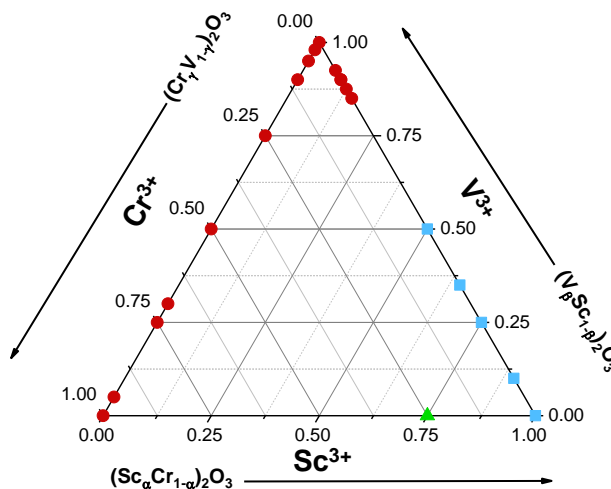


Figure 4.2 Ternary phase diagram of reported phases in the  $\text{Sc}^{3+}$  –  $\text{Cr}^{3+}$  –  $\text{V}^{3+}$  oxide system. Where bixbyite, corundum, and  $R\bar{3}$ -type phases are represented by blue squares, red circles, and green triangles, respectively.

#### 4.1.2 Results and Discussion.

All structures discussed in this section were prepared by mixing stoichiometric amounts of  $\text{Sc}_2\text{O}_3$ ,  $\text{V}_2\text{O}_3$  and  $\text{Cr}_2\text{O}_3$ , followed by heating at  $1500^\circ\text{C}$  in a reducing atmosphere.

**Scandium Chromates.** First, the scandium chromate series  $((\text{Sc}_\alpha\text{Cr}_{1-\alpha})_2\text{O}_3)$  was investigated. Unlike the scandium vanadate system  $((\text{Sc}_{1-\beta}\text{V}_\beta)_2\text{O}_3)$  which crystallize either as a bixbyite ( $\beta < 0.54$ ) or a corundum ( $\beta > 0.84$ ), the scandium chromate series has a unique structure  $\text{Sc}_3\text{CrO}_6$  ( $\alpha = 0.75$ ) which crystallizes as a  $\text{Mg}_3\text{TeO}_6$ -type structure.<sup>45</sup> A series of compositions of  $(\text{Sc}_\alpha\text{Cr}_{1-\alpha})_2\text{O}_3$  were prepared between  $\alpha = 1 - 0$ . X-ray diffraction data for the products at each composition is plotted in figure 4.3. In this series, only two intermediate compositions crystallize as single phases;  $\text{Sc}_{0.2}\text{Cr}_{1.8}\text{O}_3$  ( $\alpha = 0.1$ ) and  $\text{Sc}_{1.6}\text{Cr}_{0.4}\text{O}_3$  ( $\alpha = 0.8$ ).

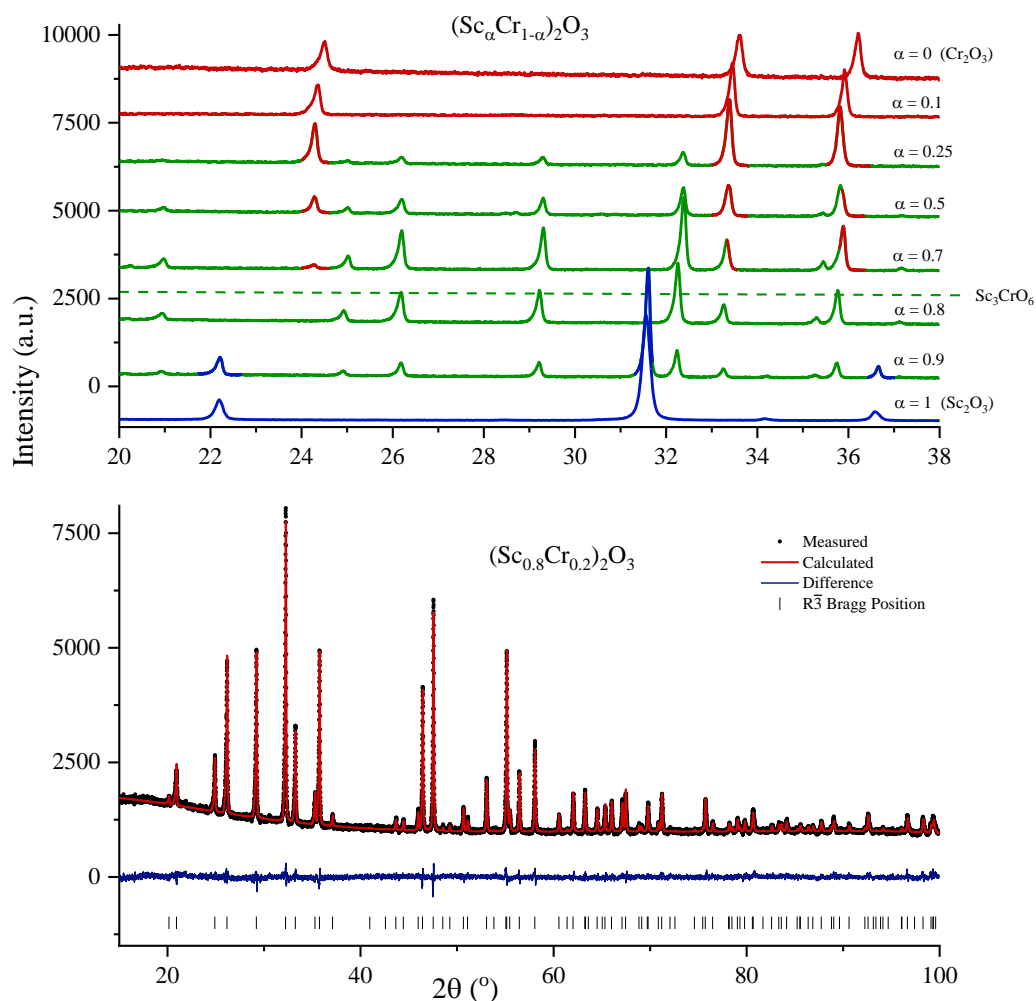


Figure 4.3 (Top) Powder X-ray diffractograms for the compositional series  $(\text{Sc}_{1-x}\text{Cr}_x)_2\text{O}_3$ . Blue peaks belong to the bixbyite phase (space group:  $Ia\bar{3}$ ), green peaks belong to  $R\bar{3}$ -type structure and red peaks belong to corundum phases (space group:  $R\bar{3}c$ ). (Bottom) Full Rietveld refinement of the powder X-ray diffraction data for  $(\text{Sc}_{0.8}\text{Cr}_{0.2})_2\text{O}_3$  where black closed circles = measured data, red line = fit, blue line = difference and black ticks = Bragg peaks corresponding to  $R\bar{3}$ -type structure.

The Rietveld plot of  $\text{Sc}_{1.6}\text{Cr}_{0.4}\text{O}_3$  ( $\alpha = 0.8$ ) is depicted in figure 4.3, and refined structural parameters are reported in table 4.1.  $\text{Sc}_{1.6}\text{Cr}_{0.4}\text{O}_3$  (or  $\text{Sc}_{3.2}\text{Cr}_{0.8}\text{O}_6$ ) crystallizes as  $\text{Mg}_3\text{TeO}_6$ -type structure (s.g.  $R\bar{3}$ ) like the  $\text{Sc}_3\text{CrO}_6$  phase. The unit cell parameters of  $\text{Sc}_{1.6}\text{Cr}_{0.4}\text{O}_3$  ( $\alpha = 0.8$ ) agree within reason to the previously reported phase of composition  $\text{Sc}_{3.13}\text{Cr}_{0.87}\text{O}_6$  ( $\alpha = 0.78$ ), suggesting these two phases are nearly identical.<sup>45</sup> The  $\text{Sc}_3\text{CrO}_6$  phase may tolerate an increased concentration of Sc due to the Sc:Cr site mixing on the  $3b$  site, though Sc doping cannot exceed 20%. This is demonstrated by  $\alpha = 0.9$  sample which did not crystallize as a single phase and residual  $\text{Sc}_2\text{O}_3$  was present. It is assumed that the additional Sc is located on the  $3b$  site due to previous literature which

states the  $3b$  site is able to accommodate Sc.<sup>45</sup> Site occupancies were not refined in this thesis as accurate determination would require use of neutron diffraction data. This previous report claims that Sc:Cr site mixing on the  $3b$  site is plausible due to the difference in bond lengths between Cr1-O1 and Cr2-O2. The Cr2<sup>3b</sup> site cavity is larger compared to the Cr1<sup>3a</sup> site; and therefore, the Cr2<sup>3b</sup> site can accommodate a limited amount of the larger cation Sc<sup>3+</sup>. In contrast, the  $R\bar{3}$  structure cannot tolerate additional Cr as a single phase was not obtained with composition Sc<sub>2.8</sub>Cr<sub>1.2</sub>O<sub>6</sub> (or (Sc<sub>0.7</sub>Cr<sub>0.3</sub>)<sub>2</sub>O<sub>3</sub>). Phase separation is favoured due to the stability of Cr<sub>2</sub>O<sub>3</sub> with octahedrally coordinated chromium(III).

Table 4.1 Refined structural parameters for (Sc<sub>0.8</sub>Cr<sub>0.2</sub>)<sub>2</sub>O<sub>3</sub>. Space group:  $R\bar{3}$  (#148),  $a = 8.8077(5)$  Å,  $c = 10.2119(7)$  Å, and  $V = 686.06(1)$  Å<sup>3</sup>.  $\chi^2/R_{wp} = 1.04/2.95$ .

Atom	Site	x	y	z	SOF*	B <sub>iso</sub> (Å <sup>2</sup> ) <sup>†</sup>
Cr1	3a	0	0	0	1.0	1.0
Sc2/Cr2	3b	0	0	½	1.0	1.0
Sc1	18f	0.0425(1)	0.2667(1)	0.2044(1)	1.0	1.0
O1	18f	0.0254(3)	0.2115(2)	0.4007(2)	1.0	0.12(7)
O2	18f	0.1849(2)	0.1593(3)	0.1204(2)	1.0	0.29(7)

\*Note: site mixing on  $3b$  site was not refined and the occupancies for all sites were fixed to 1.0.

†Thermal parameter for cations were fixed to 1.0 Å<sup>2</sup>.

The Sc<sub>0.2</sub>Cr<sub>1.8</sub>O<sub>3</sub> ( $\alpha = 0.1$ ) demonstrates that the corundum-Cr<sub>2</sub>O<sub>3</sub> phase can accommodate at least 10% Sc-doping. In contrast, the 10% Cr-doping into Sc<sub>2</sub>O<sub>3</sub> does not maintain the bixbyite structure. Instead, the addition of Cr in a Sc-rich phase favours formation of the cation-ordered  $R\bar{3}$  phase. This work contributes one point to the phase diagram as shown in figure 4.4. The addition of Sc to the corundum-Cr<sub>2</sub>O<sub>3</sub> phase is similar to corundum-V<sub>2</sub>O<sub>3</sub> which can also accommodate additional Sc as reported by Lussier *et al.*<sup>44</sup> Interestingly, the corundum-

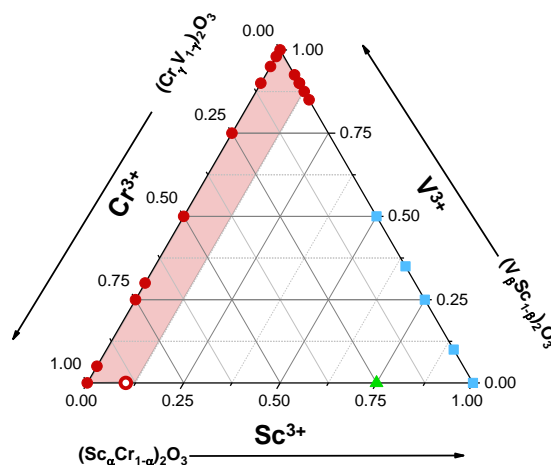


Figure 4.4 Ternary phase diagram of reported phases in the Sc<sup>3+</sup> - Cr<sup>3+</sup> - V<sup>3+</sup> - O system, including novel Sc<sub>0.2</sub>Cr<sub>1.8</sub>O<sub>3</sub> and Sc<sub>1.6</sub>Cr<sub>0.4</sub>O<sub>3</sub> phases shown by red open-circle and green open-triangle. Potential corundum region of the phase diagram is shown in red.

Sc<sub>0.2</sub>Cr<sub>1.8</sub>O<sub>3</sub> ( $\alpha = 0.1$ ) and corundum-(V<sub>β</sub>Cr<sub>1-β</sub>)<sub>2</sub>O<sub>3</sub> phases highlight a potential region of the diagram (shown in red) where Sc could be introduced into the corundum structure. Therefore,

doping of 10% of Sc to the  $(V^{3+}_{1-x}Cr^{3+x})_2O_3$  solid solutions was considered and is discussed in the following section.

**Ternary Phases.** Four ternary phases were added to the phase diagram. It is found that 10% scandium doping with the  $(V^{3+}_{1-x}Cr^{3+x})_2O_3$  solid solutions will crystallize in the corundum phase and will remain a single phase. X-ray diffraction data for  $(Sc_{0.1}V_{0.9-x}Cr_x)_2O_3$  phases are shown in figure 4.5 and table 4.2 reports structural parameters for  $(Sc_{0.1}V_{0.9-x}Cr_x)_2O_3$  ( $x = 0.1, 0.4, 0.7, 0.9$ ). Rietveld analysis of x-ray diffraction data confirms corundum phases (s.g.  $R\bar{3}c$ , #167) for all compositions, the Rietveld plot for  $x = 0.1$  is shown in figure 4.2.

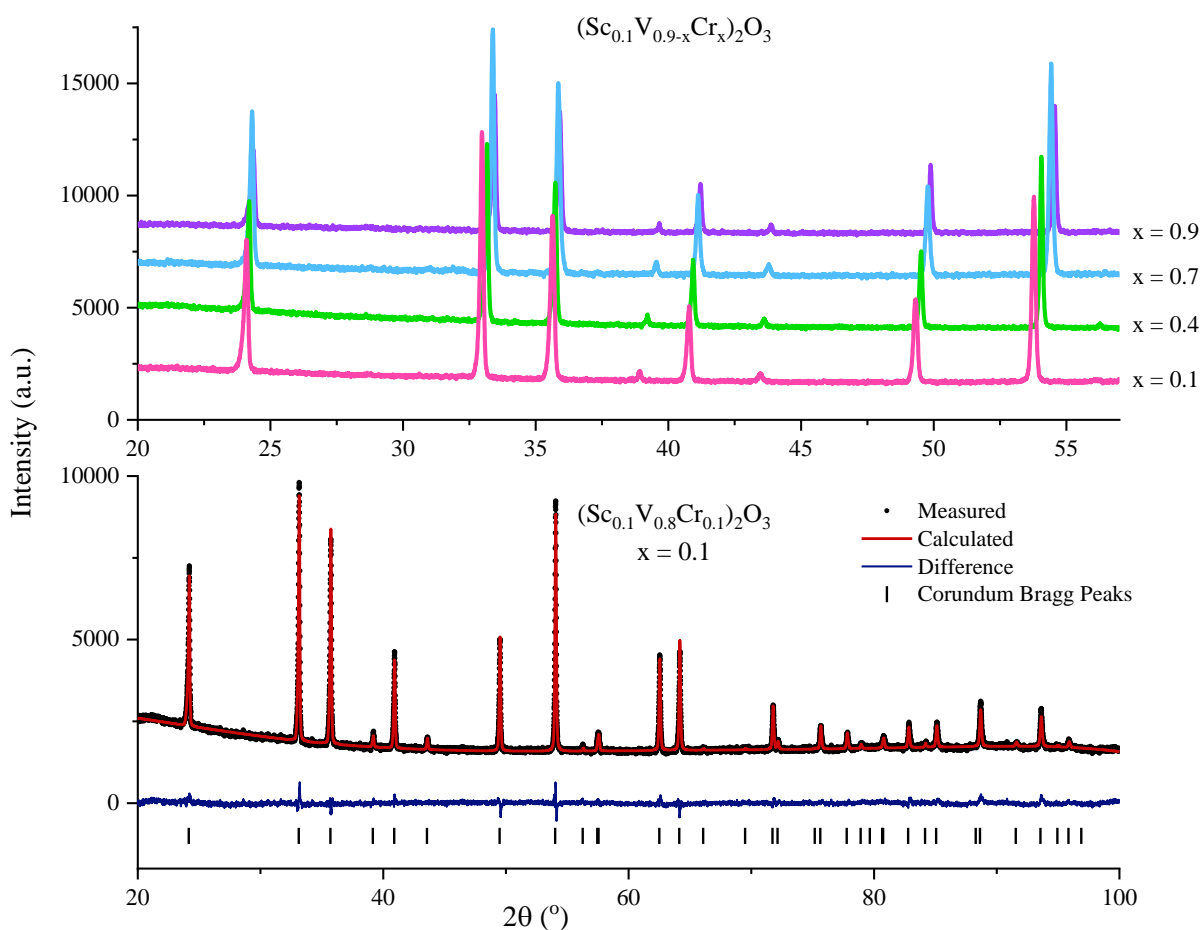


Figure 4.5 (Top) X-ray diffraction data for  $(Sc_{0.1}V_{0.9-x}Cr_x)_2O_3$  ( $x = 0.1, 0.4, 0.7, 0.9$ ). (Bottom) Full Rietveld plot for powder X-ray diffraction data for  $(Sc_{0.1}V_{0.8}Cr_{0.1})_2O_3$  where black closed circles = measured data, red line = fit, blue line = difference and black ticks = Bragg peaks corresponding to corundum phase.

Table 4.2 Refined Structural Parameters for Corundum Phases ( $\text{Sc}_{0.1}\text{V}_{0.9-x}\text{Cr}_x)_2\text{O}_3$  for  $x = 0.1, 0.4, 0.7, 0.9$  (s.g.  $R\bar{3}c$ ).

Targeted composition		$(\text{Sc}_{0.1}\text{V}_{0.8}\text{Cr}_{0.1})_2\text{O}_3$	$(\text{Sc}_{0.1}\text{V}_{0.5}\text{Cr}_{0.4})_2\text{O}_3$	$(\text{Sc}_{0.1}\text{V}_{0.2}\text{Cr}_{0.7})_2\text{O}_3$	$(\text{Sc}_{0.1}\text{Cr}_{0.9})_2\text{O}_3$
Unit Cell	a (Å)	5.0382(4)	5.0263(3)	5.0085(4)	4.9923(3)
	c (Å)	13.885(1)	13.7922(9)	13.6727(1)	13.6335(1)
	V (Å <sup>3</sup> )	305.25(5)	301.76(4)	297.02(5)	294.97(4)
Sc/V/Cr	z	0.3493(3)	0.3489(4)	0.3481(4)	0.3488(4)
$12c$ (0, 0, z)	$B_{\text{iso}}$ (Å <sup>2</sup> )	0.27(2)	0.01(1)	0.11(1)	0.01(2)
O	x	0.3032(3)	0.3018(2)	0.3039(3)	0.3003(3)
$18e$ (x, 0, 1/4)	$B_{\text{iso}}$ (Å <sup>2</sup> )	0.49(3)	0.12(3)	0.31(3)	0.07(4)
$\chi^2/R_{\text{wp}}$		1.30/2.92	1.10/2.49	1.26/2.39	0.97/2.16

The thesis also contributes a bixbyite of composition  $\text{Sc}_2\text{V}_{0.8}\text{Cr}_{0.2}\text{O}_{4.5}$ . This phase will be discussed in section 4.2.2. In total, this work contributes 5 compositions to the  $\text{Sc}^{3+}\text{-Cr}^{3+}\text{-V}^{3+}$  ternary phase diagram as shown in figure 4.6 by open symbols. Understanding this phase diagram is essential to avoid competing phases during synthesis of the ordered-tetragonal structure. The

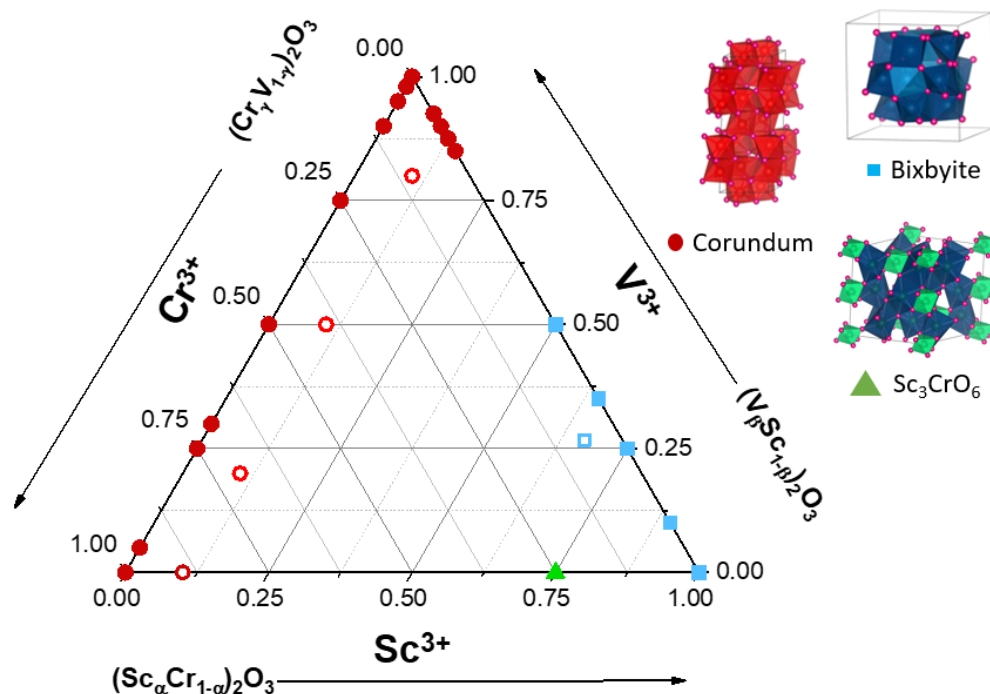


Figure 4.6 Ternary phase diagram of  $\text{Sc}^{3+} - \text{Cr}^{3+} - \text{V}^{3+} - \text{O}$  system. Where bixbyite, corundum and  $R\bar{3}$ -type phases are represented by blue squares, red circles and green triangles, respectively. Open symbols represent compositions contributed by this thesis work.

$\text{Sc}_3\text{CrO}_6$ -type structure phase is highly favourable when Sc and Cr are near a 3:1 ratio. It is also noted that  $\text{Cr}^{3+}$  has the potential to occupy the octahedral  $\text{V1}^{8g}$  site within the tetrahedral  $\bar{I}4$  structure due to its similar size and charge to  $\text{V}^{3+/4+}$ . The reaction between 0.9 mol  $\text{Sc}_2\text{O}_3$ , 0.4 mol  $\text{Cr}_2\text{O}_3$  and 0.2 mol  $\text{ScVO}_4$  was conducted in air at  $1100^\circ\text{C}$  for 30 h, similar to reaction 2.15. If this reaction yields the tetragonal  $\bar{I}4$  structure, then it would be expected that  $\text{Cr}^{3+}$  would occupy the

$\text{V1}^{8g}$  site and  $\text{V}^{5+}$  would be located in the  $\text{V2}^{2c}$  site. The x-ray diffractogram of the product of this reaction is shown in figure 4.7. The product includes  $\text{Sc}_3\text{CrO}_6$ , and unreacted  $\text{Sc}_2\text{O}_3$ ,  $\text{Cr}_2\text{O}_3$  and  $\text{ScVO}_4$  starting materials. This

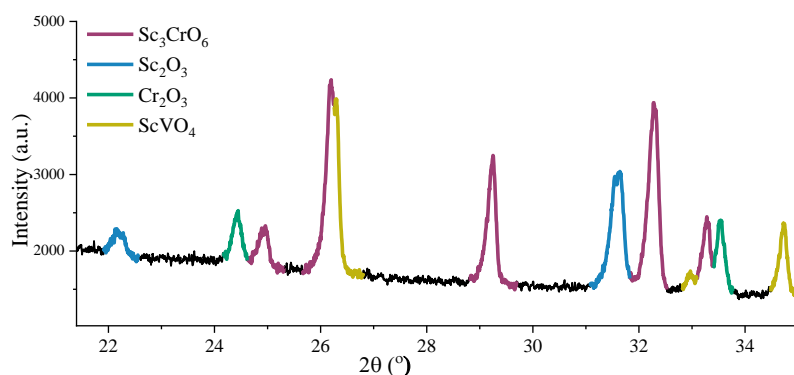


Figure 4.7 X-ray diffractogram of the products from the reactions of 0.9 mol  $\text{Sc}_2\text{O}_3 + 0.4 \text{Cr}_2\text{O}_3 + 0.1 \text{V}_2\text{O}_3$  after heating for 48 h at  $1500^\circ\text{C}$  in a reducing environment (5%  $\text{H}_2$  in  $\text{N}_2$ ).

shows that  $\text{Cr}^{3+}$  is not a viable candidate to occupy the  $\text{V1}^{8g}$  site as at a higher concentration of  $\text{Cr}^{3+}$  will have preference to form a cation ordered  $\text{Sc}_3\text{CrO}_6$  phase rather than the tetragonal  $\bar{I}4$  structure. This limits the conversation to doping the B-sublattice with a maximum of 20% Cr.

## 4.2 $\text{Sc}_2\text{V}_{0.8}\text{Cr}_{0.2}\text{O}_{5+\delta}$ phases.

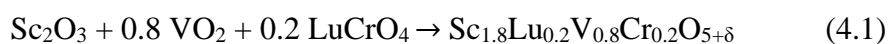
### 4.2.1 Background.

The bixbyite, fluorite and ordered-tetragonal phases are all found within the  $\text{Sc}_2\text{VO}_{5+\delta}$  family of phases, where the size, charge and amount of oxygen content are the deciding factors in structure formation. This work investigates if the same chemistry can be conducted with now substituting 20% of vanadium with chromium. This work has particular focus on targeting substitution of chromium to the tetrahedral  $\text{V2}^{2c}$  site to tune magnetic interactions within the tetragonal  $\bar{I}4$  structure. Spin-1/2 chromium(V) is a promising candidate to occupy the  $\text{V2}^{2c}$  site due to its similar size and charge as  $\text{V}^{5+}$  ( $r(\text{IV}) \text{V}^{5+}=0.355\text{\AA}$ ,  $r(\text{IV}) \text{Cr}^{5+}=0.345\text{\AA}$ ).<sup>5</sup> Though a

handful of  $\text{Cr}^{5+}$  compounds have been reported, stabilizing this uncommon phase is a significant challenge.

Leutkina reported the synthesis of the  $\text{Cr}^{5+}$  bearing zircon structure,  $\text{ScCrO}_4$  (s.g.  $I4_1/amd$ ).<sup>47</sup> This thesis work attempted the synthesis of zircon  $\text{ScCrO}_4$  following the previously reported method, but did not succeed to stabilize the +5 -oxidation state. Interestingly, the Materials Project<sup>48</sup> reports  $\text{ScCrO}_4$  composition would favour crystallization in space group  $Cmcm$ .<sup>49</sup> No additional reports of this composition have been published.

The chromium(V) oxidation state has been also reported in the  $\text{LuCrO}_4$  and  $\text{YCrO}_4$  phases,<sup>50,51</sup> where both phases crystallize as the zircon structure (s.g.  $I4_1/amd$ ).  $\text{YCrO}_4$  would not be a viable starting material for the synthesis of the ordered-tetragonal phase as it is unlikely that  $\text{Y}^{3+}$  would be able to occupy the Sc sites due to the large size difference between  $\text{Sc}^{3+}$  and  $\text{Y}^{3+}$  ( $\text{Sc}^{3+}$   $r(\text{VIII})=0.87\text{\AA}$ ;  $\text{Y}^{3+}$   $r(\text{VIII})=1.019\text{\AA}$ )<sup>5</sup>.  $\text{LuCrO}_4$  would be a more suitable candidate for a starting material as  $\text{Lu}^{3+}$  is closer in size to  $\text{Sc}^{3+}$  ( $\text{Lu}^{3+}$   $r(\text{VIII})=0.977\text{\AA}$ ).<sup>5</sup> In fact,  $\text{Lu}^{3+}$  has been partially substituted for  $\text{Sc}^{3+}$  in bixbyite- $\text{Sc}_{1-x}\text{Lu}_x\text{VO}_3$  ( $x = 0 - 0.1$ ) demonstrating  $\text{Lu}^{3+}$  and  $\text{Sc}^{3+}$  are miscible at low Lu concentration.<sup>52</sup> Phase pure  $\text{LuCrO}_4$  was prepared by the co-precipitation method adapted from previously reported procedure,<sup>28</sup> see section 2.2.1. The following reaction was then attempted using various temperatures in air to obtain the ordered-tetragonal phase with  $\text{Cr}^{5+}$  in the tetrahedral  $\text{V}2^{2c}$  site.



The chromium(V) oxidation state was not stabilized for reaction 4.1. Instead  $\text{LuCrO}_4$  decomposed and reduced to  $\text{Cr}_2\text{O}_3$  and  $\text{Lu}_2\text{O}_3$  at temperatures above 700 °C. Therefore,  $\text{LuCrO}_4$  is not a viable starting material for the tetragonal phase using conventional solid state synthesis. To further consider this reaction a sol-gel synthesis route should be investigated. Sol-gel synthesis is based on the hydrolysis and condensation of molecular precursors such as metal alkoxides or hydroxylated metal ions in aqueous solution.<sup>53</sup> One advantage sol-gel offers is the use of synthesis temperatures much lower than conventional solid state reactions. This would be an advantage in the above reaction to prevent decomposition of  $\text{LuCrO}_4$ . However, the question remains if the larger  $\text{Lu}^{3+}$  will fit into the ordered tetragonal structure.

The inability of  $\text{Cr}^{5+}$  to be stabilized at high temperature prevents it from being a suitable option during the synthesis of the tetragonal phase; consequently,  $\text{Cr}^{4+}$  is considered instead.  $\text{CrO}_2$

crystallizes in the rutile structure (s.g.  $P4_2/mnm$ ), where chromium is octahedrally coordinated. This poses a challenge as the objective is to obtain Cr in a tetrahedral environment within the tetragonal structure. However, the small ionic radius of  $\text{Cr}^{4+}$  is comparable to  $\text{V}^{5+}$ , and thus  $\text{Cr}^{4+}$  is a reasonable option to consider ( $\text{Cr}^{4+} r(\text{IV}) = 0.41 \text{ \AA}$ ,  $\text{V}^{5+} r(\text{IV}) 0.355 \text{ \AA}$ ).<sup>5</sup>

## 4.2.2 Results and Discussion.

### 4.2.2.1 Structure of $\text{Sc}_2\text{V}_{0.8}\text{Cr}_{0.2}\text{O}_{5+\delta}$ phases.

**Bixbyite.** Bixbyite- $\text{Sc}_2\text{V}_{0.8}\text{Cr}_{0.2}\text{O}_{4.5}$  (s.g.  $Ia\bar{3}$ ) was prepared by reacting corundum ( $\text{V}_{0.8}\text{Cr}_{0.2}$ ) $_2\text{O}_3$  (s.g.  $R\bar{3}c$ ) and  $\text{Sc}_2\text{O}_3$  (s.g.  $Ia\bar{3}$ ) in a 1:2 ratio to obtain bixbyite- $\text{Sc}_2\text{V}_{0.8}\text{Cr}_{0.2}\text{O}_{4.5}$  according to reaction 2.12. The reaction was conducted under reducing conditions (5%  $\text{H}_2$  in  $\text{N}_2$ ) at  $1500^\circ\text{C}$ . The Rietveld analysis of x-ray diffraction data confirms crystallization of a bixbyite phase as shown in figure 4.8. Refined crystallographic parameters are reported in table 4.3. There was a 2.13(7)%  $\text{Sc}_2\text{Si}_2\text{O}_7$  impurity present in this sample which is understood to be present due to

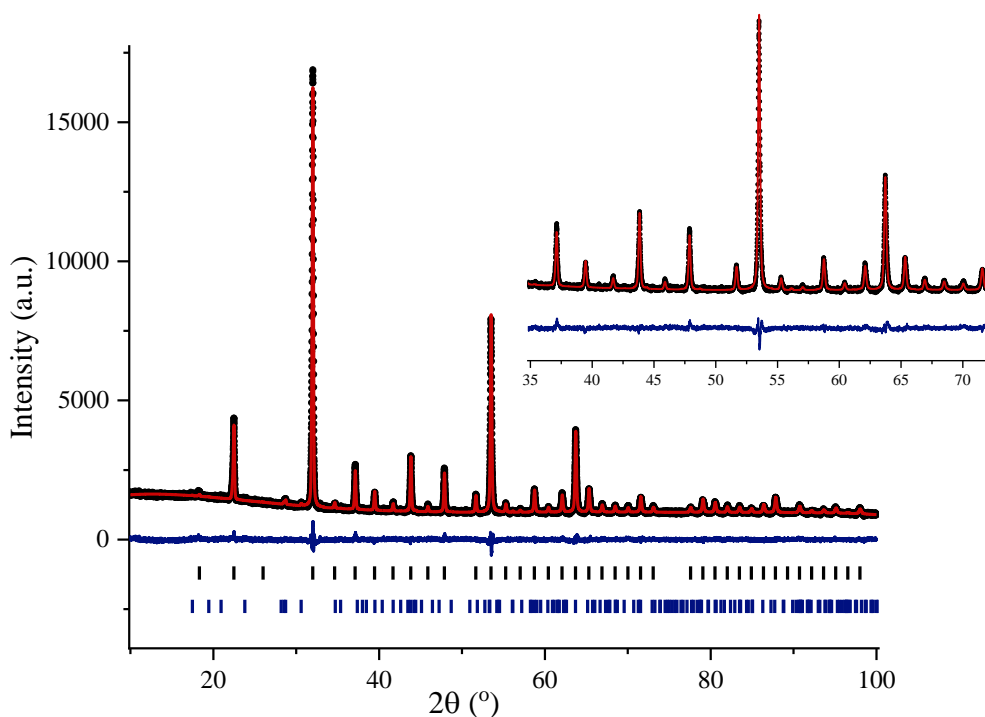


Figure 4.8 The Rietveld refinement plots of x-ray diffraction data for bixbyite-  $\text{Sc}_2\text{V}_{0.8}\text{Cr}_{0.2}\text{O}_{4.5}$  (s.g.  $Ia\bar{3}$ ) prepared via reaction 2.12. This sample contained a 2%  $\text{Sc}_2\text{Si}_2\text{O}_7$  impurity phase. Black closed circles = measured data, red line = fit, blue line = difference and black ticks = Bragg peaks corresponding to  $Ia\bar{3}$  and blue ticks = Bragg peaks corresponding to  $\text{Sc}_2\text{Si}_2\text{O}_7$  phase.

Table 4.3 Refined structural parameters for bixbyite-  $\text{Sc}_2\text{V}_{0.8}\text{Cr}_{0.2}\text{O}_{4.5+\delta}$ . Space group:  $Ia\bar{3}$ ,  $a = 9.68291(6)$  Å, and  $V = 907.85(2)$  Å<sup>3</sup>.  $\chi^2/R_{\text{wp}} = 0.98/2.79$ .

Atom	Site	x	y	z	SOF*	B <sub>iso</sub> (Å <sup>2</sup> )
Sc/Cr/V	8a	0	0	0	1.0	0.23(3)
Sc/Cr/V	24d	0.2859(1)	0	¼	1.0	0.05(2)
O	48e	0.0947(1)	0.0947(1)	0.0947(1)	1.00 (1)	0.76(6)

\*Site mixing on metal sites (8a and 24d) were not refined.

the reaction of scandium with silicate from the ceramic boat used during synthesis. It is assumed that the structure is cation-disordered as  $\text{Cr}^{3+}$  and  $\text{V}^{3+}$  are the same charge and have similar ionic radii ( $\text{Cr}^{3+}$   $r(\text{VI}) = 0.615$  Å;  $\text{V}^{3+}$   $r(\text{VI}) = 0.64$  Å).<sup>5</sup> Notably bixbyite- $\text{Sc}_2\text{V}_{0.8}\text{Cr}_{0.2}\text{O}_{4.5}$  can undergo either topotactic oxidation (at 400°C) to the fluorite phase or reconstructive oxidation (at 1100°C) to the ordered tetragonal phase.

**Fluorite.** Low temperature oxidation of  $\text{Sc}_2\text{V}_{0.8}\text{Cr}_{0.2}\text{O}_{4.5}$  will result in topotactic insertion of oxygen and the formation of the fluorite phase (reaction 2.14). A Rietveld plot of x-ray diffraction data of  $\text{Sc}_2\text{V}_{0.8}\text{Cr}_{0.2}\text{O}_{5+\delta}$  (s.g.  $Fm\bar{3}m$ ) is shown in figure 4.9, where the lattice dimension

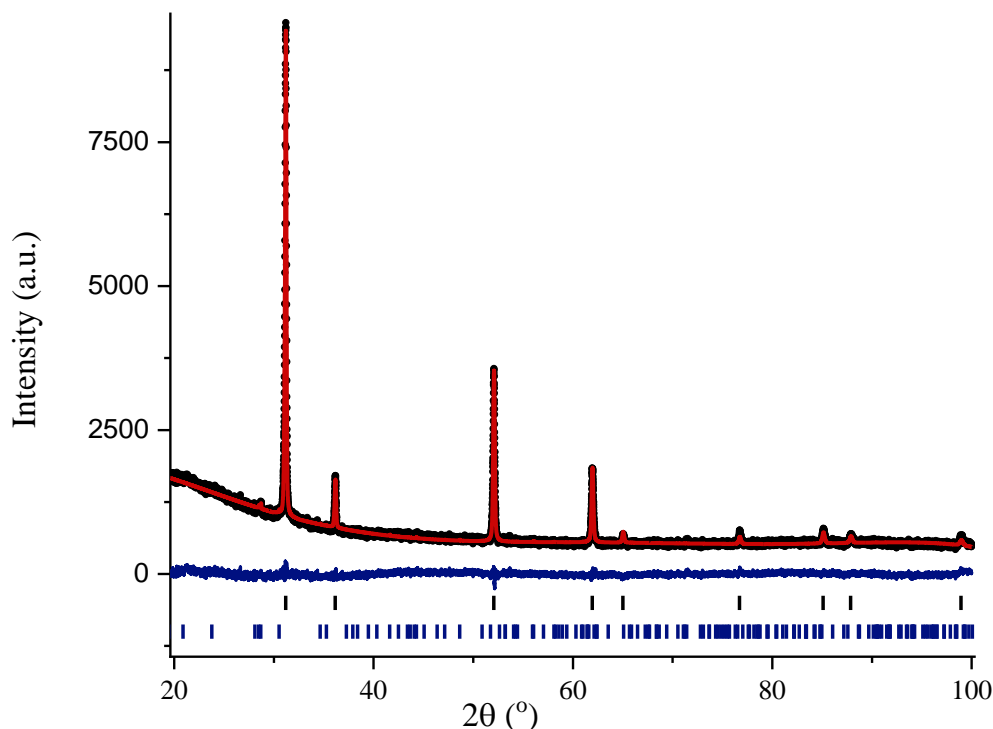


Figure 4.9 The Rietveld refinement plots of x-ray diffraction data for fluorite-  $\text{Sc}_2\text{V}_{0.8}\text{Cr}_{0.2}\text{O}_{4.5}$  (s.g.  $Fm\bar{3}m$ ) prepared via reaction 2.14. This sample contained a 2.1(6)%  $\text{Sc}_2\text{Si}_2\text{O}_7$  impurity phase. Black closed circles = measured data, red line = fit, blue line = difference and black ticks = Bragg peaks corresponding to  $Fm\bar{3}m$  and blue ticks = Bragg peaks corresponding to  $\text{Sc}_2\text{Si}_2\text{O}_7$  phase.  $\chi^2/R_{\text{wp}} = 2.65/0.98$ .

of  $a = 4.9653(7)$  Å was determined. Note the 2.1(6)%  $\text{Sc}_2\text{Si}_2\text{O}_7$  impurity present in the bixbyite precursor remains present in the fluorite product.

**Tetragonal.** Reconstructive oxidation of bixbyite- $\text{Sc}_2\text{V}_{0.8}\text{Cr}_{0.2}\text{O}_{4.5}$  occurs at  $1100^\circ\text{C}$ , according to the procedure outlined in section 2.2.1, and results in the formation of tetragonal- $\text{Sc}_2\text{V}_{0.8}\text{Cr}_{0.2}\text{O}_{5+\delta}$  (s.g.  $\bar{I}4$ ). Like the Ti-analogue, reconstructive oxidation of the Cr containing phase occurs at a higher temperature compared to the parent  $\text{Sc}_2\text{VO}_5$ .<sup>4</sup> Although the tetragonal  $\bar{I}4$  structure forms through reconstructive oxidation, it is unlikely that Cr will occupy the tetrahedral  $\text{V}2^{2c}$  site. As discussed in chapter 3, the small size of  $\text{V}^{5+}$  causes cation ordering and consequently drives formation of the tetragonal structure.  $\text{Cr}^{4+}$  is similar in size, and thus has the potential to drive cation ordering as well ( $\text{Cr}^{4+}$  r(IV) = 0.41 Å;  $\text{V}^{5+}$  r(IV) = 0.355 Å).<sup>5</sup> However, bixbyite- $\text{Sc}_2\text{V}_{0.8}\text{Cr}_{0.2}\text{O}_{4.5}$  contains  $\text{Cr}^{3+}$  which is highly stable and is not easily oxidized to the tetravalent state. In contrast,  $\text{V}^{3+}$  readily oxidizes to  $\text{V}^{5+}$ . The reconstructive oxidation of bixbyite- $\text{Sc}_2\text{V}_{0.8}\text{Cr}_{0.2}\text{O}_{4.5}$  can be considered as an oxidative competition. It is assumed that vanadium outcompetes chromium as vanadium oxidizes more readily to the pentavalent state and thus occupying the tetrahedral  $\text{V}2^{2c}$  site. The expected composition of reconstructive oxidation is  $\text{Sc}_2(\text{V}^{3/4+}_{0.6}\text{Cr}^{3+}_{0.2})^{8g}(\text{V}^{5+}_{0.2})^{2c}\text{O}_{5+\delta}$ .

A direct synthesis method was investigated to direct chromium into the tetrahedral  $\text{V}2^{2c}$  of the ordered-tetragonal phase. A bulk polycrystalline sample of tetragonal- $\text{Sc}_2\text{V}_{0.8}\text{Cr}_{0.2}\text{O}_{5+\delta}$  (s.g.  $\bar{I}4$ ) was prepared by reacting  $\text{Sc}^{3+}$ ,  $\text{Cr}^{4+}$  and  $\text{V}^{4+}$  oxides at  $1100^\circ\text{C}$  in static vacuum (reaction 2.16). Static vacuum was used in an attempt to maintain oxidation states; however, it is possible that the valencies of the cations will change when heated at high temperatures. The B-sublattice in tetragonal- $\text{Sc}_2\text{V}_{0.8}\text{Cr}_{0.2}\text{O}_{5+\delta}$  could be described by the following scenarios:

- 1) Oxidation states are maintained:  $(\text{V}^{4+}_{0.8})^{8g} (\text{Cr}^{4+}_{0.2})^{2c}$
- 2) V disproportionates:  $(\text{V}_{0.2}^{3+}\text{V}_{0.4}^{4+}\text{Cr}_{0.2}^{4+})^{8g} (\text{V}^{5+}_{0.2})^{2c}$
- 3) Cr reduces and V is oxidized:  $(\text{V}_{0.6}^{4+}\text{Cr}_{0.2}^{3+})^{8g} (\text{V}^{5+}_{0.2})^{2c}$

In the third scenario, chromium is reduced by directly interacting with its vanadium ions, causing an electron to be transferred from V to Cr. This would result in the oxidation of V and the reduction of Cr. It should also be emphasized that the actual reaction could be a combination of the three scenarios listed above.

A Rietveld refinement (figure 4.10) for tetragonal- $\text{Sc}_2\text{V}_{0.8}\text{Cr}_{0.2}\text{O}_{5+\delta}$  confirms that the  $\bar{I}4$  structure can indeed be prepared via the direct synthetic method. The tetragonal phase accounts

for approximately 90% of this sample with zircon- $\text{ScVO}_4$ , bixbyite and corundum impurity phases present. Additional characterization methods are necessary to determine if Cr is in the tetrahedral  $2c$  site. The remaining sections in this chapter investigate the structure of the tetragonal- $\text{Sc}_2\text{V}_{0.8}\text{Cr}_{0.2}\text{O}_{5+\delta}$  (s.g.  $I\bar{4}$ ) prepared via direct synthesis.

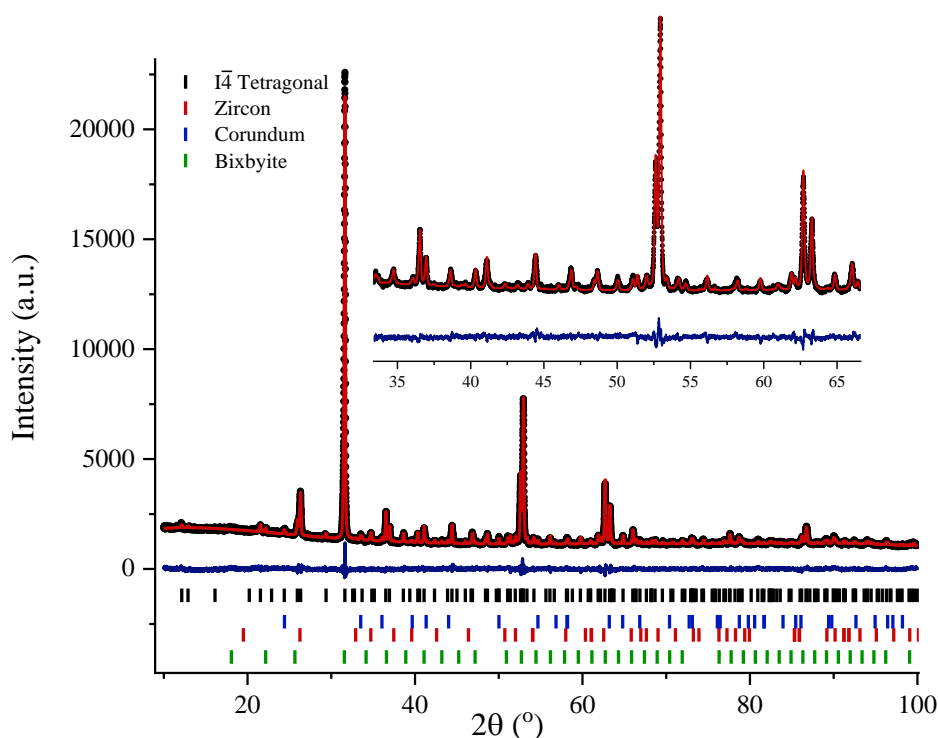


Figure 4.10 The Rietveld refinement plots of x-ray diffraction data for tetragonal-  $\text{Sc}_2\text{V}_{0.8}\text{Cr}_{0.2}\text{O}_{4.5}$  (s.g.  $I\bar{4}$ ) prepared via direct synthesis method. The Rietveld analysis suggests the sample contains 88.9(1)% tetragonal  $I\bar{4}$  structure and zircon, bixbyite and corundum impurities. Black closed circles = measured data, red line = fit, blue line = difference and ticks = Bragg peaks.

#### 4.2.2.2 Structural investigation of tetragonal- $\text{Sc}_2\text{V}_{0.8}\text{Cr}_{0.2}\text{O}_{5+\delta}$ .

**Neutron Powder Diffraction.** Room temperature neutron powder diffraction (NPD) was carried out for tetragonal- $\text{Sc}_2\text{V}_{0.8}\text{Cr}_{0.2}\text{O}_{5+\delta}$  (s.g.  $I\bar{4}$ ) prepared via direct synthesis (reaction 2.16). The Rietveld plot of the neutron diffraction data is shown in figure 4.11. Crystallographic

Table 4.4 Refined structural parameters for tetragonal-  $\text{Sc}_2\text{V}_{0.8}\text{Cr}_{0.2}\text{O}_{5+\delta}$  prepared via direct synthesis. Values were obtained from simultaneous Rietveld Refinement against x-ray and TOF neutron diffraction data. The space group is refined as  $I\bar{4}$  (#82),  $a = 7.7749(6)$  Å,  $c = 14.5867(1)$  Å, and  $V = 881.7(2)$  Å<sup>3</sup>.

Label	Site	x	y	z	$B_{iso}$
<b>Sc1</b>	4f	0	½	0.4344(2)	2.1(1)
<b>Sc2</b>	8g	0.9473(2)	0.2026(2)	0.2592(1)	0.21(5)
<b>Sc3</b>	8g	0.6308(2)	0.3203(2)	0.4246(1)	0.46(6)
<b>V1</b>	8g	0.8956(8)	0.2067(9)	0.5851(4)	0.34(5)
<b>V2</b>	2c	0	½	¼	0.1*
<b>O1</b>	8g	0.0993(3)	0.2525(4)	0.5056(2)	0.33(6)
<b>O2</b>	8g	0.8345(3)	0.3900(3)	0.3397(1)	0.1(1)
<b>O3</b>	8g	0.8134(4)	0.4169(3)	0.5253(2)	0.69(7)
<b>O4</b>	4e	0	0	0.6402(3)	0.4(1)
<b>O5</b>	4e	0	0	0.1728(2)	0.3(1)
<b>O6</b>	2a	½	½	0	0.9(2)
<b>O7</b>	8g	0.7349(4)	0.1896(4)	0.6693(2)	1.14(9)
<b>O8</b>	8g	0.0775(4)	0.3381(4)	0.6823(2)	1.04(8)

\*Fixed thermal parameter ( $B_{iso}$ ) for V2<sup>2c</sup>.

parameters are reported in table 4.4 and were obtained from the simultaneous refinement against x-ray and TOF neutron diffraction data. The Rietveld analysis of the neutron diffraction data show that the sample contains 90.4(6)% tetragonal  $I\bar{4}$  phase, 3.79(6)% bixbyite, 3.31(7)% zircon- $\text{ScVO}_4$  and 2.5(1)% corundum phases. If the corundum phase corresponds to  $\text{Cr}_2\text{O}_3$ , this would mean 29% of the available Cr would be present in the corundum phase, and the tetragonal  $I\bar{4}$  structure would have 0.14 mol of Cr in the structure. The lattice parameters of the corundum phase were refined to be  $a = b = 4.987(1)$  Å and  $c = 13.65(6)$  Å. This is slightly larger than the expected lattice parameters for  $\text{Cr}_2\text{O}_3$  which suggests the corundum composition contains both Cr and V cations (for  $\text{Cr}_2\text{O}_3$ :  $a = b = 4.959$  Å and  $c = 13.595$  Å; for  $\text{CrVO}_3$ :  $a = b = 4.986$  Å and  $c = 13.762$  Å).<sup>43</sup> As the corundum phase contains a mixture of Cr and V cations, this indicates more than 0.14 mol of Cr is likely to be located in the tetragonal  $I\bar{4}$  structure. Therefore, even though the sample has a Cr-rich impurity phase, Cr is in fact present in the tetragonal  $I\bar{4}$  structure. Notably, bixbyite and zircon- $\text{ScVO}_4$  impurities are also present in the sample, suggesting the tetragonal  $I\bar{4}$  structure may be deficient in Sc and V as well. This means the overall stoichiometry of the tetragonal  $I\bar{4}$  structure could correspond to a ratio of 20Sc:8V:2Cr. The precise determination of the tetragonal  $I\bar{4}$  phase stoichiometry is hindered by the presence of impurity phases; and so the stoichiometry is assumed

to be  $\text{Sc}_2\text{V}_{0.8}\text{Cr}_{0.2}\text{O}_{5+\delta}$  for the remaining of this chapter, though it is noted the precise composition may vary.

The neutron diffraction data reveal that there is no scattering intensity on the  $\text{V}2^{2c}$  site. The scattering length ( $b$ ) of V and Cr are -0.38, and 3.64 fm, respectively. Therefore, the absence of scattering intensity of the tetrahedral  $\text{V}2^{2c}$  site signifies V occupies this site as V is nearly neutron transparent. Whereas if Cr occupied the  $\text{V}2^{2c}$  site, scattering intensity would be present on this site. This indicates that the B-sublattice should be described as:  $(\text{V}_{0.6}^{3+\dots4+}\text{Cr}_{0.2}^{3+\dots4+})^{8g}(\text{V}^{5+}_{0.2})^{2c}$ .

Refinement of site occupancies in the structural model is limited as Cr, V and Sc have the potential to occupy the remaining sites in the tetragonal structure:  $\text{V}1^{8g}$ ,  $\text{Sc}1^{4f}$ ,  $\text{Sc}2^{8g}$ , and  $\text{Sc}3^{8g}$ . This prevents precise determination of site occupancies. The assumption that Cr only occupies the  $\text{V}1^{8g}$  site is made. It is noted that  $\text{Cr}^{3+}$  could occupy the three Sc sites ( $\text{Sc}1^{4f}$ ,  $\text{Sc}2^{8g}$  and  $\text{Sc}3^{8g}$ ). However,  $\text{Cr}^{3+}$  ( $d^3$ ) has a strong preference to be octahedrally coordinated; thus, Cr in the refinement is limited to the  $\text{V}1^{8g}$  site. Interestingly, a large amount of scattering intensity is present on the  $\text{V}1^{8g}$  site. 25% Cr occupancy (or 2/8 atoms) on  $\text{V}1^{8g}$  site cannot account for the large amount of scattering, suggesting  $\text{Sc}^{3+}$  also occupies this site ( $\text{Sc}^{3+}$   $b_{\text{coherent}} = 12.29$  fm). Despite its large ionic radius,  $\text{Sc}^{3+}$  was reported to occupy 9% of the  $\text{V}1^{8g}$  site in the parent  $\text{Sc}_2\text{VO}_5$  composition.<sup>4</sup> This suggests that  $\text{Sc}^{3+}$  can indeed partially occupy the  $\text{V}1^{8g}$  within tetragonal- $\text{Sc}_2\text{V}_{0.8}\text{Cr}_{0.2}\text{O}_{5+\delta}$  (s.g.  $\bar{I}4$ ). Constraining the occupancy of Cr to 25% of the  $\text{V}1^{8g}$  site and refining occupancy of V

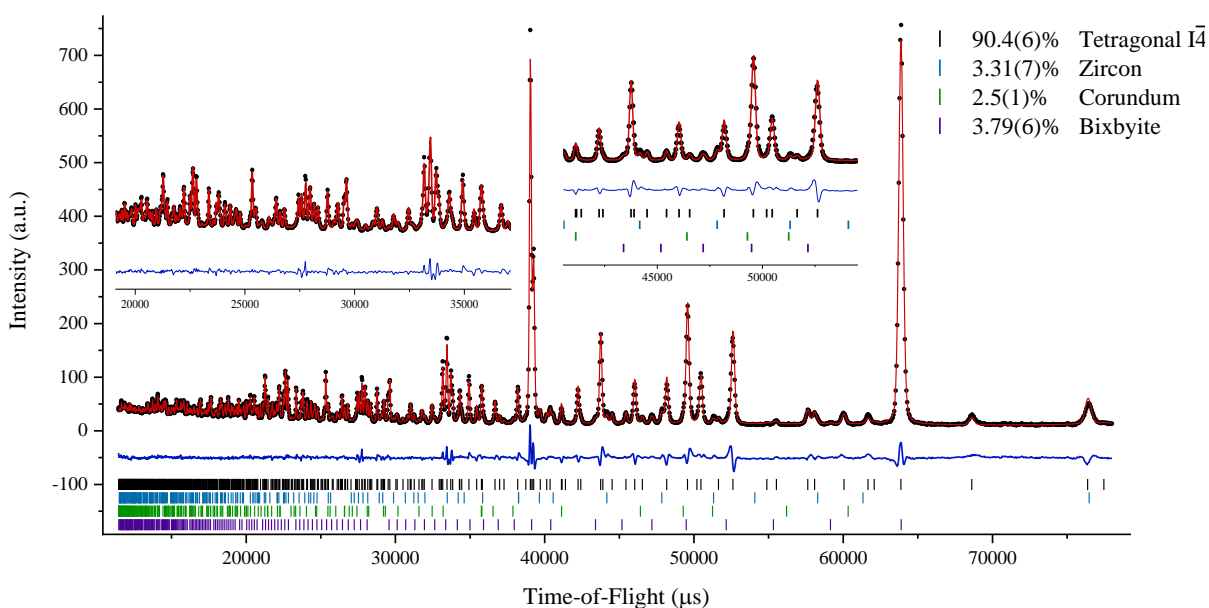


Figure 4.11 The Rietveld refinement of TOF powder neutron diffraction. Black closed circles = measured data, red line = fit, blue line = difference and ticks = Bragg peaks corresponding to respective structure.  $R_{\text{wp}}/\chi^2 = 5.16/6.05$ .

and Sc, Sc was found to occupy 18.7(9)% of the  $V1^{8g}$  site. A larger concentration of Sc on the  $V1^{8g}$  site compared to the undoped- $\text{Sc}_2\text{VO}_5$  could be due to the smaller ionic radius of Cr compared to V which allows a greater tolerance of Sc on the  $V1^{8g}$  site.

**XANES.** Vanadium K edge and chromium K edge XANES data were collected on tetragonal- $\text{Sc}_2\text{V}_{0.8}\text{Cr}_{0.2}\text{O}_{5+\delta}$  (s.g.  $I\bar{4}$ ), data are shown in figure 4.12. The vanadium K edge was compared to  $\text{ScVO}_4$  (s.g.  $I4_1/amd$ ,  $V^{5+}$ , tetrahedral coordination) and  $\text{V}_2\text{O}_3$  (s.g.  $R\bar{3}c$ ,  $V^{3+}$ , octahedral coordination) standards (figure 4.11). Linear combination of 0.25  $\text{ScVO}_4$  and 0.75  $\text{V}_2\text{O}_3$  spectra accurately describe the pre-edge peak of tetragonal- $\text{Sc}_2\text{V}_{0.8}\text{Cr}_{0.2}\text{O}_{5+\delta}$ . This corresponds to 0.2 mol  $V^{5+}$  and 0.6 mol  $V^{3+}$  present in the sample. This supports the findings from neutron diffraction which show that V is located in the tetrahedral  $V2^{2c}$  site.

The chromium K edge was compared to  $\text{CrO}_2$  ( $\text{Cr}^{4+}$ , octahedral coordination) and  $\text{Cr}_2\text{O}_3$  ( $\text{Cr}^{3+}$ , octahedral coordination) standards. If chromium were present in a 4-fold coordinated site a large pre-edge peak would be expected due to the presence of a non-centrosymmetric environment. The absence of a large peak in the spectrum suggests that chromium is in a centrosymmetric environment such as octahedral coordination.  $\text{CrO}_2$  has a larger pre-edge peak compared to  $\text{Cr}_2\text{O}_3$  as the  $\text{Cr}^{4+}$  has a lower number of  $d$  electrons than  $\text{Cr}^{3+}$  causing the  $dp$  hybridized orbital to have greater  $p$  character, allowing more electrons to be excited and a larger peak to be present. The pre-

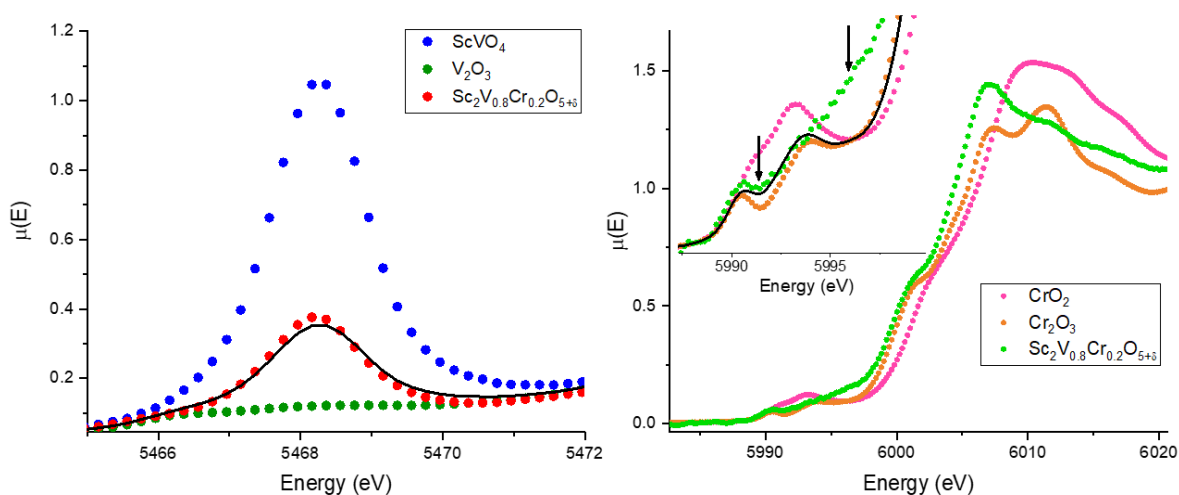
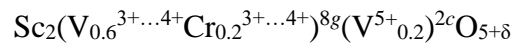


Figure 4.12 (Left) XANES data in the pre-edge region of the vanadium K edge obtained on tetragonal  $\text{Sc}_2\text{V}_{0.8}\text{Cr}_{0.2}\text{O}_{5+\delta}$  (red circles), and standards  $\text{ScVO}_4$  (blue circles) and  $\text{V}_2\text{O}_3$  (green circles). Linear combination of 25:75  $\text{ScVO}_4$  and  $\text{V}_2\text{O}_3$  spectra are modelled by the black line. (Right) XANES data of the pre-edge/edge region of the chromium K edge obtained on tetragonal structures  $\text{Sc}_2\text{V}_{0.8}\text{Cr}_{0.2}\text{O}_{5+\delta}$  (green circles),  $\text{Cr}_2\text{O}_3$  (orange circles) and  $\text{CrO}_2$  (pink circles). Inset highlights the pre-edge peaks and includes linear combination of 75:25  $\text{Cr}_2\text{O}_3$  and  $\text{CrO}_2$  spectra shown by the solid black line.

edge feature of the Cr edge tetragonal- $\text{Sc}_2\text{V}_{0.8}\text{Cr}_{0.2}\text{O}_{5+\delta}$  is comparable to  $\text{Cr}_2\text{O}_3$ , however there is additional intensity present at 5991 eV and 5996 eV. Linear combination of 0.25  $\text{CrO}_2$  and 0.75  $\text{Cr}_2\text{O}_3$  spectra fits the intensity at 5991 eV. This suggests that a mixture of  $\text{Cr}^{4+/3+}$  oxidation states may be present in tetragonal- $\text{Sc}_2\text{V}_{0.8}\text{Cr}_{0.2}\text{O}_{5+\delta}$ . The peak at 5996 eV is described by neither  $\text{Cr}_2\text{O}_3$  nor  $\text{CrO}_2$ . This feature may be due to the presence of higher coordination environment and suggests Cr could be partially occupying the  $\text{Sc}1^{4f}$ ,  $\text{Sc}2^{8g}$ , or  $\text{Sc}3^{8g}$  sites. However, spectra of additional standards with Cr in higher coordination environment would be required to support this claim.

**DC Magnetic Susceptibility.** DC magnetic susceptibility data in figure 4.13 were collected from 2 to 350 K. The inverse susceptibility was plotted with respect to temperature for the full data range where the data collected between 250 and 350 K show linear behaviour. The data were fit to the Curie-Weiss law where a  $\mu_{\text{eff}}$  of 2.25(3)  $\mu_{\text{B}}$  and a  $\theta_{\text{CW}}$  of  $-33.87(1)$  K were extracted. The negative  $\theta_{\text{CW}}$  indicates net antiferromagnetic interactions in tetragonal- $\text{Sc}_2\text{V}_{0.8}\text{Cr}_{0.2}\text{O}_{5+\delta}$ . This is similar to the undoped- $\text{Sc}_2\text{VO}_5$  analogue which also exhibits net antiferromagnetic interactions, yet  $\theta_{\text{CW}}$  for  $\text{Sc}_2\text{VO}_5$  was reported as  $-1.6(2)$  K.<sup>4</sup> This suggests that the introduction of 0.2 mol Cr increases the strength of net magnetic correlations.

The effective magnetic moment provides insight into oxygen content present in tetragonal- $\text{Sc}_2\text{V}_{0.8}\text{Cr}_{0.2}\text{O}_{5+\delta}$ . The presence of two redox active cations within tetragonal- $\text{Sc}_2\text{V}_{0.8}\text{Cr}_{0.2}\text{O}_{5+\delta}$  limits the exact determination of oxygen stoichiometry. Analysis of NPD and XANES data provides evidence that  $\text{V}^{5+}$  fully occupies the tetragonal  $\text{V}2^{2c}$  site and the composition can be described as:



where the  $\text{V}1^{8g}$  site is occupied by a mixture of  $\text{V}^{3+}$ ,  $\text{V}^{4+}$ ,  $\text{Cr}^{3+}$  and  $\text{Cr}^{4+}$ . The Curie constant,  $C$ , can be used to evaluate the ratio of  $\text{V}^{3+}:\text{V}^{4+}$  occupying the octahedral  $\text{V}2^{8g}$  site. The spin-only Curie constant was calculated using equations 2.14 and 2.15. The expected spin-only Curie constants are  $C(\text{Cr}^{3+}) = 1.875 \text{ emu K mol}^{-1} \text{ Oe}^{-1}$ ,  $C(\text{V}^{3+} \text{ and } \text{Cr}^{4+}) = 0.99 \text{ emu K mol}^{-1} \text{ Oe}^{-1}$ , and  $C(\text{V}^{4+}) = 0.375 \text{ emu K mol}^{-1} \text{ Oe}^{-1}$ , for the  $S = 3/2$ , 1, and  $1/2$  ions, respectively. Diamagnetic ( $S = 0$ ) cations will not contribute to the Curie constant as  $C(\text{V}^{5+} \text{ and } \text{Sc}^{3+}) = 0 \text{ emu K mol}^{-1} \text{ Oe}^{-1}$ . The experimentally obtained Curie constant,  $C$ , was found to be  $0.6338(4) \text{ emu K mol}^{-1} \text{ Oe}^{-1}$  and is described as the weighted sum of the individual Curie constants. Equation 4.2 relates to a composition of  $\text{Sc}_2(\text{V}^{3+}_x\text{V}^{4+}_{0.6-x}\text{Cr}^{3+}_y\text{Cr}^{4+}_{0.2-y})^{8g}(\text{V}^{5+}_{0.2})^{2c}\text{O}_{5+\delta}$ .

$$C_{total} = (0.6 - x) \cdot C_{V^{4+}} + (x \cdot C_{V^{3+}}) + (y \cdot C_{Cr^{3+}}) + (0.2 - y) \cdot C_{Cr^{4+}} \quad (4.2)$$

Assuming only  $Cr^{4+}$  ( $y = 0$ ) is present in tetragonal- $Sc_2V_{0.8}Cr_{0.2}O_{5+\delta}$  and solving for  $x$  in equation 4.2,  $x$  is found to be 0.55. This corresponds to a composition of  $Sc_2V^{3+}_{0.34}V^{4+}_{0.26}Cr^{4+}_{0.2}V^{5+}_{0.2}O_{4.93}$ . Assuming only  $Cr^{3+}$  ( $y = 0.2$ ), then  $x$  is calculated as 0.34 and corresponds to a composition of  $Sc_2V^{3+}_{0.05}V^{4+}_{0.55}Cr^{3+}_{0.2}V^{5+}_{0.2}O_{4.97}$ . The oxidation state of chromium within the structure is correlated to oxygen content and the relative amount  $V^{3+}/V^{4+}$ . XANES suggests  $Cr^{4+}$  is present in tetragonal- $Sc_2V_{0.8}Cr_{0.2}O_{5+\delta}$ ; however exact quantification is difficult. The DC susceptibility measurements suggests the oxygen stoichiometry to be between 4.93 and 4.97 mol per formula unit. This is an approximate 2.1(5)% increase in oxygen content compared to the undoped- $Sc_2VO_5$  structure that reports 4.85(3) mol of oxygen per formula unit.<sup>4</sup>

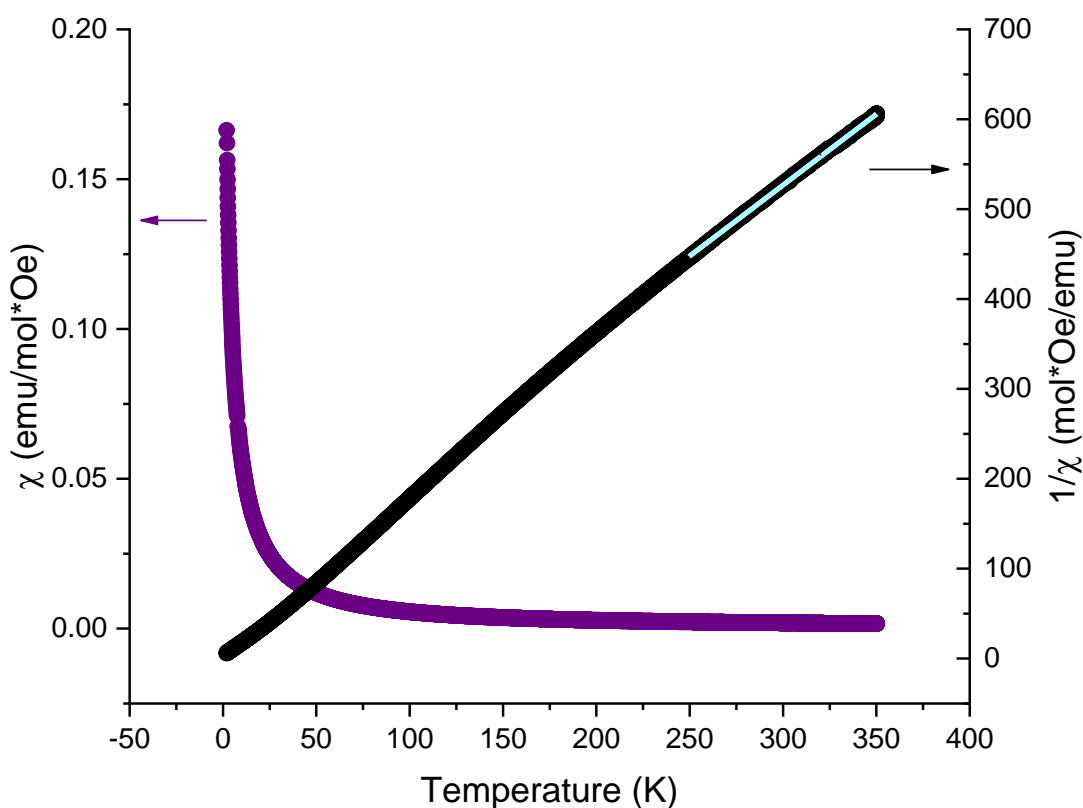


Figure 4.13 DC magnetometry data. Purple circles represent zero field cooled data. Black circles correspond to the inverse susceptibility of the field cooled data, where the blue line shows linear fit. A diamagnetic contribution of  $-79.2 \times 10^{-6} \text{ emu mol}^{-1}$  was subtracted from the data.

### 4.3 Conclusion

Section 4.1 investigates the ternary  $\text{Sc}^{3+}\text{-V}^{3+}\text{-Cr}^{3+}$  ternary phase diagram and reports five novel phases: four corundum phases of nominal composition  $(\text{Sc}_{0.1}\text{V}_{0.9-x}\text{Cr}_x)_2\text{O}_3$  for  $x = 0.1, 0.4, 0.7,$  and  $0.9$ ; and a Cr-doped scandium vanadate bixbyite  $\text{Sc}_2\text{V}_{0.8}\text{Cr}_{0.2}\text{O}_{4.5}$ .

Section 4.2 investigates  $\text{Sc}_2\text{V}_{0.8}\text{Cr}_{0.2}\text{O}_{5+\delta}$  phases with an overall objective of obtaining the tetragonal  $I\bar{4}$  phase with chromium in the tetrahedral  $\text{V}2^{2c}$  site. Notably, the  $\text{Sc}_2\text{V}_{0.8}\text{Cr}_{0.2}\text{O}_{5+\delta}$  composition can undergo the same chemistry as parent- $\text{Sc}_2\text{VO}_{5+\delta}$  phases. The bixbyite- $\text{Sc}_2\text{V}_{0.8}\text{Cr}_{0.2}\text{O}_{4.5}$  can be topotactically oxidized at low temperature and form the fluorite phase ( $\text{Sc}_2\text{V}_{0.8}\text{Cr}_{0.2}\text{O}_5$ ); or reconstructively oxidized at high temperature to yield the ordered tetragonal phase ( $\text{Sc}_2\text{V}_{0.8}\text{Cr}_{0.2}\text{O}_{5+\delta}$ ). Although the tetragonal  $I\bar{4}$  structure can be obtained through reconstructive oxidation it is expected that  $\text{V}^{5+}$  would be found in the  $\text{V}2^{2c}$  site. To target Cr in the tetrahedral  $\text{V}2^{2c}$  site, a direct synthesis method was considered.

Tetragonal-  $\text{Sc}_2\text{V}_{0.8}\text{Cr}_{0.2}\text{O}_{5+\delta}$  was obtained via direct synthesis as verified by PXD. Detailed structural analysis was completed where NPD and XANES experiments showed  $\text{V}^{5+}$  occupies the tetrahedral  $\text{V}2^{2c}$  site and  $\text{Cr}^{3/4+}$  is located on the octahedral  $\text{V}2^{8g}$  site, though site mixing with the three Sc sites is possible. DC susceptibility measurements allowed for semi-quantitative determination of oxygen content within tetragonal- $\text{Sc}_2\text{V}_{0.8}\text{Cr}_{0.2}\text{O}_{5+\delta}$  (s.g.  $I\bar{4}$ ). The oxygen stoichiometry is expected to lie between 4.93 and 4.97 mol per formula unit.

Of particular interest, the tetragonal-  $\text{Sc}_2\text{V}_{0.8}\text{Cr}_{0.2}\text{O}_{5+\delta}$  phase has a greater tolerance of Sc on the  $\text{V}1^{8g}$  site and has stronger net antiferromagnetic correlations compared to the parent  $\text{Sc}_2\text{VO}_{5+\delta}$  structure. Future steps for this work should focus on the synthesis of a phase pure sample in order to determine the precise location of Cr within the structure and to further investigate magnetic properties. Though 80% Cr-doping on the B-sublattice yields the  $\text{Sc}_3\text{CrO}_6$  structure, future work should also consider if more than 20% Cr can occupy the B-sublattice.

## Chapter 5: Conclusion

---

The tetragonal  $I\bar{4}$  structure is an interesting archetype that requires exploration to possible substitutions within the structure. The large size difference between sites suggests targeted site substitutions are possible and offers the potential for a new family of materials that crystallize in the tetragonal  $I\bar{4}$  phase to be found. This thesis investigated targeted substitution of Cr and Ti into the  $V2^{2c}$  and  $V1^{8g}$  sites in the tetragonal  $I\bar{4}$  structure.

Four compositions of the tetragonal  $I\bar{4}$  phase were prepared via direct synthesis  $Sc_2Ti_xV_{1-x}O_{5+\delta}$  ( $x = 0.2, 0.6, 0.8$ ), and  $Sc_2V_{0.8}Cr_{0.2}O_{5.1}$  as verified by x-ray diffraction. The tetragonal- $Sc_2Ti_{0.8}V_{0.2}O_{5.1}$  (s.g.  $I\bar{4}$ ) phase demonstrates that the octahedral  $V1^{8g}$  and tetrahedral  $V2^{2c}$  sites are individually controllable. XANES data revealed  $Ti^{4+}$  and  $V^{5+}$  are found in octahedral and tetrahedral environments, respectively. This suggested  $Ti^{4+}$  occupies the  $V1^{8g}$  and  $V^{5+}$  is found on the  $V2^{2c}$  site. Two additional compositions,  $Sc_2Ti_{0.6}V_{0.4}O_{5+\delta}$  ( $x = 0.6$ ) and  $Sc_2Ti_{0.2}V_{0.8}O_{5+\delta}$  ( $x = 0.2$ ), also crystallize in the tetragonal structure. XANES data showed  $Ti^{4+}$  is found in the octahedral environment in all compositions which validate the strong propensity for  $Ti^{4+}$  to occupy the  $V1^{8g}$  site.

Comparison of the  $Sc_2TiO_5$  family of phases and tetragonal- $Sc_2Ti_{0.8}V_{0.2}O_{5.1}$  suggests formation of the ordered tetragonal phase is driven by the presence of  $V^{5+}$ . The tetragonal  $I\bar{4}$  structure is not found in the  $Sc_2TiO_5$  family of phases. Yet substitution of as little as 20%  $V^{5+}$  for  $Ti^{4+}$  will cause cation ordering, suggesting formation of the tetragonal  $I\bar{4}$  structure due to the small size and large charge of  $V^{5+}$ . This poses the question: Is another cation able to initiate cation ordering and formation of the tetragonal  $I\bar{4}$  phase?

This work considered  $Cr^{4+}$  as a potential substitute for the tetrahedral  $V2^{2c}$  site. X-ray diffraction showed  $Sc_2V_{0.8}Cr_{0.2}O_{5+\delta}$  crystallized in the tetragonal  $I\bar{4}$  phase. However, neutron diffraction and XANES data revealed  $V^{5+}$  occupies the  $V2^{2c}$  site, and Cr is found in the  $V1^{8g}$  site, though potential site mixing on the Sc positions is possible. Future work should continue the search of a viable substitute for the  $V2^{2c}$  site in the tetragonal  $I\bar{4}$  structure as magnetic exchange interactions within this system could be tuned if a paramagnetic cation occupied this site. One

possible candidate is  $\text{Mn}^{5+}$  ( $r(\text{IV}) = 0.33 \text{ \AA}$ ).<sup>5</sup> However, like chromium, manganese is redox active and stabilizing  $\text{Mn}^{5+}$  may be a significant challenge.

Future work investigating the tetragonal  $I\bar{4}$  structure should consider the limits of oxygen stoichiometry. This thesis work and the report of parent  $\text{Sc}_2\text{VO}_{5+\delta}$  phase<sup>4</sup> has shown that low temperature oxidation of the tetragonal  $I\bar{4}$  structure will form the fluorite phase. However, the boundary between fluorite and the tetragonal phase is currently ambiguous. Neutron diffraction experiments on Ti-doped tetragonal  $I\bar{4}$  phases will provide insight to this boundary as Ti-doped phases have larger oxygen stoichiometry than the parent  $\text{Sc}_2\text{VO}_{5+\delta}$ . However, tuning of oxygen stoichiometry should not be limited to the B-sublattice. Doping of a +4 cation, such as  $\text{Zr}^{4+}$  on the A-sublattice would be another route to tune oxygen stoichiometry in the tetragonal  $I\bar{4}$  structure.

This thesis focused on the B-sublattice though future work should consider cation doping on the A-sublattice. This work considered partial substitution of  $\text{Lu}^{3+}$  into the A-sublattice simply because  $\text{Cr}^{5+}$  could be delivered by  $\text{LuCrO}_4$ . It was found that  $\text{LuCrO}_4$  was not a suitable starting material as this phase decomposed at high temperature, however doping of  $\text{Lu}^{3+}$  into the A-sublattice could be considered.

The scandium vanadate system offers a new playground to explore order/disorder transitions in materials where oxide vacancies, size and charge ordering determine structure formation. This thesis was motivated by the investigation by potential substitutions in the novel- $\text{Sc}_2\text{VO}_5$  structure, though understanding synthetic routes and potential competing phases required binary (Sc-Ti, Sc-Cr) and ternary (Sc-V-Cr, Sc-V-Ti) phases to be explored. Bixbyite structures

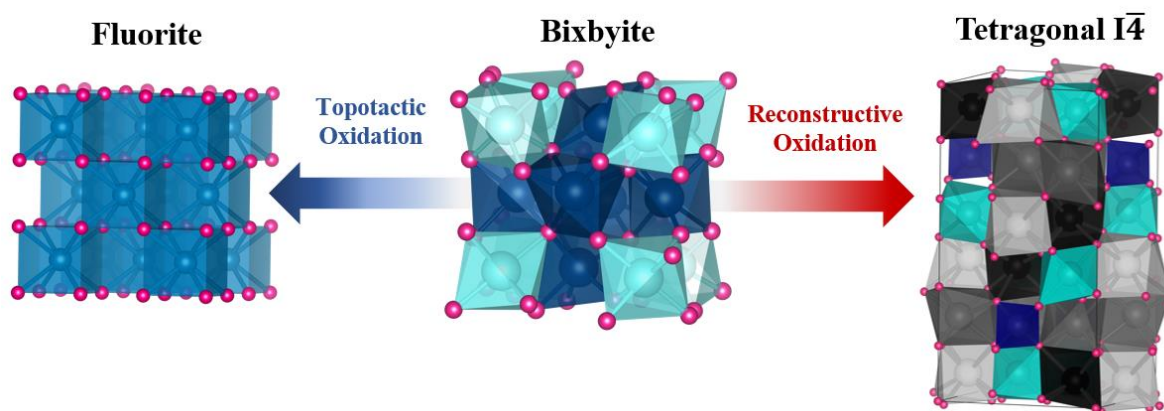


Figure 5.1 Schematic illustration of the process of oxidizing the bixbyite phases to either the tetragonal phase at high temperature (reconstructive oxidation) or the fluorite phase at low temperature (topotactic oxidation).

$\text{Sc}_2\text{Ti}_{0.8}\text{V}_{0.2}\text{O}_{4.5+\delta}$ ,  $\text{Sc}_2\text{Ti}_{0.2}\text{V}_{0.8}\text{O}_{4.5+\delta}$  and  $\text{Sc}_2\text{V}_{0.8}\text{Cr}_{0.2}\text{O}_{4.5}$  (s.g.  $Ia\bar{3}$ ,  $\text{V}^{3+}$ ) were prepared, and it was found that all Ti and Cr-doped structures demonstrate similar chemistry to undoped- $\text{Sc}_2\text{VO}_{5+\delta}$  as illustrated in figure 5.1. The Ti and Cr-doped bixbyite phases can undergo reconstructive oxidation at high temperatures to form the tetragonal  $I\bar{4}$  phase. In such case  $\text{V}^{3+}$  is oxidized to  $\text{V}^{5+}$  and then drives ordering of cations. In contrast, low temperature oxidation of the bixbyite phase is topotactic and the fluorite phase is formed. Here it is expected that  $\text{V}^{3+}$  is oxidized to  $\text{V}^{4+}$ . It is expected that the topotactic addition of oxygen is a reversible process and reduction of the fluorite would result in the formation of the bixbyite phase. Future work should consider reduction of fluorite phases, and in-situ x-ray diffraction experiments would be of benefit to track progress of oxidation/reduction processes.

In addition to using redox chemistry, this work also highlighted that annealing temperature can be used to control structure, this is demonstrated by the  $\text{Sc}_2\text{TiO}_{5+\delta}$  composition. This composition crystallized in the cation- and anion-disordered cubic-fluorite (s.g.  $Fm\bar{3}m$ ) structure at  $1500^\circ\text{C}$ . At lower synthesis temperatures, the cation-disordered and anion-ordered structure pseudobrookite phase (s.g.  $Cmcm$ ) was the dominant phase; though it is noted that rhombohedral-fluorite and bixbyite competing phases were present. Interestingly annealing between high and low temperatures can control which structure is favoured.

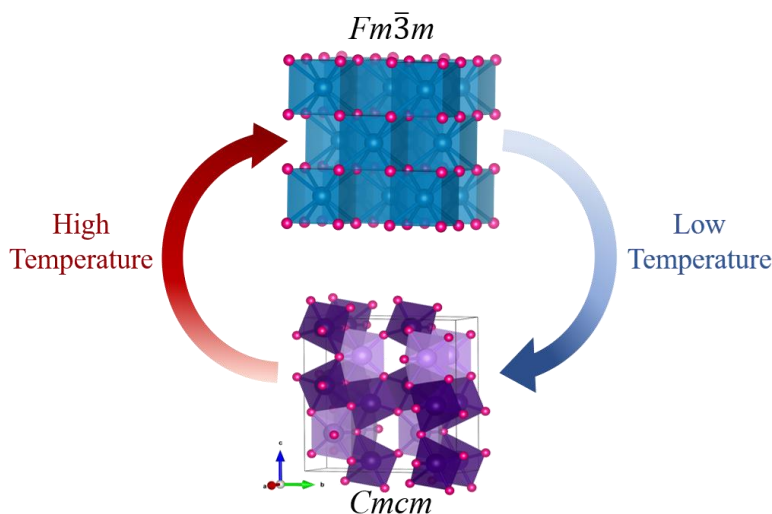


Figure 5.2 Illustration of structural transition in  $\text{Sc}_2\text{TiO}_5$ , where the anion disordered fluorite structure (s.g.  $Fm\bar{3}m$ ) is found at high temperature and the anion ordered pseudobrookite structure (s.g.  $Cmcm$ ) is found at low temperature.

The structural transitions in  $\text{Sc}_2\text{Ti}_x\text{V}_{1-x}\text{O}_{5+\delta}$  and  $\text{Sc}_2\text{TiO}_5$  compositions demonstrate how redox chemistry and temperature can be used to control order and disorder within a system. This is of particular significance when synthesis of ion conducting materials is considered. The defect fluorite structure allows for ion conduction as the disordered anionic lattice enables oxygen to hop between energetically equivalent positions. If the oxide sublattice and oxide vacancies are ordered the oxide ion mobility is expected to be low and thus oxide ion conduction would be prevented. Therefore, understanding the relationship between ordered and disordered structures is essential for the synthesis of a functional electrolyte. This is simply one example that signifies how material properties are dependent on its structure, though understanding of structure should be applied across all branches of solid state chemistry applications as a material properties are highly correlated to its structure.

## References

- (1) Parkinson, B.; Parkinson, B. The Emerging Art of Solid-State Synthesis Published by : American Association for the Advancement of Science The Emerging Art of Solid-State Synthesis. **1995**, 270 (5239), 1157–1158.
- (2) Mikhailov, Y. Y.; Pokrovskii, B. .; Komissarova, L. N. New Phases in the System Sc-V-O. *Dokl. Chem.* **1971**, 193, 403–404.
- (3) Cong, H.; Zhang, H.; Yao, B.; Yu, W.; Zhao, X.; Wang, J.; Zhang, G. ScVO<sub>4</sub>: Explorations of Novel Crystalline Inorganic Optical Materials in Rare-Earth Orthovanadate Systems. *Cryst. Growth Des.* **2010**, 10 (10), 4389–4400..
- (4) Vrublevskiy, D.; Lussier, J. A.; Panchuk, J. R.; Mauws, C.; Beam, J. C.; Wiebe, C. R.; Grosvenor, A. P.; Bieringer, M. Understanding the Interplay of Vacancy, Cation, and Charge Ordering in the Tunable Sc<sub>2</sub>VO<sub>5+δ</sub> Defect Fluorite System. *Inorg. Chem.* **2021**, 60 (2), 872–882.
- (5) Shannon, R. D. Revised Effective Ionic Radii and Systematic Studies of Interatomic Distances in Halides and Chalcogenides. *Acta Crystallogr. A.* **1976**, 32 (5), 751–767.
- (6) Shafi, S. P.; Lundgren, R. J.; Cranswick, L. M. D.; Bieringer, M. Formation, Structure and Magnetism of the Metastable Defect Fluorite Phases AVO<sub>3.5+x</sub> (A=In, Sc). *J. Solid State Chem.* **2007**, 180 (12), 3333–3340.
- (7) Shafi, S. P.; Hernden, B. C.; Cranswick, L. M. D.; Hansen, T. C.; Bieringer, M. Topotactic Oxidation Pathway of ScTiO<sub>3</sub> and High-Temperature Structure Evolution of ScTiO<sub>3.5</sub> and Sc<sub>4</sub>Ti<sub>3</sub>O<sub>12</sub>-Type Phases. *Inorg. Chem.* **2012**, 51 (3), 1269–1277.
- (8) Greedan, J. E. Geometrically Frustrated Magnetic Materials. *J. Mater. Chem.* **2001**, 11 (1), 37–53.
- (9) Broholm, C.; Cava, R. J.; Kivelson, S. A.; Nocera, D. G.; Norman, M. R.; Senthil, T. Quantum Spin Liquids. *Science* (80-. ). **2020**, 367 (6475).
- (10) Balents, L. Spin Liquids in Frustrated Magnets. *Nature* **2010**, 464 (7286), 199–208.
- (11) Anderson, P. W. Resonating Valence Bonds: A New Kind of Insulator? *Mat. Res. Bull.* **1973**, 8, 153–160.
- (12) Pecharsky, V. K.; Zavalij, P. Y. *Fundamentals of Powder Diffraction and Structural Characterization of Materials*; Springer, 2005.
- (13) Brown, P. J.; Fox, A. G.; Maslen, E. N.; O’Keefe, M. A.; Willis, B. T. M. International Tables for Crystallography; 2006; Vol. C, pp 554–595.
- (14) Sears, V. F. Neutron Scattering Lengths and Cross Sections. *Neutron News* **1992**, 3 (3), 26–37.
- (15) How SNS Works | Neutron Science at ORNL <https://neutrons.ornl.gov/content/how-sns-works> (accessed Jun 23, 2020).
- (16) Huq, A.; Hodges, J. P.; Gourdon, O.; Heroux, L. Powgen: A Third-Generation Highresolution High-Throughput Powder Diffraction Instrument at the Spallation Neutron Source. *Z. Krist. Proc.* **2011**, No. November.
- (17) Young, R. A. *The Rietveld Method*; Oxford: New York, New York, USA, 1995.
- (18) Mccusker, L. B.; Von Dreele, R. B.; Cox, D. E.; Louër, D.; Scardi, P. Rietveld Refinement Guidelines. *J. Appl. Crystallogr.* **1999**, 32 (1), 36–50.
- (19) Rodriguez-Carvajal, J. FullProf Suite. *Phys. B.* **1993**, 192 (55).
- (20) Coelho, A. A. TOPAS Academic. **2015**.
- (21) Cheary, R. W.; Coelho, A. A.; Cline, J. P. Fundamental Parameters Line Profile Fitting in Laboratory Diffractometers. *J. Res. Natl. Inst. Stand. Technol.* **2004**, 109 (1), 1–25.
- (22) Kittel, C. *Solid State Physics*, 8th ed.; 2001.

- (23) Design, Q. Physical Property Measurement System Operations Manual.
- (24) Aluri, E. R.; Grosvenor, A. P. *A Review of X-Ray Absorption Near-Edge Spectroscopic Studies of Pyrochlore-Type Oxides Proposed for Nuclear Materials Applications*; Elsevier Inc., 2016.
- (25) X-ray absorption fine structure (XAFS) - Online Dictionary of Crystallography [https://dictionary.iucr.org/X-ray\\_absorption\\_fine\\_structure\\_\(XAFS\)](https://dictionary.iucr.org/X-ray_absorption_fine_structure_(XAFS)) (accessed Jun 23, 2021).
- (26) Clavin, S. *XAS for Everyone*; CRC Press, 2013.
- (27) Bakerna, A.; Mobilio, S. *Synchrotron Radiation: Basics, Methods and Applications*; Springer, 2015.
- (28) Jiménez, E.; Isasi, J.; Sáez-Puche, R. Synthesis, Structural Characterization and Magnetic Properties of RCrO<sub>4</sub> Oxides, R=Nd, Sm, Eu and Lu. *J. Alloys Compd.* **2000**, 312 (1), 53–59.
- (29) Ravel, B.; Newville, M. Athena, Artemis and Hephaestus: Data Analysis for X-Ray Absorption Spectroscopy Using IFEFFIT. *J. Synchrotron Radiat.* **2005**, 12 (537–541).
- (30) Bain, G. A.; Berry, J. F. Diamagnetic Corrections and Pascal's Constants. *J. Chem. Educ.* **2008**, 85 (4), 532–536.
- (31) Huq, A.; Kirkham, M.; Peterson, P. F.; Hodges, J. P.; Whitfield, P. S.; Page, K.; Hogle, T.; Iverson, E. B.; Parizzia, A.; Rennich, G. POWGEN: Rebuild of a Third-Generation Powder Diffractometer at the Spallation Neutron Source. *J. Appl. Crystallogr.* **2019**, 52, 1189–1201.
- (32) Rice, C. E.; Robinson, W. R. Structural Changes in the Solid Solution (Ti<sub>1-x</sub>V<sub>x</sub>)<sub>2</sub>O<sub>3</sub> as x Varies from Zero to One. *J. Solid State Chem.* **1977**, 21 (2), 145–154.
- (33) Loehman, R. E.; Rao, C. N. R.; Honig, J. M. Crystallography and Defect Chemistry of Solid Solutions of Vanadium and Titanium Oxides. *J. Phys. Chem.* **1969**, 73 (6), 1781–1784.
- (34) Rice, C. E.; Robinson, W. R. Structural Changes Resulting from Doping Ti<sub>2</sub>O<sub>3</sub> with Sc<sub>2</sub>O<sub>3</sub> or Al<sub>2</sub>O<sub>3</sub>. *J. Solid State Chem.* **1977**, 21 (2), 155–160.
- (35) Reid, A. F.; Sienko, M. J. Scandium Titanite and Scandium Vanadite, ScTiO<sub>3</sub> and ScVO<sub>3</sub>. *Inorg. Chem.* **1967**, 6 (3), 521–524.
- (36) Lussier, J. A. Understanding the Structure and Reactivity of Solid State Electrolyte Model Systems, University of Manitoba, 2019.
- (37) Brixner, L. H. Preparation and Properties of the Ln<sub>2</sub>Ti<sub>2</sub>O<sub>7</sub> -Type Rare Earth Titanates. *Inorg. Chem.* **1964**, 3 (7), 1065–1067.
- (38) Rossell, H. J. Crystal Structures of Some Fluorite-Related M<sub>7</sub>O<sub>12</sub> Compounds. *J. Solid State Chem.* **1976**, 19 (2), 103–111.
- (39) Shafi, S. P. *Solid State Structure-Reactivity Studies on Bixbyites, Fluorites and Perovskites Belonging to the Vanadate, Titanate and Cerate Families*; 2012.
- (40) Ito, J. Synthesis of Scandium Pseudobrookite, Sc<sub>2</sub>TiO<sub>5</sub>. *Am. Mineral.* **1971**, 56 (480), 1105–1108.
- (41) Kolitsch, U.; Tillmanns, E. Sc<sub>2</sub>TiO<sub>5</sub>, an Entropy-Stabilized Pseudobrookite-Type Compound. *Acta Crystallogr. Sect. E Struct. Reports Online* **2003**, 59 (3), 36–39.
- (42) Lyashenko, L. P.; Kolbanev, I. V.; Shcherbakova, L. G.; Knerel'man, E. I.; Davydova, G. I. Effect of a Nonequilibrium State on Phase Relations in the System TiO<sub>2</sub>-Sc<sub>2</sub>O<sub>3</sub> (40-50 Mol % Sc<sub>2</sub>O<sub>3</sub>). *Inorg. Mater.* **2004**, 40 (8), 833–839.
- (43) Reid, A. F.; Sabine, T. M.; Wheeler, D. A. Neutron Diffraction and Other Studies of Magnetic Ordering in Phases Based on Cr<sub>2</sub>O<sub>3</sub>, V<sub>2</sub>O<sub>3</sub> and Ti<sub>2</sub>O<sub>3</sub>. *J. Solid State Chem.* **1972**, 4 (3), 400–409.
- (44) Lussier, J. A.; Simon, F. J.; Whitfield, P. S.; Singh, K.; Thangadurai, V.; Bieringer, M. Structure Evolution

- and Reactivity of the  $\text{Sc}_{2-x}\text{V}_x\text{O}_{3+\delta}$  ( $0 \leq x \leq 2.0$ ) System. *Inorg. Chem.* **2018**, *57* (9), 5607–5614.
- (45) Todorov, N. D.; Abrashev, M. V.; Russev, S. C.; Marinova, V.; Nikolova, R. P.; Shivachev, B. L. Raman Spectroscopy and Lattice-Dynamical Calculations of  $\text{Sc}_3\text{CrO}_6$  Single Crystals. *Phys. Rev. B - Condens. Matter Mater. Phys.* **2012**, *85* (21).
- (46) Belik, A. A.; Matsushita, Y.; Tanaka, M.; Takayama-Muromachi, E. Crystal Structures and Properties of Perovskites  $\text{ScCrO}_3$  and  $\text{InCrO}_3$  with Small Ions at the A Site. *Chem. Mater.* **2012**, *24* (11), 2197–2203.
- (47) Leutkina, E. V.; Puretskii, N. A.; Bobylev, A. P.; Komissarova, L. N. Solid-Phase Synthesis and Characterization of Rare-Earth Chromates. *Theor. Found. Chem. Eng.* **2007**, *41* (5), 567–571.
- (48) Jain, A.; Ong, S. P.; Hautier, G.; Chen, W.; Richards, W. D.; Dacek, S.; Cholia, S.; Gunter, D.; Skinner, D.; Ceder, G.; et al. The Materials Project: A Materials Genome Approach to Accelerating Materials Innovation. *APL Mater.* **2013**, *1* (1), 11002.
- (49) Jain, Anubhav and Ong, Shyue Ping and Hautier, Geoffroy and Chen, Wei and Richards, William Davidson and Dacek, Stephen and Cholia, Shreyas and Gunter, Dan and Skinner, David and Ceder, Gerbrand and Persson, K. a. Materials Project.
- (50) Long, Y. W.; Yang, L. X.; Yu, Y.; Li, F. Y.; Yu, R. C.; Jin, C. Q. Synthesis, Structure, Magnetism and Specific Heat of  $\text{YCrO}_4$  and Its Zircon-to-Scheelite Phase Transition. *Phys. Rev. B* **2007**, *75* (10), 104402.
- (51) Tezuka, K.; Doi, Y.; Hinatsu, Y. Crystal Structures and Magnetic Properties of Zircon-Type Compounds  $\text{Lu}_{1-x}\text{Y}_x\text{CrO}_4$ . *J. Mater. Chem.* **2002**, *12* (4), 1189–1193.
- (52) Lundgren, R. J.; Cranswick, L. M. D.; Bieringer, M. Phase Stability, Structural Evolution and Magnetic Properties of  $\text{Sc}_{(1-x)}\text{Lu}_x\text{VO}_3$  ( $0.0 \leq x \leq 1.0$ ). *Chem. Mater.* **2007**, *19* (16), 3945–3955.
- (53) C.J. Brinker; G. W. Scherer. *Sol-Gel Science: The Physics and Chemistry of Sol-Gel Processing*, 1st ed.; 1990.

## Appendix

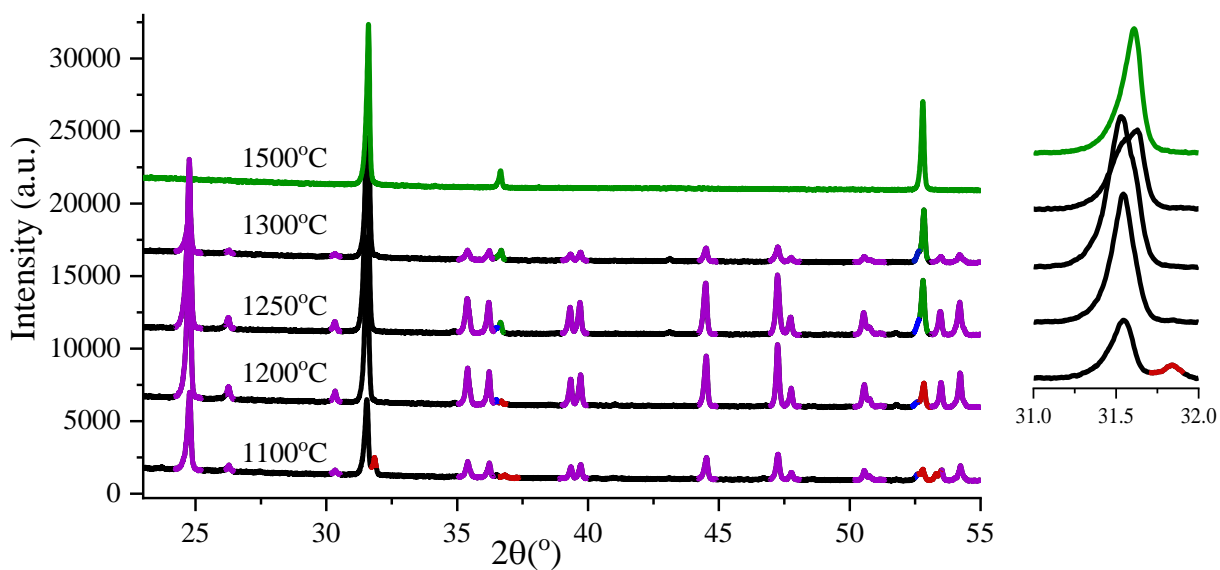


Figure A.1 X-ray diffraction data of 1:1 Sc<sub>2</sub>O<sub>3</sub> and TiO<sub>2</sub> heating at temperatures 1100°C, 1200°C, 1250°C, 1300°C, and 1500°C. Where peaks belonging to pseudobrookite phase are indicated in purple; fluorite = green; rhombohedral = red; and bixbyite = green. Note: peak at approximately 32° 2θ contains a mixture of phases in temperatures 1100°C-1300°C and is coloured black as it does not correspond to one phase. The inset highlights the major peak between 31° and 32° 2θ.

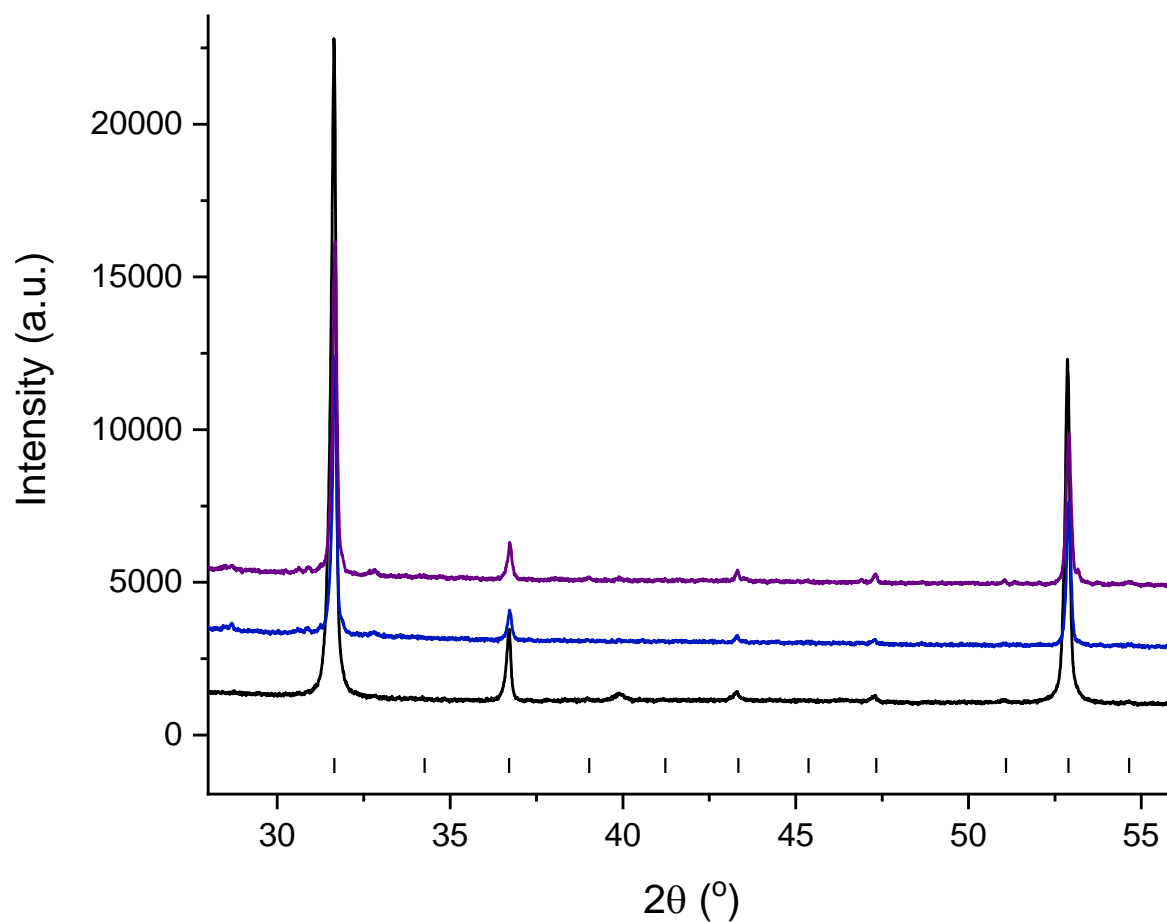


Figure A.2. Comparison of products obtained from reactions 2.7-2.9. Black = Ti/Ti<sup>4+</sup> starting material, Blue = Ti<sub>2</sub>O<sub>3</sub> starting material; Purple = TiO<sub>2</sub> starting material. Note: peak at 40° 2θ in black pattern is Pt impurity present from the Pt boat, where peak at 29.5° 2θ is Sc<sub>2</sub>Si<sub>2</sub>O<sub>7</sub> impurity phase from ceramic boat.

Table A.1. Refined structural parameters for tetragonal- $\text{Sc}_2\text{Ti}_{0.6}\text{V}_{0.4}\text{O}_{5+\delta}$  (s.g.  $I\bar{4}$ ,  $x = 0.6$ ) prepared via direct synthesis. The lattice parameters are refined as  $a = 7.81706(4)$  Å,  $c = 14.71473(9)$  Å, and  $V = 899.2(1)$  Å<sup>3</sup>.  $R_{\text{wp}}/\chi^2 = 3.41/1.25$ .

Atom	Site	x	y	z
Sc1	4f	0	1/2	0.4310(2)
Sc2	8g	0.9488(3)	0.2033(3)	0.2556(2)
Sc3	8g	0.6274(4)	0.3176(3)	0.4227(2)
V1	8g	0.2103(5)	0.1043(5)	0.4112(2)
V2	2c	0	1/2	3/4
O1	8g	0.108(1)	0.237(1)	0.5036(6)
O2	8g	0.829(1)	0.378(1)	0.3365(6)
O3	8g	0.809(1)	0.417(1)	0.5293(5)
O4	4e	0	0	0.6397(9)
O5	4e	0	0	0.1719(8)
O6	2a	1/2	1/2	1/2
O7	8g	0.7335(7)	0.178(1)	0.6775(6)
O8	8g	0.0753(9)	0.3391(8)	0.6791(7)

Note: Thermal parameters for cation and anion sites were fixed to  $1.0$  Å<sup>2</sup> and  $0.5$  Å<sup>2</sup>, respectively.

Table A.2. Refined structural parameters for tetragonal-Sc<sub>2</sub>Ti<sub>0.2</sub>V<sub>0.8</sub>O<sub>5+δ</sub> (s.g.  $I\bar{4}$ , x = 0.2) prepared via direct synthesis. The lattice parameters are refined as a = 7.77925(6) Å, c = 14.6012(1) Å, and V = 899.2(1) Å<sup>3</sup>. R<sub>wp</sub>/χ<sup>2</sup> = 3.18/1.16.

Atom	Site	x	y	Z
Sc1	4f	0	½	0.4289(4)
Sc2	8g	0.9512(4)	0.2011(5)	0.2602(3)
Sc3	8g	0.6280(5)	0.3228(5)	0.4211(2)
V1	8g	0.2100(6)	0.1008(5)	0.4177(3)
V2	2c	0	½	¾
O1	8g	0.104(1)	0.237(1)	0.5042(8)
O2	8g	0.836(1)	0.386(1)	0.3283(7)
O3	8g	0.819(1)	0.427(1)	0.5316(6)
O4	4e	0	0	0.6393(9)
O5	4e	0	0	0.176(1)
O6	2a	½	½	½
O7	8g	0.724(7)	0.1987(9)	0.6719(7)
O8	8g	0.066(9)	0.345(1)	0.6763(7)

Note: Thermal parameters for cation and anion sites were fixed to 1.0 Å<sup>2</sup> and 0.5 Å<sup>2</sup>, respectively.